ON THE RHEOLOGY AND MAGNETIZATION OF DILUTE MAGNETIC EMULSION UNDER SMALL AMPLITUDE OSCILLATORY SHEAR

Rodrigo Figueiredo Abdo

PhD Thesis
Programa de Pós-Graduação em Ciências Mecânicas

UNIVERSIDADE DE BRASÍLIA

Faculdade de Tecnologia
Departamento de Engenharia Mecânica

UNIVERSIDADE DE BRASÍLIA
FACULDADE DE TECNOLOGIA
DEPARTAMENTO DE ENGENHARIA MECÂNICA

ON THE RHEOLOGY AND MAGNETIZATION OF DILUTE MAGNETIC EMULSION UNDER SMALL AMPLITUDE OSCILLATORY SHEAR

Rodrigo Figueiredo Abdo

Orientador: Dr. Taygoara Felamingo de Oliveira (ENM/ UnB)

PHD THESIS

PUBLICAÇÃO: ENM.DM - XXX.XXX

BRASÍLIA/DF: 6 de abril de 2023

UNIVERSIDADE DE BRASÍLIA
FACULDADE DE TECNOLOGIA
DEPARTAMENTO DE ENGENHARIA MECÂNICA

On the rheology and magnetization of dilute magnetic emulsion under small amplitude oscillatory shear

Rodrigo Figueiredo Abdo

TESE DE DOUTORADO SUBMETIDA AO DEPARTAMENTO DE ENGENHARIA MECÂNICA DA FACULDADE DE TECNOLOGIA DA UNIVERSIDADE DE BRASÍLIA COMO PARTE DOS REQUISITOS PARCIAIS PARA A OBTENÇÃO DO GRAU DE DOUTOR EM PROGRAMA DE PÓS-GRADUAÇÃO EM CIÊNCIAS MECÂNICAS.

APROVADA POR:

Dr. Taygoara Felamingo de Oliveira (ENM/ UnB)
(Orientador)

Dr. Rafael Gabler Gontijo (ENM/ UnB)
(Examinador Interno)

Dr. Roney Leon Thompson (COPPE/ UFRJ)
(Examinador Externo)

Dr. Antonio Castelo Filho (ICMC/ USP)
(Examinador Externo)

BRASÍLIA/DF, 6 DE ABRIL DE 2023.

FICHA CATALOGRÁFICA

Rodrigo F. Abdo
On the rheology and magnetization of dilute magnetic emulsion under small amplitude oscillatory shear [Distrito Federal] 2023.
xvii, 84p. (ENM/FT/UnB, Doutor, Programa de Pós-Graduação em Ciências Mecânicas, 2023.
PhD Thesis - Universidade de Brasília.
Faculdade de Tecnologia.
Departamento de Engenharia Mecânica.
Palavras-chave:
1. Oscillatory shear 2. Magnetic emulsions
3. Two-phase flow 4. Level-Set
I. ENM/FT/UnB II. Título (série)

REFERÊNCIA BIBLIOGRÁFICA

Rodrigo F. Abdo(2023). On the rheology and magnetization of dilute magnetic emulsion under small amplitude oscillatory shear. PhD Thesis, Publicação ENM.DM - XXX.XXX, Departamento de Engenharia Mecânica, Universidade de Brasília, Brasília, Distrito Federal, xvii, 84p.

CESSÃO DE DIREITOS

NOME DO AUTOR: Rodrigo Figueiredo Abdo.

TÍTULO DA TESE DE DOUTORADO: On the rheology and magnetization of dilute magnetic emulsion under small amplitude oscillatory shear.

GRAU / ANO: DOUTOR / 2023

Rodrigo Figueiredo Abdo

Acknowledgements

Due to the great amount of emotional content in the following words, those will be written in Portuguese.

Durante essa jornada tive o apoio de várias pessoas e instituições, as quais gostaria de deixar meu expresso agradecimento.

Em primeiro lugar, agradecer meus pais e meu irmão: Nagib, Ludmila e Tiago. Partes inseparáveis da minha construção. Tornei-me, em meio às qualidades e aos defeitos, a pessoa que sou hoje graça a vocês. Se hoje posso caminhar com as minhas próprias pernas, de forma digna e honrada, é porque tive o apoio e carinho de cada um ao longo dessa trajetória. Vocês fizeram e fazem, incondicionalmente, o impossível para que isso pudesse se tornar realidade. Meus agradecimentos não caberiam em uma página. Estendo toda essa gratidão aos meus queridos avós, Eda e Léo (in memoriam).

À minha querida esposa, Ana Luisa. O melhor presente que a vida poderia ter me dado. A pessoa que, diariamente, extrai o melhor de mim e me ajuda a construir a melhor versão de quem eu sou. Mulher de valores inigualáveis, que ao meio de tantas coisas, achou um espaço para brigar pelos meus sonhos e torná-los realidade. Não existe compromisso maior do que essa doação. Não menos importante, meus queridos sogros: Olímpio e Betânia. Pessoas com um coração gigante e alma irradiadora. Estiveram ao meu lado todo esse tempo, aconselhando, ajudando, buscando oportunidades e oferendo todo acolhimento possível.

Ao professor e orientador Taygoara. Certamente uma das melhores escolhas durante essa jornada. Um profissional dedicado que esbanja vitalidade e inspiração por meio de sua vocação como professor. Agradeço pelas memoráveis aulas, conversas, orientações e opiniões em seus mais diversos campos. Posso afirmar, com clareza, que estou saindo muito melhor do que entrei. Você é parte essencial nesse caminho e guardo uma admiração especial pela sua dedicação em ter proporcionado isso.

Agradeço ao Instituto Federal de Brasília, campus Estrutural, ao qual sou professor, por abrir as portas de um sonho antigo e confiar no meu potencial durante essa jornada. Estendo esse agradecimento a Universidade de Brasília, um lugar incrível em que vivi dias maravilhosos.

Não menos importante, aos colegas que partilharam desse caminho e contribuíram

para a excelência de todo esse trabalho: Lucas Hildebrand Pires da Cunha e Victor Guinancio e Abicalil.

"Life is not easy for any of us. But what of that? We must have perseverance and, above all, confidence in ourselves. We must believe that we are gifted for something, and that this thing, at whatever cost, must be attained."

Marie Curie

Resumo

On the rheology and magnetization of dilute magnetic emulsion under small amplitude oscillatory shear

Autor: Rodrigo Figueiredo Abdo

Orientador: Dr. Taygoara Felamingo de Oliveira (ENM/ UnB)

Programa de Pós Graduação em Programa de Pós-Graduação em Ciências Mecânicas

Brasília, 6 de abril de 2023

Uma emulsão magnética diluída, sob a ação combinada de um campo magnético externo e um cisalhamento oscilatório de pequena amplitude é estudado utilizando simulações numéricas. Nossas simulações consideram um domínio tridimensional onde uma única gota de ferrofluido superparamagnético é suspensa numa matriz não magnetizável e diluída. Além disso, a gota é confinada num canal periódico entre placas paralelas onde o campo magnético externo pode ser imposto em cada uma das direções das coordenadas. O método numérico escolhido baseia-se no método de projeção para as equações incompressíveis de Navier-Stokes, acrescido de um termo interfacial e magnético, e do método level-set para a captura da interface. De acordo com o sinal periódico da gota, estudamos a sua dinâmica, reologia e resposta da magnetização através de uma gama de frequências angulares, amplitudes da taxa de cisalhamento e intensidades do campo magnético externo. Verificamos que o campo magnético pode alterar significativamente a dinâmica e a morfologia da gota, confinando também a gota em regiões de maior ou menor cisalhamento efetivo. Tal fato implica que o campo magnético pode alterar de forma crítica as respostas elásticas e viscosas em função da frequência, especialmente quando orientado na direção da vorticidade, na qual é possível controlar ativamente o tempo de relaxação da gota. Também a este respeito, o campo magnético causa uma anisotropia de tensões na sua respectiva direção de aplicação, o que é demonstrado através das diferenças de tensões normais. Finalmente, embora se trate de uma gota de ferrofluido superparamagnético, encontramos uma componente periódica fora de fase da magnetização, o que significa que o tempo de relaxação magnético é finito e está intimamente relacionado com a relaxação

mecânica.

Palavras-chaves: Oscillatory shear; Magnetic emulsions; Two-phase flow; Level-Set.

Abstract

ON THE RHEOLOGY AND MAGNETIZATION OF DILUTE MAGNETIC EMULSION UNDER SMALL AMPLITUDE OSCILLATORY SHEAR

Author: Rodrigo Figueiredo Abdo

Supervisor: Dr. Taygoara Felamingo de Oliveira (ENM/ UnB)

Thesis Proposal in Mechanical Sciences

Brasília, 2023

A dilute magnetic emulsion, under the combined action of an external magnetic field and a small amplitude oscillatory shear, is studied using numerical simulations. In order to achieve this, our simulations consider a three-dimensional domain where a single superparamagnetic ferrofluid droplet is suspended in a non-magnetizable and diluted matrix. Furthermore, the droplet is confined in a periodic channel between parallel plates where the external magnetic field can be imposed in each of the coordinate directions. The chosen numerical method is based on the projection method for the incompressible Navier-Stokes equations, augmented by an interfacial and magnetic term, and the level-set method for interface capturing. According to the periodic signal of the droplet, we studied its dynamics, rheology and magnetization response across a range of angular frequencies, shear-rate amplitudes, and external magnetic fields. We found that the magnetic field can significantly change the dynamics and morphology of the droplet, also confining the droplet to regions of greater or lower effective shear. Such a fact implies that the magnetic field can critically alter the elastic and viscous responses as a function of frequency, especially when oriented in the direction of the vorticity, in which it is possible to actively control the droplet relaxation time. Also in this regard, the magnetic field causes a stress anisotropy in its respective direction of application, which is shown through the normal stress difference. Finally, although it is a superparamagnetic ferrofluid droplet, we found an out-of-phase periodic component of the magnetization, which means that the magnetic relaxation time is finite and closely related to mechanical relaxation.

Key-words: Oscillatory shear, magnetic emulsions, two-phase flow, Level-Set.

List of Figures

List of Tables

Content

List of abbreviations and acronyms

$CLSVOF$	Coupled level set/volume-of-fluid
$LAOE$	Large amplitude oscillatory extensional
$LAOS$	Large amplitude oscillatory shear
$SAOS$	Small amplitude oscillatory shear
$SBDF2$	Second order Semi-backward difference formula
FFT	Fast Fourier Transform

List of symbols

Latin letters

a	Initial droplet radius
$a,\ b,\ c,\ d, ...$	Linear coefficients
B, $\mathbf{B}$	Minor axis of the ellipsoid and magnetic induction
c, C	Cut-off function or intermediary ellipse axis
Ca	Capillary number
d, D, $\mathbf{D}$	Signed distance function, Taylor deformation parameter and second-order rate of deformation tensor
$\mathbf{F}$	Force per unit volume
G', G'', G^*	Storage and loss moduli and complex modulus
H, $\mathbf{H}$	Heaviside function and magnetic field vector
$\mathbf{I}$, $\mathbf{I}^*$	Unit second-order tensor and inertia tensor
L	Domain length or the major axis of the ellipsoid
M, $\mathbf{M}$, $\langle\mathbf{M}\rangle$	Magnetization component, magnetization vector and mean magnetization vector
N	Normal stress difference
$\hat{\mathbf{n}}$	Unit normal vector
Oh	Ohnesorge number
p	Pressure
q	Pressure approximation
$\mathbf{r}$	Euclidian distance
Re	Reynolds number

S	Reinitialization auxiliary function
t, $\mathbf{t}$	Time, tangential vector
u, $\mathbf{u}$	Velocity in x-direction and velocity vector
v	Velocity in y-direction
w	Velocity in z-direction
$\mathbf{x}$	Position vector
	Greek letters
β	Volume fraction or narrow band parameter
γ	Shear-strain or narrow band parameter
$\dot{\gamma}$	Shear-rate
δ	Phase shift or Diract delta function
$\Delta\mathbf{f}$	Stress jump across the droplet surface
ϵ	Size of the bandwidth
ζ	Magnetic permeability ratio (μ_d/μ_0)
η, η', η''	Viscosity, dynamic viscosity and out-of-phase viscosity
θ, θ', θ''	Droplet inclination angle or angle between $\langle\mathbf{M}\rangle$ and $\mathbf{H}_0$, in-phase and out-of-phase components
κ	Curvature
λ, Λ	Vicosity ratio (η_d/η_c) or volume correction factor and eigenvalues
μ	Magnetic permeability
ρ	Specific mass
σ, Σ, $\mathbf{\Sigma}$	Surface tension, stress component and stress tensor
τ, $\boldsymbol{\tau}$, τ', τ''	Virtual time or torque magnitude, torque and in-phase and out-of-phase components
ϕ	Level set function
χ, χ', χ''	Magnetic susceptibility, in-phase and out-of-phase components
ψ	Magnetic scalar potential
ω, Ω, $\partial\Omega$	Angular frequency and domain and interface

Subscript

0	Initial condition/amplitude/vacuum
1	First
2	Second
3	Third
b	Related to the bulk propertie
c	Continuous phase and capillary
d	Dispersed phase
e	Effective
h	Hydrostatic
$i,\ j,\ k$	Grid cell position
ϵ	Smoothed
mag	Magnetic
x	Oriented in the x-direction or relative to the x coordinate
y	Oriented in the y-direction or relative to the y coordinate
z	Oriented in the z-direction or relative to the z coordinate
yx	Normal to y in the x direction
xx	Normal to x in the x direction
yy	Normal to y in the y direction
zz	Normal to z in the z direction

Superscript

D	Related to the particle stress tensor

1 Motivation and background

Emulsions are dispersion systems made up of two or more immiscible liquids, in which the liquid droplets are considered as the dispersed phase and the liquid medium the continuous phase (Tadros, 2013). The most striking examples of emulsions are the classical mixtures of oil-in-water (O/W), water-in-oil (W/O), or even the oil-in-oil (O/O), such as propylene glycol in paraffinic oil (Pal, 2019). Another system structure is found in double and multiple emulsions, *i.e.*, emulsions of emulsion, such as W/O/W or O/W/O. These specific emulsions are known for their extraordinary ability and significant potential in the encapsulation and controlled release of active substances, separation and extraction procedures, and microreactors for chemical reactions (Liu et al., 2021).

A great aspect of emulsions, in general, is that despite often being composed of Newtonian fluids, emulsions present a complex non-Newtonian behavior, presenting a dual characteristic depending on the shear-rate and shear-strain. The emulsion starts to have a more predominantly elastic or viscous behavior, depending on the time scale of the experiment and the properties of the emulsion constituents.

While simple shear is the traditional way of evaluating the properties of fluids in their natural time scale, oscillatory shear is the most popular deformation mode for investigating viscoelastic properties. The experiment induces a sinusoidal shear deformation, in which oscillation frequency determines the time scale and, thus, allows measures of the stress response.

Based on a small amplitude oscillatory shear experiment, the viscoelastic properties are the storage (G') and loss (G'') moduli. These two parameters decompose time-dependent stress into real and imaginary parts of a complex number. For a sinusoidal shear deformation, the storage modulus is in phase with the strain and follows the macroscopic deformation, consequently storing energy. The loss module is 90° out-of-phase with strain and measures the energy dissipated or lost as heat.

Despite their widespread use and significance in emulsions, our understanding of stability, which involves the knowledge of viscoelastic properties, remains limited. Improving our understanding of emulsion stability is essential for the development of high-quality and stable emulsions with a wide range of applications, such as found in enhanced oil recovery (Zhou et al., 2019), pipeline transportation of heavy crude oil in water (Ashrafizadeh; Kamran, 2010) and alternative fuel for diesel engines (Debnath; Saha; Sahoo, 2015). One of

the most successful fields of application is in the biomedical area, comprising, for example, drug carrier systems (Shukla et al., 2018). It is worth mentioning that the knowledge of emulsion properties has also been crucial in preventative and therapeutic solutions against COVID-19 (Sharma; Singh, 2021; Ashaolu, 2021; Tayeb et al., 2021). Figure 1.1 presents a schematic representation of an oil-in-water nanoemulsion (O/W NE) of encapsulated hydrophobic compounds and surface-functionalized biomolecules of O/W NEs proposed by Tayeb et al. (2021). Drugs, vitamins, colors, dyes, oil or flavors can be encapsulated and delivered by specific antibodies, polymers, aptamers or a fluorescent probe.

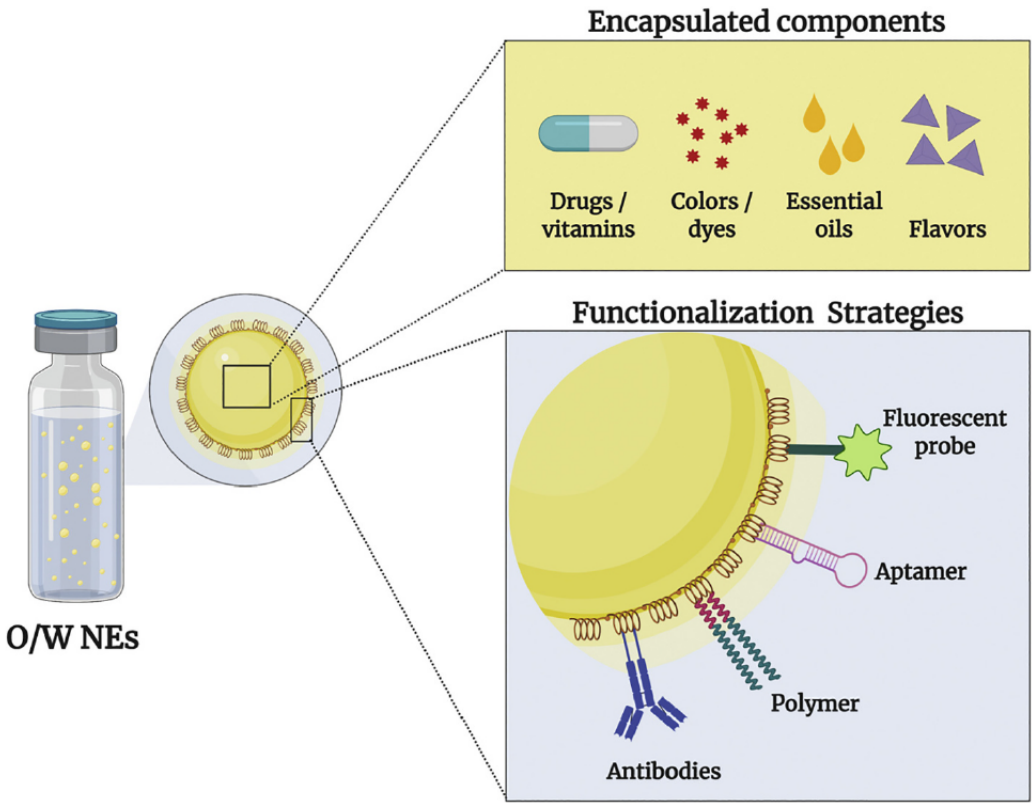

Figure 1.1 – Encapsulated hydrophobic compounds and surface-functionalized biomolecules of oil-in-water nanoemulsion (Tayeb et al., 2021).

Table 1 presents typical parameters of emulsions found in food applications. It is important to note that O/W emulsions, such as milk or mayonnaise, form compounds with completely different physical properties than W/O emulsions, such as butter or margarine. Properties such as the viscosity of both phases, droplet size distribution, chemical composition or the interfacial interactions among the phases can drastically modify the flow characteristics. A key factor to consider is shown in the last column of Tab. 1, which represents the ratio between the volume of the dispersed and continuous phase, commonly called volume fraction. In the case of dilute emulsions, the particle-particle interactions are of negligible importance, *i.e.*, the linear scale of the suspension motion is large compared with the average distance between the particles. In this scenario, for dilute systems with volume fraction up to 5% (Guido; Shaqfeh, 2019), it is possible to characterize the entire emulsion by studying only a single droplet, provided that in a

large periodic domain. One of the most important aspects, in this case, is the fact that emulsions can be considered as a continuum, in which the macroscopic properties are obtained through an averaging process of microscopic quantities. This methodology is, indeed, followed by many authors in many different research fields (Vlahovska, 2011; Raja; Subramanian; Koch, 2010; Ghigliotti; Biben; Misbah, 2010; Poddar et al., 2019; Mandal et al., 2018).

Table 1.1 – Typical parameters of emulsions according to Pal (2019)

Food product	**Disp. phase**	**Cont. phase**	**Vol. fraction (%)**
Milk	Oil droplets	Water	3 to 4
Butter	Water droplets	Liquid oil and fat crystals	About 16
Margarine	Water droplets	Liquid oil and fat crystals	16 to 50
Mayonnaise	Oil droplets	Water	≥ 65
Coffee whiteners	Oil droplets	Water	10 to 16
Salad dressings	Oil droplets	Water	≥ 30

In parallel, over the years, a great amount of research has been carried out in an attempt to tune or control the properties of emulsions. Many authors investigated, experimentally (Pei et al., 2018; Feigl et al., 2007) and numerically (Pimenta; Oliveira, 2021; Stone; Leal, 1990), the use of surfactants in emulsions in order to change the surface properties or change the local thermodynamic environment. Figure 1.2(a) shows a water droplet structure surrounded by surfactants with hydrophilic heads and hydrophobic tails. Similarly, the Pickering emulsions, which provide a more stable system than classic emulsions obtained with a surfactant (Carvalho-Guimarães et al., 2022) is present in Fig. 1.2(b). In this case, the water droplet is stabilized through interface adsorption by solid particles, preventing coalescence, sedimentation or the formation of cream (Chen et al., 2011).

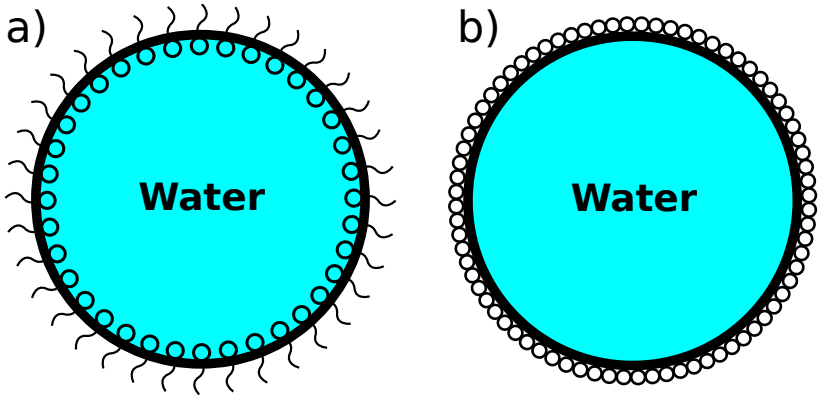

Figure 1.2 – Surfactant-stabilized water droplet (a) and a Pickering emulsion droplet (b).

Another effective way to achieve the desired properties in a droplet, and consequently in the emulsion, is by using materials capable of becoming anisotropic under the action of an external agent. In this case, one of the approaches is based on the use of external electric or (and) magnetic fields in ferrofluid emulsions.

Since the conception, formulation and synthesis of a ferrofluid by Steve Papell (Stephen, U.S. Patent 3 215 572 A, 1963), considerable research attention has been directed toward this area. Magnetic emulsions are an emerging field of study that combines the properties of magnetic particles and liquid emulsions. This area of research has garnered interest due to the unique physical and chemical properties that magnetic emulsions exhibit, which are not present in traditional emulsions or magnetic particles alone.

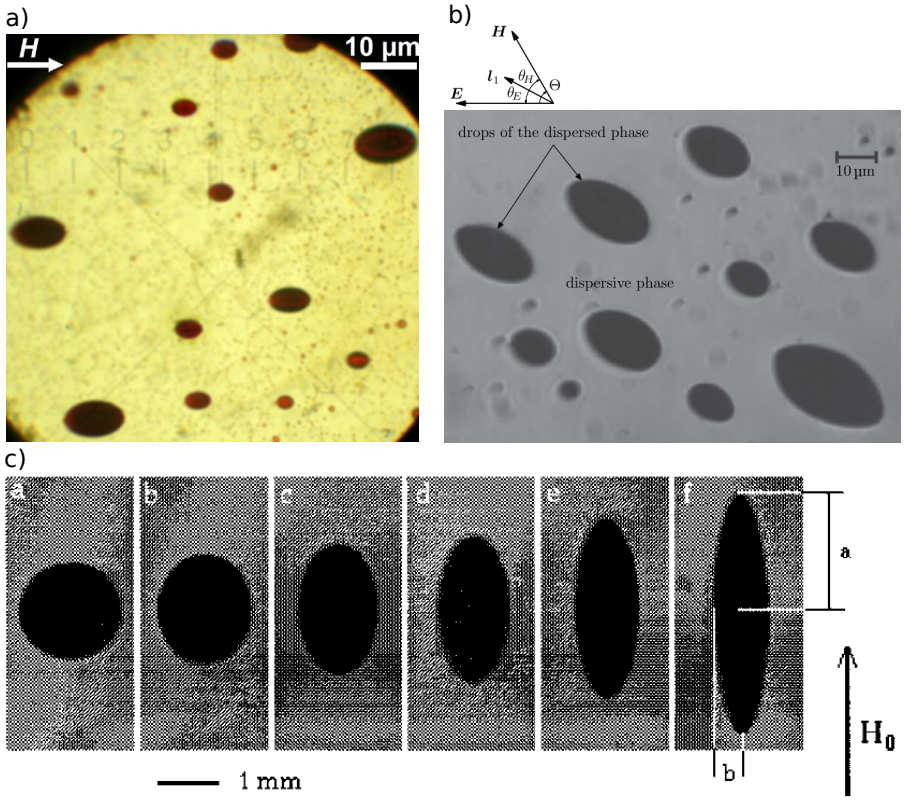

Figure 1.3 – Magnetic emulsion affected by a uniform magnetic field (a) and (c) (Zakinyan; Dikansky, 2011; Flament et al., 1996) and simultaneously by electric and magnetic fields (b) (Dikansky; Zakinyan; Tyatyushkin, 2011).

Both the magnetic and electric fields, depending on their orientation, are capable of critically altering the dynamics and rheology of the dispersed ferrofluid droplet. Figure 1.3(a) shows ferrofluid droplets immersed in oil under a uniform magnetic field. The emulsion droplets become ellipsoidal and aligned along the magnetic field direction. Similarly, in Fig. 1.3(c), the same phenomenon happens, but in this case, it is evident that the droplet elongation is related to the intensity of the magnetic field. Figure 1.3(b) shows the combination of both the magnetic and electric fields. In this case, due to the anisotropy caused by the external fields, the electric conductivity and magnetic permeability are no longer a scalar, but a second-order tensor. It is worth mentioning that the same effects, for example, can also be applied to magnetic Pickering emulsions (Bielas et al., 2022) or in confined magnetic nanoparticles in double emulsions (Zentner; Concellón; Swager, 2020).

There is ample evidence to support the view that magnetic emulsions can substantially contribute to the development of new technologies. Some applications were

reported in many areas, for example, lab-on-a-chip technologies (Hamilton et al., 2018), magnetic pump and cilia (Meng et al., 2019), externally controlled materials (Andablo-Reyes; Hidalgo-Álvarez; Vicente, 2011) and treatment of retinal detachment (Mefford et al., 2007; Voltairas; Fotiadis; Massalas, 2001). There are also applications found in environmental science, where they have been used for the removal of pollutants from water. The magnetic droplets can be used to absorb and retain contaminants, and the external magnetic field can be used to separate the magnetic droplets from the water, thus purifying the water (Yang et al., 2017).

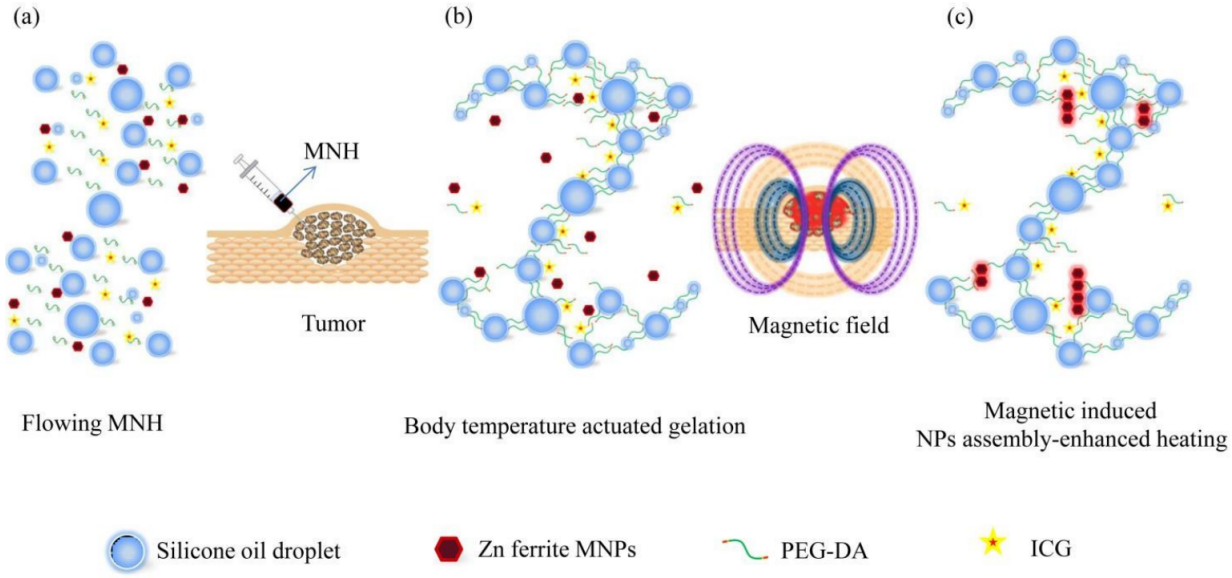

Figure 1.4 – Schematically representation of the use of magnetic fluids in hyperthermia for cancer therapy. (a) represents the injection of magnetic nanoemulsion hydrogel, (b) the solid-like magnetic hydrogel transformation and (c) the thermal ablation (Wu et al., 2017)

One of the most significant applications of magnetic emulsions is in the field of biomedicine. Magnetic emulsions have been used for the delivery of drugs to specific sites within the body, using an external magnetic field to guide the magnetic droplets to the desired location (Liu; Li; Lam, 2018). The encapsulation of drugs in magnetic droplets can improve their bioavailability, increase their stability, and reduce their toxicity. This opens up new opportunities for the treatment of diseases, particularly in hyperthermia for cancer therapy (Das; Colombo; Prosperi, 2019). Figure 1.4 shows, schematically, how this technology works. In Fig. 1.4(a), a magnetic nanoemulsion hydrogel (MNH), with temperature $< 25°\ C$, is injected into the tumor tissues. Once in contact with body temperature ($\approx 37°C$), it is transformed into a solid-like magnetic hydrogel, preventing leakage from the region, see Fig. 1.4(b). By applying an alternating current magnetic field, the magnetic nanoparticles induce the necrosis of tumor tissue by thermal ablation, Fig. 1.4(c). It is worth mentioning that all this process can be monitored by ultrasound in real-time, as well (Wu et al., 2017).

Even though there are several and successful applications of magnetic emulsions in different contexts, many crucial questions remain unanswered. Few studies in this research area have sought to examine the droplet dynamics, rheological, and magnetization properties, especially in oscillatory shear. As an example of the richness of the subject, it was only recently reported (Cunha et al., 2020b; Abicalil et al., 2021) that, under the combined action of a uniform magnetic field and simple shear flow, there is a misalignment between the bulk magnetization and the original external magnetic field for a superparamagnetic dilute emulsion. Furthermore, promoting a magnetic torque that leads to an antisymmetric bulk stress tensor. This fact alone can lead to the development or improvement of new technologies and processes. Also taking into account that these emulsions, as a non-Newtonian fluid, have viscoelastic and magnetization properties, an even greater field of application and study is expected.

2 Literature review

A disperse combination of two immiscible liquids, such as oil and water, is known as an emulsion. Even while emulsions are often made of Newtonian fluids, their overall behavior is that of a single non-Newtonian fluid, indicating that they have both viscosity and elasticity. Thus, they have solid-like and fluid-like behavior, which means that their viscosity is not constant and varies according to the flow kinematics and the constitution of the emulsion. Emulsions are especially helpful in a variety of applications, including the culinary and cosmetic sectors, where they are utilized as the foundation for goods like milk homogenization (Bai et al., 2021), optimizing the delivery of active pharmaceutical substances (Jaiswal; Dudhe; Sharma, 2015) and cosmetic products (Kim; Oh; Lee, 2020).

Dilute emulsions have been a topic of interest in the field of physics since the early 20th century, with seminal work done by Albert Einstein in 1906 and 1911 (Einstein, 1906; Einstein, 1911). Einstein's work laid the foundation for our understanding of dilute emulsions. In his paper, Einstein considered a dilute emulsion of rigid spheres in a such way one particle does not influence the neighborhood of others. Based on the viscous dissipation produced by the flow around a single sphere, Einstein predicted that the effective viscosity of a dilute emulsion, η_e, increases linearly with the volume fraction, β, being $\eta_e = \eta_c(1 + 5\beta/2)$, where η_c is the viscosity of the continuous phase.

Taylor (1932) extended Einstein's work by changing solid for fluid spheres, leading to $\eta_e = \eta_c(1 + 2.5\beta(\lambda + 0.4)/(\lambda + 1))$, where λ is the ratio between the viscosities of the dispersed and continuous phase. Both Einstein and Taylor works were experimentally validated, showing an excellent agreement, respectively, for $\beta < 3\%$ and $\beta < 5\%$ (Pal, 2016).

On the other hand, moderately and highly concentrated emulsions are those in which the volume fraction exceeds $\approx 2\%$ (Pal, 2011) (although the literature records higher values, such as 5% (Yang; Shaqfeh, 2018a; Yang; Shaqfeh, 2018b) or 10% (Barnes; Hutton; Walters, 1989)), reaching volume fractions even greater than the maximum packing volume. In both cases, the neighboring droplets interact with each other hydrodynamically or are deformed among each other, losing their spherical shape.

The beauty of dilute emulsions, in contrast to moderately and highly concentrated emulsions, is that it is only necessary to consider a single droplet mechanism to develop the macroscopic relationships or bulk properties. Since the works of Einstein and Taylor, there

is a growing body of research on the macroscopic mechanical properties of heterogeneous media. Table 2.1 presents a short review of some papers that predicted emulsion properties based on a single particle system. It is important to note that it is only a list of examples. Many other works were published along these lines, including the classic works of Taylor (1934), Oldroyd and Wilson (1953), Batchelor (1970) and the following papers in this section.

In like manner, Palierne (1990), by studying the effects of interfacial tension, investigated the linear viscoelastic behavior of diluted and non-diluted emulsions by introducing an oscillatory shear into the flow. The great contribution of Palierne's model was to consider a deformation-dependent interfacial shear, leading to nonisotropic interfacial stress (Jacobs et al., 1999). His model is well-known for accurately describing molten polymer mixes at both high and low frequencies (Bousmina, 1999; Jacobs et al., 1999; Shu et al., 2013). Additionally, his theory allows the previous approaches of Fröhlich and Sack (1946), Oldroyd and Wilson (1950), Oldroyd and Wilson (1953), Oldroyd and Taylor (1955) and Kerner (1956) to be generalized.

Analogously, both Cavallo, Guido and Simeone (2003) and Wannaborworn, Mackley and Renardy (2002) focused their work on the droplet dynamics in dilute emulsion under small amplitude oscillatory shear flows. They found the same ellipsoidal shape reported by Taylor (1934) and other authors. The droplet deformation is harmonic and its amplitude is a linear function of the strain. Furthermore, as the flow is reversed, the droplet is compressed in the direction of its major axis and extended along the minor axis, *i.e.*, the principal axis of the droplet switches from extension to compression, approaching a spherical shape between the shear cycles. Interestingly, it was reported that the only breakup mechanism occurred by end pinching at strain peaks, and, as expected, the critical shear for droplet breakup is higher in oscillatory shear than in simple shear.

Similarly, using the boundary integral method (Siqueira et al., 2017a; Cunha et al., 2018; Siqueira et al., 2017b) and an asymptotic solution based on the small deformation theory (Vlahovska; Bławzdziewicz; Loewenberg, 2009), Oliveira and Cunha (2015) reported a rheological study on droplets with moderate to high viscosity ratios subjected to oscillatory shear flow, demonstrating that the dynamics, in this case, are dependent on the shear-rate amplitude, oscillation frequency, and droplet relaxation time. The authors also reported that by imposing large amplitude oscillatory shear the emulsion stress response displays high-order harmonics.

Table 2.1 – Studies on diluted emulsions considering a single droplet.

Title	Journal	Short description
Motion and deformation of liquid drops and the rheology of dilute emulsions in simple shear flow (Kennedy; Pozrikidis; Skalak, 1994)	Computers and Fluids	Study of dilute emulsions using the boundary integral method to compute the effective stress tensor of appreciably deformed droplets.
Equation of change for ellipsoidal drops in viscous flow (Maffettone; Minale, 1998)	Journal of Non-Newtonian Fluid Mechanics	Phenomenological model for the droplet deformation.
Ellipsoidal model for droplet deformation in emulsions (Yu; Bousmina, 2003)	Journal of Rheology	Ellipsoidal model for droplet deformation for dilute emulsions composed of Newtonian fluids with an arbitrary viscosity ratio.
Drop breakup in dilute Newtonian emulsions in simple shear flow: New drop breakup mechanisms (Zhao, 2007)	Journal of Rheology	Experimental study of droplet breakup in a dilute Newtonian emulsion of different viscosity ratio under simple shear.
Inertial effects on the rheology of a dilute emulsion (Raja; Subramanian; Koch, 2010)	Journal of Fluid Mechanics	The authors derive an expression for the bulk stress in a dilute emulsion using a small, but finite Reynolds number.
Rheology of a dilute two-dimensional suspension of vesicles (Ghigliotti; Biben; Misbah, 2010)	Journal of Fluid Mechanics	The paper presents, based on the boundary integral method, a link between the rheology of dilute suspensions of vesicles and the constituent particles.
On the rheology of a dilute emulsion in a uniform electric field (Vlahovska, 2011)	Journal of Fluid Mechanics	The author studies the effective emulsion properties such as coupling of shape distortion, charge convection and stress bases on an isolated droplet in an external flow.

Drop deformation and emulsion rheology under the combined influence of uniform electric field and linear flow (Mandal et al., 2018)	Journal of Fluid Mechanics	The paper presents a study on the effect of a uniform electric field on the emulsion rheology based on an isolated droplet under the combined presence of an external uniform electric field and uniaxial extensional flow.
Emulsion rheology for steady and oscillatory shear flows at moderate and high viscosity ratio (Oliveira; Cunha, 2015)	Rheol Acta	The authors present a complete study using a three-dimensional boundary integral method for a single droplet to investigate the emulsions rheology at high viscosity ration in steady, oscillatory and extensional flow.
Electrorheology of a dilute emulsion of surfactant-covered drops (Poddar et al., 2019)	Journal of Fluid Mechanics	A viscous droplet covered by surfactants is studied using a three-dimensional numerical model in order to investigate the bulk emulsion properties in the dilute suspension regime.
Field-induced control of ferrofluid emulsion rheology and droplet break-up in shear flows (Cunha et al., 2018)	Physics of Fluids	Based on a two-dimensional finite domain size with a single ferrofluid droplet under a uniform external magnetic field, the authors investigated how the magnetic field intensity affects the emulsion rheology under the simple-shear.
Effects of external magnetic fields on the rheology and magnetization of dilute (Cunha et al., 2020b)	Physics of Fluids	Similar to (Cunha et al., 2018), but the authors investigate the stress response, the bulk magnetization and magnetic torque as a contribution of the non-symmetric bulk stress tensor.
Rheology of a dilute ferrofluid droplet suspension in shear flow: Viscosity and normal stress differences (Ishida; Matsunaga, 2020)	Physical Review Fluids	Similar to previous two studies reported by Cunha et al. (2018) and Cunha et al. (2020b), but in a three-dimensional domain. The authors present additional results by applying a magnetic field in the vorticity direction.

Emulsions can often be manipulated in many ways. However, due to the high surface energy of the interface, they tend to be thermodynamically unstable (Maphosa; Jideani, 2018). One alternative to overcome this problem and to make them stable is to use surfactants (surface active agents) to reduce the interfacial tension. In such cases, the transport of surfactants over the droplet surface results in complex rheological responses, being possible to manipulate characteristics such as bulk viscosity, deformation and surface tension (Pimenta; Oliveira, 2021). The understanding of surfactant dynamics is a useful knowledge in several fields, such as oil recovery, agriculture, or nanotechnology (Tiwari; Mall; Solanki, 2018). Closely related are the Pickering emulsions, but in this case, solid particles are introduced in such a way as to cover the droplet contour, preventing coalescence and stabilizing the emulsion (Jiang; Sheng; Ngai, 2020). Such technology is applicable in many areas, *e.g.*, for drug delivery of non-spherical products (Yang et al., 2017).

An external magnetic field to the emulsion can also be used as a way to manipulate or control an emulsion. This specific emulsion is known as magnetic emulsion, which is a liquid-liquid suspension in which one phase, dispersed or continuous, is magnetically responsive. The most classical example is to use ferrofluid droplets immersed in a non-magnetizable matrix fluid (Cunha et al., 2018; Cunha et al., 2020b; Abicalil et al., 2021; Ishida; Matsunaga, 2020; Abdo et al., 2023), but it is not restricted to this application. Magnetic emulsions can also be composed of oil droplets in ferrofluid (Zakinyan; Dikansky, 2011), with surfactants (Brown et al., 2012) or in magnetic Pickering emulsions (Ma; Zong; Han, 2021). Due to its potential for use in medical treatments (Voltairas; Fotiadis; Massalas, 2001; Mefford et al., 2007; Liu; Li; Lam, 2018), the production of externally controlled materials (Andablo-Reyes; Hidalgo-Álvarez; Vicente, 2011; Vicente; Klingenberg; Hidalgo-Alvarez, 2011; Morillas; Vicente, 2020; Spatafora-Salazar et al., 2021), and applications in Lab-on-a-Chip devices (Sen et al., 2017; Zhang et al., 2019a; Varma et al., 2016; Ray et al., 2017), ferrofluid droplet-based emulsions have been the subject of intense research in recent years. It is possible to actively control the rheology of the materials (Abicalil et al., 2021; Cunha et al., 2018; Cunha et al., 2020b; Ishida; Matsunaga, 2020; Abdo et al., 2023), manipulate it in confined systems (Bijarchi et al., 2021; Roodan et al., 2020; Bijarchi et al., 2020), and actively control heat transfer (Cunha et al., 2020a) by exploring the interaction with external magnetic fields. In addition, new studies have suggested using ferrofluid droplets as liquid microrobots for targeted cargo delivery in microsystems (Fan et al., 2020a; Fan et al., 2020b; Ji et al., 2021; Chen et al., 2021).

Despite the various contexts involving magnetic emulsions, only recently Jesus, Roma and Ceniceros (2018) published a study combining the simultaneous action of simple shear and the external magnetic field in a fully three-dimensional domain. The authors showed the distortions caused by the external magnetic field in the sheared ferrofluid droplet. In addition, they found that at low-intensity external magnetic fields and weak flows, the droplet deformation in the shear plane and the vorticity direction have the same

order. The authors also proposed an equation for the deformation based on the asymptotic small deformation theory. In the same way, using a two-dimensional domain, Hassan, Zhang and Wang (2018) showed that the angle of incidence of the external magnetic field can significantly change the deformation and orientation of the droplet, depending on the intensity of the magnetic field and the shear imposed.

Cunha et al. (2018), using the level-set and projection methods, investigated a ferrofluid droplet under the combined effects of the shear flow and external magnetic field in a two-dimensional domain. The authors showed that the magnetic field can be used to change the viscosity behavior of a magnetic emulsion from shear-thinning to shear-thickening, or vice versa, by changing the field application direction. In addition, for the first time, the authors provided evidence that the magnetic field can change the conditions for droplet rupture in simple shear flows. In the same fashion, Hassan and Wang (2019) explored the breakup problem, but with a wider range of the incidence angle of the external magnetic field. The authors reported that there is a critical magnetic field incident angle and intensity that promotes, or attenuates, the breakup process.

Cunha et al. (2020b) reported a new formulation for calculating the particle stress tensor, accounting for both magnetic and capillary stress jumps on the droplet surface. It was possible to verify small misalignments between the bulk magnetization of the emulsion and the external magnetic field, leading to the appearance of a magnetic torque and an asymmetry in the particle stress tensor, regardless of the superparamagnetic constitution of the ferrofluid droplet.

Ishida and Matsunaga (2020) proposed a three-dimensional model with diluted ferrofluids droplets dispersed in a non-magnetic fluid considering the external magnetic field in each of the coordinate directions. In addition to the great agreement with the results reported by Cunha et al. (2020b), the authors verified the anisotropy of the emulsion, caused by the magnetic field, by calculating the first and second normal stress differences.

Capobianchi et al. (2021) also investigated dilute magnetic emulsions based on a single droplet using direct numerical simulations. The authors corroborated the aforementioned works of Cunha et al. (2020b) and Ishida and Matsunaga (2020) in terms of the imposed dynamics by the external magnetic field and proposed a constitutive equation for the viscosity of the emulsion as a function of the magnetic field.

As previously exposed, recent research has focused on the rheology and magnetization of magnetic emulsions (Cunha et al., 2018; Cunha et al., 2020b; Ishida; Matsunaga, 2020; Capobianchi et al., 2021), as well as the droplet dynamics (Jesus; Roma; Ceniceros, 2018; Hassan; Zhang; Wang, 2018; Hassan; Wang, 2019), both under the combined action of simple shear and a uniform external magnetic field. Additionally, complex structures generated by magnetizable suspended particles under simple or oscillatory shear have received a lot of attention (Cunha; Rosa, 2021; Rosa; Cunha, 2019; Rosa; Cunha, 2020). To the author's knowledge, no research has looked at how the external magnetic field

affects the rheology and magnetization of diluted emulsions subjected to a small amplitude oscillatory shear (SAOS).

In order to fill this gap, a preliminary step of this thesis is the study of magnetic emulsion in simple shear flow with external magnetic fields, which allows comparing the present results with others available in the literature, providing subsidies for the validation of our methodology. This initial step was completed in co-authorship with other researchers and published in Physics of Fluids in 2021 (Abicalil et al., 2021). In this work, in addition to the proposed validation, the authors also reported the first three-dimensional study in which it was verified that the magnetization of a suspension of superparamagnetic ferrofluid can be misaligned in relation to the external field, producing internal torques in the material and consequently anisotropy of stresses.

The final step, under the same view of the droplet of ferrofluid suspended in a non-magnetizable and diluted matrix, is to change the input from simple shear to small amplitude oscillatory shear. The numerical simulation is performed in a three-dimensional domain using the level-set and projection methods to capture the droplet interface and solve the Navier-Stokes equations, respectively. The magnetic problem is treated through the classic Maxwell's equations, in which the external magnetic field is generated in each of the coordinate directions, furthermore, the magnetic problem is assumed to be quasi-stationary, such that no electric currents are induced. We investigated the droplet dynamics by analyzing its periodic deformation and orientation according to the instantaneous shear imposed. In order to describe the droplet viscoelastic properties and the capacity of the magnetic field to induce stress anisotropy, we looked at the droplet shape between the low and high-frequency limits. We also looked at the oscillatory magnetic torque caused by the angle between the external magnetic field and the emulsion magnetization. As far as the authors know, such results have not been reported before. We discovered that the external magnetic fields can increase or decrease the storage and loss moduli as functions of frequency, direction and intensity of the magnetic field. Moreover, especially when the magnetic field is oriented perpendicular to the shear plane, the imposed flow dynamics cause a change in droplet relaxation time. We also show, by studying the magnetization properties, that, despite the superparamagnetic ferrofluid droplet, there is a periodic component of the magnetization signal which is not in-phase with the imposed strain, revealing that the intrinsic interaction between surface tension, shear stress, and magnetic field results in a finite magnetic relaxation time. These results have been published in the Journal of Fluid Mechanics in 2023 (Abdo et al., 2023).

The remainder of this thesis is organized as follows. Chapter 3 presents the problem statement, the complete description of the small amplitude oscillatory shear and magnetic emulsions, including the governing equation, non-dimensional parameters and rheological properties. Chapter 4 presents the numerical method, going through the level-set and projection methods, mesh discretization, boundary conditions and numerical solvers. Chapter 5 presents the validation in simple shear, a qualitative and quantitative validation

concerning droplet breakup and the main results of this thesis in small amplitude oscillatory shear. Lastly, in Chapter 7 we presented a discussion about the future work.

3 Mathematical formulation

3.1 Problem statement

The problem analyzed consists of a superparamagnetic (Rosensweig, 2013) and spherical ferrofluid droplet with initial radius a, suspended in a continuous phase composed of a non-magnetizable fluid. The emulsion is inside a channel with dimensions L_x, L_y, and L_z where the upper and lower plates oscillate in opposite directions with angular frequency, ω, producing an oscillatory shear flow with shear-rate amplitude, $\dot{\gamma}_0$. The velocity, u, produced by the plates over time, is a function of both $\dot{\gamma}_0$ and ω, so each plate moves with velocity equals to $|u| = (\dot{\gamma}_0/2)\cos(\omega t)L_y$. The other boundaries are taken as periodic in order to prevent problems caused by finite sizes. It is worth mentioning that the strain amplitude is set to $\gamma_0 = 0.1$ to ensure the SAOS regime, also, the problem is studied for a dilute emulsion, in the creeping flow limit.

Additionally, both phases have the same viscosity, η, which implies a viscosity ratio of $\lambda = \eta_d/\eta_c = 1$. The droplet surface is assumed to be free of tensioactive substances with a constant surface tension coefficient, σ. Furthermore, the ferrofluid droplet interacts with an external uniform magnetic field $\boldsymbol{H}_0$, which can be parallel to either the main flow direction (x), the main velocity gradient direction (y), or the main vorticity direction (z). The continuous phase has magnetic permeability μ_0, assumed to be equal to that of free space, and, based on the magnetic permeability ratio, set to $\zeta = \mu_d/\mu_0 = 2$ (Flament et al., 1996), the disperse phase has magnetic permeability $\mu_d = \zeta\mu_0$.

The magnetic problem is assumed to be quasi-stationary, such that no electric currents are induced, and once both phases have the same density ρ, the system has neutral buoyancy. Moreover, the phases are assumed to be incompressible, *i.e.,* the divergence of velocity is zero, $\nabla.\mathbf{u} = 0$. From this perspective, the problem can be consistently described by the incompressible Navier-Stokes equations augmented by a continuum surface force to represent a ferrofluid droplet interface, and a magnetic force term, as well.

The interface-capturing method makes use of an implicit function defined for all $\mathbf{x} \in \mathbb{R}^n$ where the zero isocontour represents the interface, $\phi(\mathbf{x}) = 0$. This computational technique was first introduced by Osher and Sethian (1988), counting on great numerical advantages and the calculation of the geometric properties of the droplet, such as the

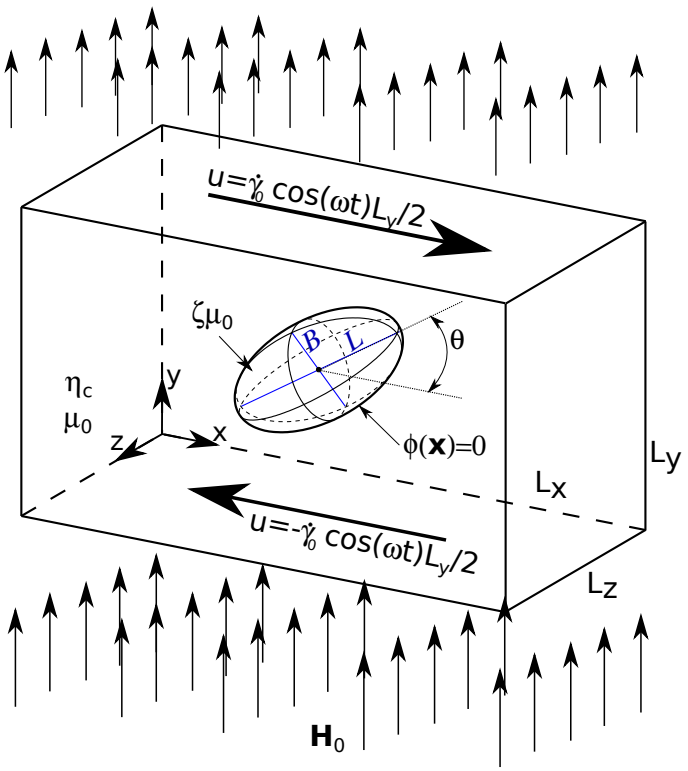

Figure 3.1 – Schematic illustration of the problem for the external magnetic field, $\boldsymbol{H}_0$, parallel to the main velocity gradient direction (y). The domain is of finite size $L_x \times L_y \times L_z$. The magnetic permeability of the continuous and the ferrofluid phases are, respectively, μ_0 and $\zeta\mu_0$. A shear flow is imposed on the system by the top and bottom walls moving in opposite directions with velocity $|u| = \dot{\gamma}_0 \cos(\omega t) L_y/2$. The droplet surface is determined by the Level Set function $\phi(\boldsymbol{x}) = 0$. The droplet is shown in a deformed state with major and minor axes lengths L and B. The droplet's inclination angle is θ.

curvature, κ. In order to illustrate the proposed study, Fig. 3.1 presents a schematic drawing of the problem for the external magnetic field in the main velocity gradient direction.

Since the droplet deforms into an ellipsoidal shape, properties such as the Taylor deformation, $D = (L - B)/(L + B)$, and the droplet inclination angle (relative to the x-axis), θ, can be accurately calculated taking advantage of the symmetry of the inertia tensor, where the eigenvalues are associated with the principal axis: the major, L, and minor, B, axis.

Finally, considering that any change in the boundary conditions is instantly perceived everywhere in the flow due to the Stokes flow condition in the droplet scale, the rheological properties can be estimated based on the bulk and particle stress tensor proposed by Batchelor (1970). As a consequence, such viscoelastic properties, as G' and G'', which decompose the time-dependent particle stress into an in-phase and an out-of-phase component with respect to the shear, can be calculated with the aid of a fast Fourier transform (FFT). In parallel, the magnetization properties can be estimated as bulk quantities, as well, such as the emulsion magnetization and magnetic torques.

3.2 Small amplitude oscillatory shear

The oscillatory shear experiment is one of the most popular tests employed in order to study the viscoelastic response of the emulsion on different time scales. In the case of the small amplitude oscillatory shear, there is a relatively small strain amplitude to ensure the linear viscoelastic region, which is given by

$$\gamma = \gamma_0 \sin(\omega t)\,, \tag{3.1}$$

where the velocity profile will be nearly linear in y if $\omega\rho L_y^2/2\eta_0 \ll 1$, which is half of the ratio between the vorticity diffusion time scale ($L_y^2\rho/\eta$) and oscillation time scale ($1/\omega$), for η_0 being the zero-shear-rate viscosity (Bird; Armstrong; Hassager, 1987). For an emulsion composed of two Newtonian phases, the stress response, in this case, is neither in-phase with the strain (perfectly elastic solid) nor 90° out-of-phase (Newtonian fluid), but is somewhere in between, leading to an in-phase, G', and out-of-phase, G'', components.

These facts show that a given material can respond with a predominantly elastic behavior when the elastic modulus, G', is greater than the loss modulus, G'', and vice versa. In the same way, it is possible to observe this behavior on η', and η'' viscosities. Basically, $G' \to G$ (elastic modulus), $G'' \to 0$, for a Hookean solid and $\eta' \to \eta$, $\eta'' \to 0$, for a Newtonian fluid.

Based on the Maxwell's model, it is worth mentioning that by solving his equation for G' and G'' it is possible to find the relaxation time when $G' = G''$. Taking into account this fact, many authors estimate the relaxation time of the system as the inverse of the angular frequency right on the cross-over point between the curves for G' and G" (Graebling; Muller; Palierne, 1993; Tadros, 1994).

Palierne (1990) also developed an analytical solution for dilute emulsions, which successfully describes the viscoelastic properties of a large variety of non-Newtonian fluids (Bousmina, 1999; Liao et al., 2020; Boudoukhani; Moulai-Mostefa; Hammani, 2020). According to his model and assuming trivial surface dilatation modulus and surface shear modulus, the complex shear modulus for a homogeneous dilute emulsion is given by (Pal, 2011)

$$G_e^*(\omega) = G_c^*(\omega) + 5\beta G_c^*(\omega) H^*(\omega)\,, \tag{3.2}$$

where β is the volume fraction, G_c^* is the complex shear modulus of the continuous phase, and the second term on the right-hand side accounts for the dispersed phase contribution. The term $H^*(\omega)$ is given by

$$H^*(\omega) = \frac{(G_d^* - G_c^*)(19G_d^* + 16G_c^*) + (4\sigma/a)(5G_d^* + 2G_c^*)}{(2G_d^* + G_c^*)(19G_d^* + 16G_c^*) + (40\sigma/a)(G_d^* + G_c^*)}\,. \tag{3.3}$$

Under the assumption that both phases are Newtonian and $\lambda = 1$, they share the same complex shear modulus $\omega\eta i$, with $i = \sqrt{-1}$. In this case, Eq. 3.2 reduces to

$$G_e^*(\omega) = G_c^*(\omega) + \beta G_c^*(\omega)\frac{28\sigma/a}{35G_c^*(\omega) + 16\sigma/a}\,. \tag{3.4}$$

It is interesting to note the term σ/a, in Eq. 3.4, is the one-half of the pressure difference across the fluid interface for a spherical droplet, according to the Young–Laplace equation. This fact gives us a great intuition about the time scale of the present phenomena and would be of great importance in Sec. 3.5.

3.3 Magnetic emulsions

The magnetic problem is based on two conditions: the first one considers a superparamagnetic ferrofluid droplet, which means that this specific material can be much more magnetizable for the same magnetic field than paramagnetic materials. The property that measures this behavior is called magnetization, $\mathbf{M}$, which denotes the orientation and how polarized magnetic matter is. The second point is the quasi-stationary condition, where no electric currents are induced. Furthermore, the relaxation time of the magnetic field is considered to be negligible with respect to fluid flow and droplet motion.

For a magnetic emulsion submitted to an external magnetic field, $\mathbf{H}_0$, the induction field is the sum of the contribution of the impressed magnetizing field and the local magnetization, given by

$$\mathbf{B} = \mu_0(\mathbf{H} + \mathbf{M})\,. \tag{3.5}$$

But for a superparamagnetic material, with constant magnetic susceptibility, χ, the magnetization is proportional to the applied magnetic field, $\mathbf{M} = \chi\mathbf{H}$. To generalize this definition throughout the entire domain, since the emulsion is also composed of a non-magnetizable continuous phase, we define χ as a function of the position vector, $\mathbf{x}$, giving the Eq. 3.5 a different form

$$\mathbf{B} = \mu_0(1 + \chi(\mathbf{x}))\mathbf{H} = \mu(\mathbf{x})\mathbf{H} = \mu_0\zeta(\mathbf{x})\mathbf{H}\,, \tag{3.6}$$

for $\mu(\mathbf{x}) = \mu_0(1 + \chi(\mathbf{x}))$ and $\zeta(\mathbf{x}) = \mu(\mathbf{x})/\mu_0$. Here, $\zeta(\mathbf{x})$, is also a position-dependent variable, differently from $\zeta = \mu_d/\mu_0$, defined in the Problem statement (see Sec. 3.1). $\zeta(\mathbf{x}) = 1$ outside the ferrofluid material and ζ (or $1+\chi$) inside.

This formulation leads to the Kelvin force per unit of volume form (or magnetic force per unit of volume)

$$\mathbf{F}_{mag} = \mu_0\mathbf{M}.\nabla\mathbf{H} = \mu_0(\zeta(\mathbf{x}) - 1)\mathbf{H}.\nabla\mathbf{H}\,. \tag{3.7}$$

With aid of the following identity

$$\nabla\left[\frac{1}{2}\mu_0 H^2(\zeta(\mathbf{x})-1)\right] = \mu_0(\zeta(\mathbf{x})-1)[\mathbf{H}.\nabla\mathbf{H} + \mathbf{H}\times(\nabla\times\mathbf{H})] + \frac{1}{2}\mu_0 H^2\nabla\zeta(\mathbf{x})\,, \quad (3.8)$$

and the fact that the applied magnetic field is irrotational, *i.e*, $\nabla\times\mathbf{H} = 0$ (Ampère-Maxwell law), equation 3.7 is now given by

$$\mathbf{F}_{mag} = \nabla\left[\frac{1}{2}\mu_0 H^2(\zeta(\mathbf{x})-1)\right] - \frac{1}{2}\mu_0 H^2\nabla\zeta(\mathbf{x})\,, \quad (3.9)$$

note that the first term in the right-hand side of Eq. 3.9 accounts for a magnetic pressure and plays no role other than ensuring a divergence-free velocity. In addition, a surface force density appears due to the step change in $\zeta(\mathbf{x})$ at the interface.

Additionally, once $\nabla\times\mathbf{H} = 0$, it is possible to associate $\mathbf{H}$ with a scalar potential, ψ, in the form $\mathbf{H} = \nabla\psi$. Furthermore, making use of the solenoidal condition of $\mathbf{B}$ (Gauss's law) in Eq. 3.6, the magnetic potential can the obtained from the following relation

$$\nabla.(\mu_0\zeta(\mathbf{x})\nabla\psi) = 0. \quad (3.10)$$

Equations 3.7 and 3.9 reveal an important result that is relevant in an attempt to describe the behavior of a magnetic material. The force per unit of volume can be described as a function of the stress tensor, $\nabla.\Sigma_{mag} = \mathbf{F}_{mag}$, which leads, for a magnetic fluid, to a general form of the Maxwell stress tensor (Rosensweig, 2013) for the present study

$$\mathbf{\Sigma}_{mag} = -\frac{1}{2}\mu_0\mathbf{H}^2\mathbf{I} + \mathbf{BH}\,, \quad (3.11)$$

note that the spherical term corresponds to the magnetic pressure.

3.4 Two-phase model for incompressible flow

Considering the problem exposed in Fig. 3.1, we can divide the domain into two distinct regions, the disperse phase, Ω_d, and the continuous phase, Ω_c. The volume occupied by the whole domain is represented by the union of both fluids, $\Omega = \Omega_c \cup \Omega_d$, and the interface is a film that coexists between the phases, $\partial\Omega = \Omega_c \cap \Omega_d$.

Both fluids are incompressible, and the continuous phase can be expressed by the classical viscous stress tensor (Batchelor, 2000). In the case of the dispersed phase, the equivalent stress tensor is the sum of the viscous and the magnetic stress tensor, in Eq. 3.11. In this sense, it is possible to define

$$\mathbf{\Sigma}_{\Omega_c} = -p_h\mathbf{I} + 2\eta_c\mathbf{D}\,, \quad (3.12)$$

$$\boldsymbol{\Sigma}_{\Omega_d} = -\left(p_h + p_{mag}\right)\mathbf{I} + 2\eta_d\mathbf{D} + \mathbf{BH}\,, \tag{3.13}$$

where p_h and p_{mag} accounts for the hydrodynamic and magnetic pressure, respectively, $\boldsymbol{\Sigma}$ is the second-order stress tensors, $\mathbf{I}$ is the unit second-order tensor and $\mathbf{D}$ is the second-order rate of deformation tensor.

It is worth mentioning that, similar to $\zeta(\mathbf{x})$, the viscosity is also a position-dependent variable. Tanking this fact into account, it is possible to generalize both constitutive equations in such a way as to accommodate all these terms in a continuum model, as proposed by many authors (Cunha et al., 2018; Cunha et al., 2020b; Abicalil et al., 2021)

$$\rho(\mathbf{x})\frac{D\mathbf{u}}{Dt} = -\nabla p + \nabla.(2\eta(\mathbf{x})\mathbf{D}) + \mu_0(\zeta(\mathbf{x}) - 1)\mathbf{H}.\nabla\mathbf{H} - \sigma\kappa\hat{\mathbf{n}}\delta(min|\mathbf{x} - \mathbf{x}_{\partial\Omega}|)\,. \tag{3.14}$$

Equation 3.14 is the result of the momentum balance in Ω. It is possible to notice that the local viscosities, η_c and η_d, were changed by a position-dependent one, $\eta(\mathbf{x})$, *i.e.*, $\eta(\Omega_c) = \eta_c$ and $\eta(\Omega_d) = \eta_d$. Also, to apply the localization theorem, the surface integral of the Young-Laplace equation was transformed into a volume integral by inserting the Dirac delta function.

From these points, the emulsion can be represented by a continuum model. For example, in the continuous phase, $\zeta(\Omega_c) = 1$ and $\delta(\Omega_c) = 0$, we have a purely Newtonian fluid with viscosity η_c, on the other hand, in the dispersed phase, $\zeta(\Omega_d) = \zeta$ and $\delta(\Omega_d) = 0$, revealing a magnetic fluid with viscosity η_d. Finally, if we are in the interface $\delta(\partial\Omega) = 1$.

3.5 Non-dimensional form

The non-dimensional parameters proposed are based on the droplet relaxation time scale, given by: $\mathbf{u}^* = \mathbf{u}\eta_c/\sigma$, $t^* = t\sigma/\eta_c a$, $\mathbf{x}^* = \mathbf{x}/a$, $p^* = pa/\sigma$, $\lambda^*(\mathbf{x}) = \eta(\mathbf{x})/\eta_c$, $\rho^*(\mathbf{x}) = \rho(\mathbf{x})\rho_c$, $\mathbf{H}^* = \mathbf{H}/|\mathbf{H}_0|$, $\kappa^* = a\kappa$, $\delta(\mathbf{x})^* = a\delta(\mathbf{x})$, $\mathbf{D}^* = \mathbf{D}\eta_c a/\sigma$ and $\nabla^* = a\nabla$.

It is worth mentioning that, as commented in Sec. 3.2, the non-dimensional parameter for the pressure, p, is the same as presented in the Palierne model, which corroborates the adoption of the droplet time scale, furthermore, other authors, such as Oliveira and Cunha (2015), also used the same time scale for similar problems. Remembering that the problem is neutral buoyancy and $\lambda = 1$, substituting each value in Eq. 3.14 and suppressing, for convenience, the superscript * we have

$$\begin{aligned}\frac{\partial\mathbf{u}}{\partial t} + \mathbf{u}.\nabla\mathbf{u} = -\frac{Ca}{Re}\nabla p + \frac{Ca}{Re}\nabla.(2\mathbf{D}) + \frac{CaCa_{mag}}{Re}(\zeta(\mathbf{x}) - 1)\mathbf{H}.\nabla\mathbf{H} \\ -\frac{Ca}{Re}\kappa\delta[min(|\mathbf{x} - \mathbf{x}_{\partial\Omega}|)]\hat{\mathbf{n}}\,,\end{aligned} \tag{3.15}$$

where

$$Re = \frac{\rho_c \dot{\gamma}_0 a^2}{\eta_c}, \tag{3.16}$$

is the ratio between fluid momentum force to viscous shear force, known as the Reynolds number,

$$Ca = \frac{\eta_c a \dot{\gamma}_0}{\sigma}, \tag{3.17}$$

the capillary number, corresponding to the ratio between viscous and capillary forces and

$$Ca_{mag} = \frac{\mu_0 a H_0^2}{\sigma}, \tag{3.18}$$

the magnetic capillary number is the ratio between magnetic and capillary forces. The velocity and strain are in each wall, respectively

$$\mathbf{u} = \frac{Ca}{2}\cos(\omega t) L_y, \tag{3.19}$$

$$\gamma = \frac{Ca}{2\omega}\sin(\omega t) L_y, \tag{3.20}$$

where it is possible to identify the non-dimensional shear and strain-rate amplitude as Ca and Ca/ω, respectively. Also, the non-dimensional version of Eq. 3.4 is given by

$$G_e^*(\omega) = G_c^*(\omega) + \frac{28\beta G_c^*(\omega)}{35 G_c^*(\omega) + 16}\,. \tag{3.21}$$

It is worth noting that the term Ca/Re is present in practically all terms of Eq. 3.15, lighting the mechanisms acting in the present problem. In fact, the term Ca/Re can also be described by the Ohnesorge number as Oh^2. This non-dimensional group represents the ratio between the viscous and surface tension forces. As the Ohnesorge number increases, the more dominant becomes the internal viscous dissipation, conversely, when Oh decreases, the input energy is converted into surface tension energy (Li, 2008).

3.6 Bulk stress tensor and stress jump

According to Batchelor (Batchelor, 1970), the bulk stress tensor is defined as

$$\mathbf{\Sigma}_b = \frac{1}{V}\int_{\Omega_c} -pdV\mathbf{I} + \frac{1}{V}\int_{\Omega_c} \eta_c(\nabla\mathbf{u} + \nabla\mathbf{u}^T)dV + \mathbf{\Sigma}^D\,, \tag{3.22}$$

where Σ^D is the particle stress tensor expressed by (Oliveira, 2007)

$$\mathbf{\Sigma}^D = \frac{1}{V}\int_{\partial\Omega}[\mathbf{x}\Delta\mathbf{f} + \eta_c(\lambda - 1)(\mathbf{u}\hat{\mathbf{n}} + \hat{\mathbf{n}}\mathbf{u})]d\Omega, \tag{3.23}$$

and $\Delta\mathbf{f} = (\mathbf{\Sigma}_{\Omega_c} - \mathbf{\Sigma}_{\Omega_d}).\mathbf{n}$ is the stress jump across the droplet surface.

Recalling that Eq. 3.9 reduces to a surface force, the jump across the interface is the balance between capillary and magnetic forces (Cunha et al., 2020b)

$$\Delta\mathbf{f} = \sigma\kappa\hat{\mathbf{n}} + \frac{1}{2}\mu_0 H^2 \nabla\zeta(\mathbf{x})\,, \tag{3.24}$$

Substituting Eq. 3.24 in Eq. 3.23

$$\boldsymbol{\Sigma}^D = \frac{1}{V}\int_{\partial\Omega}\left[\mathbf{x}\left(\sigma\kappa\hat{\mathbf{n}} + \frac{1}{2}\mu_0 H^2\nabla\zeta(\mathbf{x})\right) + \eta_c(\lambda-1)(\mathbf{u}\hat{\mathbf{n}} + \hat{\mathbf{n}}\mathbf{u})\right] d\Omega\,. \tag{3.25}$$

A fundamental point to evaluate Eq. 3.25 is to expand the term $\zeta(\mathbf{x})$. In this case, we replaced it by $\zeta(\phi) = \zeta + (1-\zeta)H(\phi)$, where ϕ is the level-set function (see Sec. 4.1), which associates to each $\mathbf{x}$, a positive Euclidean distance to the interface for points outside the droplet, and a negative one for points inside the droplet. H is the classical Heaviside function, which is set to 1 $\forall\phi \in \Omega_c$ and 0 otherwise.

Consequently, $\nabla\zeta(\mathbf{x}) = (1-\zeta)\delta(\phi)\hat{\mathbf{n}}$, where δ is the Dirac delta function. In this way, it is worth noting that $\lambda = 1$ and Eq. 3.25 is evaluated over the surface, where $\delta(\phi = 0)$, leading to the non-dimensional, scaled by σ/a, bulk and particle stress tensor

$$\boldsymbol{\Sigma}_b = -\frac{1}{V}\int_{\Omega_c} pdV\mathbf{I} + \frac{1}{V}\int_{\Omega_c}(\nabla\mathbf{u} + \nabla\mathbf{u}^T)dV + \boldsymbol{\Sigma}^D\,, \tag{3.26}$$

$$\boldsymbol{\Sigma}^D = \frac{1}{V}\int_{\partial\Omega}\left[\mathbf{x}\left(\kappa - \frac{Ca_{mag}}{2}(\zeta-1)\mathbf{H}^2\right)\hat{\mathbf{n}}\right] d\Omega\,. \tag{3.27}$$

Given the creeping flow limit, where the vorticity spreads instantly throughout the domain, it is worth mentioning that the particle stress tensor in Eq. 3.27 applies to non-steady regimes, as well. Accordingly, any change in the boundary conditions is immediately felt throughout the flow (Oliveira; Cunha, 2015). If the Stokes flow condition can be assumed in the droplet scale, then Eq. 3.27 can be utilized to compute the particle stress in the SAOS regime.

Based on the previous paragraph, the right-hand side of Eq. 3.21, which accounts for the viscoelastic contribution of the dispersed phase, can be compared using the in-phase and out-of-phase components extracted from the yx component of Eq. 3.27. Similarly, properties such as the first and second normal stress difference can be evaluated by simply taking $N_1 = \Sigma^D_{xx} - \Sigma^D_{yy}$ and $N_2 = \Sigma^D_{yy} - \Sigma^D_{zz}$.

3.7 Droplet geometrical properties

In order to study the geometric properties of the droplet, such as D and θ, shown in Fig. 3.1, it is necessary, assuming the ellipsoidal shape of the droplet (Yu; Bousmina,

2003; Maffettone; Minale, 1998) to extract its semi-axes. The non-dimensional inertia tensor, I^*, is given by

$$\mathbf{I}^* = \int_V (\mathbf{r}^2\mathbf{I} - \mathbf{rr}) dV \,. \tag{3.28}$$

where $\mathbf{r}$ is the Euclidean distance from the centroid of the droplet.

In this case, $\mathbf{I}^*$ is also symmetric, allowing its decomposition according to its eigenvalues and eigenvectors, which, in turn, determines the lengths of the axes of the ellipsoid. For the case where two of the eigenvalues are equal, there is an ellipsoid of revolution, if all are equal, the ellipsoid is a sphere. Once Eq. 3.28 is computed and its eigenvalues, Λ_1, Λ_2 and Λ_3, are extracted, it is possible to solve the following system, based on the non-dimensional moments of inertia of an ellipsoid, to find the lengths, L, B and C, of the semi-axes.

$$\begin{cases} \Lambda_1 = \frac{V}{5}(L^2 + B^2) \\ \Lambda_2 = \frac{V}{5}(B^2 + C^2) \\ \Lambda_3 = \frac{V}{5}(C^2 + L^2) \,. \end{cases} \tag{3.29}$$

Finally, since the largest eigenvalue corresponds to the minor axis of the ellipsoid, and the smallest corresponds to the major axis, θ is found based on the dot product between the vector $(1, 0, 0)$ and the major semi-axis on the shear plane. Alternatively, it is possible to use trigonometric properties to find θ.

4 Numerical methodology

4.1 Level-set

Osher and Sethian (Osher; Sethian, 1988) proposed the Level-Set method based on the implicit description of surfaces so that the interface has a codimension one (Osher; Fedkiw, 2003). The Level-Set function can be chosen to be any Lipschitz continuous function, but in practice, the signed distance function provides improved properties such as mass conservation and accuracy in geometrical parameters (Gibou; Fedkiw; Osher, 2018). In this way, defining a signed distance function $d = min(|\mathbf{x} - \mathbf{x}_{\partial\Omega}|)$, the Level-Set function is, then

$$\phi(\mathbf{x}) = \begin{cases} -d \text{ for } \mathbf{x} \in \Omega_d \\ d \text{ for } \mathbf{x} \in \Omega_c \\ 0 \text{ for } \mathbf{x} \in \partial\Omega \end{cases} \tag{4.1}$$

Imagining an arbitrary point in Ω, the relation between ϕ and d is

$$\phi(\mathbf{x})^2 = (\mathbf{x} - \mathbf{x}_{\partial\Omega})^2 \,, \tag{4.2}$$

taking the gradient and simplifying

$$\nabla\phi(\mathbf{x})\phi(\mathbf{x}) = (\mathbf{x} - \mathbf{x}_{\partial\Omega}) \,, \tag{4.3}$$

using the following identity $\phi(\mathbf{x})\hat{\mathbf{n}} = \mathbf{x} - \mathbf{x}_{\partial\Omega}$

$$\nabla\phi(\mathbf{x}) = \frac{\phi(\mathbf{x})\hat{\mathbf{n}}}{\phi(\mathbf{x})} = \hat{\mathbf{n}} \,, \tag{4.4}$$

$$|\nabla\phi(\mathbf{x})| = 1, \,, \tag{4.5}$$

which is one of the main properties of the Level-Set function and makes it possible to write

$$\hat{\mathbf{n}} = \nabla\phi \,, \tag{4.6}$$

$$\kappa = \nabla . (\nabla \phi) \ . \tag{4.7}$$

In the previous example, the Level-Set function could be written as $\phi(\mathbf{x}) = \sqrt{x^2 + y^2} - a$. The same logic could be used to expand this argument to a surface in $\mathbb{R}^4$ with the zero contour in $\mathbb{R}^3$.

Since Eq. 3.15 is continuous throughout the domain, it is necessary, to avoid discontinuities across the interface, to smooth the functions responsible for identifying each phase, such as the Heaviside, briefly presented in Sec. 3.7, and the Dirac delta function. Both smoothed function are given by (Gibou; Fedkiw; Osher, 2018; Dijk et al., 2013)

$$H_\epsilon(\phi) = \begin{cases} 0 & \text{for } \phi < -\epsilon \,, \\ \frac{1}{2} + \frac{\phi}{2\epsilon} + \frac{1}{2\pi} \sin\left(\frac{\pi\phi}{\epsilon}\right) & \text{for } -\epsilon \leq \phi \leq \epsilon \,, \\ 1 & \text{for } \epsilon < \phi \,, \end{cases} \tag{4.8}$$

$$\delta_\epsilon(\phi) = \begin{cases} 0 & for\ \phi < -\epsilon \,, \\ \frac{1}{2\epsilon} + \frac{1}{2\epsilon} \cos\left(\frac{\pi\phi}{\epsilon}\right) & for\ -\epsilon \leq \phi \leq \epsilon \,, \\ 0 & for\ \epsilon < \phi \,, \end{cases} \tag{4.9}$$

where ϵ is the size of the bandwidth and is defined as $\epsilon = 1.5\Delta x$ (Δx in this case means that ϵ is proportional to the mesh size).

By using both Eqs. 4.8 and 4.9, surface and volume integral in each phase can be calculated according to Eq. 4.11 and 4.10 (Peng et al., 1999), respectively

$$\int_{\Omega_c} f(\mathbf{x}) H_\epsilon(\phi(\mathbf{x})) dV \ , \ \int_{\Omega_d} f(\mathbf{x}) H_\epsilon(-\phi(\mathbf{x})) dV \,, \tag{4.10}$$

$$\int_{\partial\Omega} f(\mathbf{x}) \delta_\epsilon(\phi(\mathbf{x})) |\nabla\phi(\mathbf{x})| dV \,, \tag{4.11}$$

with aid of the 27-point stencil integral (Solomenko et al., 2017)

$$\int_{\Omega_{i,j,k}} f d\Omega \approx \frac{\Delta x \Delta y \Delta z}{78} \left(52 f_{i,j,k} + \sum_{l=-1}^{1} \sum_{m=-1}^{1} \sum_{n=-1}^{1} \alpha_{l,m,n} f_{i+l,j+m,k+n} \right) \,, \tag{4.12}$$

where $\alpha_{l,m,n} = 0$ if $l = m = n = 0$, and $\alpha_{l,m,n} = 1$ otherwise.

Since there is no transport, the evolution of ϕ can be described by an advection equation

$$\frac{\partial \phi}{\partial t} + \mathbf{u} \cdot \nabla \phi = 0 \,, \tag{4.13}$$

but as the interface moves, the level-set function does not retain its original properties and progressively deviates from the actual signed distance function and its properties,

periodically requiring a reinitialized to keep ϕ equal to the signed distance. Many models are described in the literature to solve properly and with accuracy, such as Crossing Times (Osher, 1993), Fast Marching Method (Tsitsiklis, 1995; Tsitsiklis, 1994), Fast Sweeping Method (Wong; Leung, 2016), using Hopf-Lax formula (Darbon; Osher, 2016; Royston et al., 2018) or High-order Constrained Reinitialization (Hartmann; Meinke; Schröder, 2010). In this work, we use a method described by Peng et al. (1999) with a mass correction algorithm reported by Sussman and Fatemi (1999).

This methodology consists of creating a narrow band around the interface to summarize the calculations only in that location. The first region consists of all points where $|\phi(\mathbf{x})| < \gamma$, being γ the size of the narrow band. Since the zero contour moves less than one grid point, the second region is composed of the points where $|\phi(\mathbf{x}+\mathbf{y})| < \gamma;\ |y| < \Delta x$, *i.e.*, the borderlines of the tubes. Figure 4.1A shows the narrow band while Fig. 4.1B the droplet position. Note that all red region has $|\phi| < \gamma$ and the border has a different color. This separation is purposeful once ϕ is updated over time only in the red region. After the creation of the narrow band, the new Level-Set function becomes

$$\phi^{new} = \begin{cases} -\gamma & if\ \phi < \gamma\,, \\ \phi & if\ |\phi| \leq \gamma\,, \\ \gamma & if\ \phi > \gamma\,. \end{cases} \tag{4.14}$$

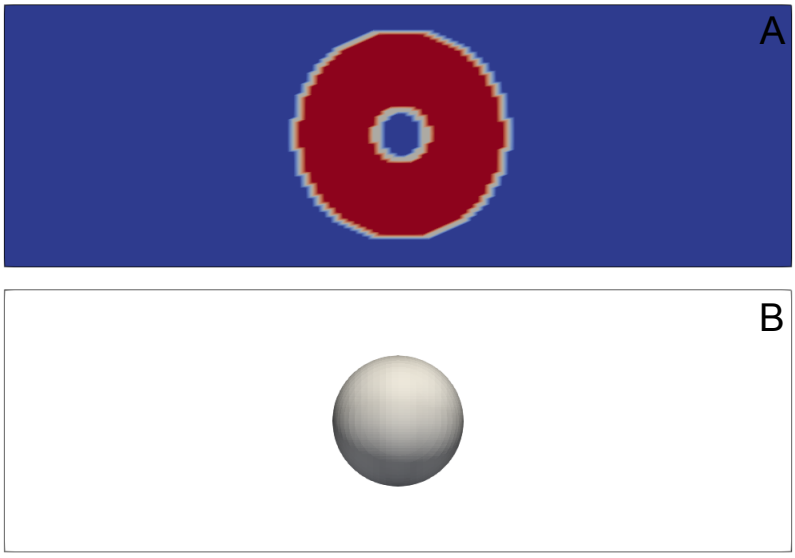

Figure 4.1 – Narrow band and droplet position from a real simulation. Figure A shows the region where the tubes are placed and Fig. B the position of the droplet.

That way, instead of calculating the update of ϕ across the entire domain, the solution is focused where it is needed, saving time and making possible costly simulations. Additionally, the Eq. 4.13 is smoothed by a cut-off function to prevent numerical oscillations at the tube boundary, as shown

$$\frac{\partial \phi}{\partial t} + c(\phi)\mathbf{u} \cdot \nabla \phi = 0\,, \tag{4.15}$$

$$c(\phi) = \begin{cases} 1 & if\ |\phi| \leq \beta\,, \\ (|\phi| - \gamma)^2(2|\gamma| + \gamma - 3\beta)/(\gamma - \beta)^3 & if\ |\beta| < |\phi| \leq \gamma\,, \\ 0 & if\ |\phi| > \beta\,, \end{cases} \tag{4.16}$$

for $\gamma = 6\Delta x$ and $\beta = 3\Delta x$.

When necessary, the routine of the program can be interrupted so that the distortions originated from Eq. 4.15 are corrected. Therefore, Eq. 4.17 is solved, considering the borderlines of Fig. 4.1, until it reaches a steady state

$$\frac{\partial \phi}{\partial\, \tau} + S(\phi_0)(|\nabla \phi| - 1) = 0\,, \tag{4.17}$$

where τ is the virtual time and the subscript 0 denotes the initial Level-Set fuction and $S(\phi_0)$ is given by

$$S(\phi) = \frac{\phi}{\sqrt{\phi^2 + |\nabla \phi|^2 (\Delta x)^2}}\,. \tag{4.18}$$

After solving Eq. 4.17, a correction factor, given by Eq. 4.19, is applied to each grid point i, j, k to minimize any mass conservation problem and then updates ϕ.

$$\lambda_{i,j,k} = -\frac{\int_{\Omega_{i,j,k}} \delta_\epsilon(\phi) \left(\frac{\phi^{n+1} - \phi^n}{\Delta t}\right) dV}{\int_{\Omega_{i,j,k}} \delta_\epsilon^2(\phi) |\nabla \phi| dV}\,. \tag{4.19}$$

In summary, first Eqs. 4.15 and 4.17, in this order, are solved using a third-order TVD Runge-Kutta (Shu; Osher, 1988; Shu; Osher, 1989) with aid of a fifth-order WENO (Liu; Osher; Chan, 1994; Jiang; Shu, 1996; Jiang; Peng, 2000) to compute ϕ^n and ϕ^{n+1}, respectively. The decision to use a TVD-RK algorithm is due to the ability to solve conservation laws without introducing oscillations near discontinuities (Olsson; Kreiss; Zahedi, 2007). Then, Eq. 4.19 is used to compute $\lambda_{i,j,k}$ for each grid point and finally the Level-Set function is corrected using $\phi^{n+1} + \Delta\tau\lambda\delta_\epsilon(\phi)|\nabla\phi|$.

(4.20)

4.2 Projection Method

Based on the Helmholtz-Hodge Decomposition (HHD), Chorin and Téman (Chorin, 1968; Témam, 1969a; Témam, 1969b) reported a non-incremental pressure-correction

scheme using a first-order time stepping and finite-difference method. The first step is to approximate the velocity ignoring the irrotational term in the Navier-Stokes equation, followed by the Poisson equation.

Using a second-order semi-backward difference formula (SBDF2) described by Badalassi et al. (Badalassi; Ceniceros; Banerjee, 2003) and substituting the position-dependent variables by the Level-Set function, the projection method of Eq. 3.15 is

$$\frac{1}{2\Delta t}\left(3\mathbf{u}^{*}-4\mathbf{u}^{n}+\mathbf{u}^{n-1}\right)-\frac{Ca}{Re}\nabla^{2}\mathbf{u}^{*}=\mathbf{G}(\hat{\mathbf{u}})+\mathbf{F}_{C}(\hat{\phi})+\mathbf{F}_{M}(\hat{\phi},\hat{H})\,, \tag{4.21}$$

$$\mathbf{u}^{n+1}=\mathbf{u}^{*}-\frac{2Ca\Delta t}{3Re}\nabla(q^{n+1})\,, \tag{4.22}$$

$$\nabla^{2}q^{n+1}=\frac{3Re}{2Ca\Delta t}\nabla\cdot\mathbf{u}^{*}, \tag{4.23}$$

$$p^{n+1}=q^{n+1}-\nabla\cdot\mathbf{u}^{*}, \tag{4.24}$$

where $\mathbf{G}$, $\mathbf{F}_c$ and $\mathbf{F}_{mag}$ are, respectively, the viscous and convective terms, capillary force and magnetic force.

$$\mathbf{G}(\hat{\mathbf{u}})=-\hat{\mathbf{u}}\cdot\nabla\hat{\mathbf{u}}-\frac{Ca}{Re}\nabla^{2}\hat{\mathbf{u}}+\frac{Ca}{Re}\nabla\cdot\left[(\nabla\hat{\mathbf{u}}+\nabla\hat{\mathbf{u}}^{T})\right], \tag{4.25}$$

$$\mathbf{F}_{c}(\hat{\phi})=-\frac{Ca}{Re}\kappa(\hat{\phi})\delta_{\epsilon}(\hat{\phi})|\nabla\hat{\phi}|\hat{\mathbf{n}}, \tag{4.26}$$

$$\mathbf{F}_{mag}(\hat{\phi},\hat{\mathbf{H}})=\frac{CaCa_{mag}}{Re}[(\zeta(\hat{\phi})-1)\hat{\mathbf{H}}.\nabla\hat{\mathbf{H}}]. \tag{4.27}$$

The semi-implicit method used here works quite well for diffusion-dominated equations. It consists of summing and subtracting the term $\frac{Ca}{Re}\nabla^{2}\mathbf{u}$, treating implicitly one and explicitly the other. As shown in Sec. 3.7, $\zeta(\phi)$ is smoothed in the form $\zeta(\phi)=\zeta+(1-\zeta)H_{\epsilon}(\phi)$. Finally, the hat symbol $\hat{}$ corresponds to a second order extrapolation in the form $\hat{\mathbf{u}}=2\mathbf{u}^{2}-\mathbf{u}^{n-1}$. As a side note, even though Eq. 4.26 is similar to the equivalent term in Eq. 3.15, there is no direct correspondence between $\delta(min(|\mathbf{x}|-\mathbf{x}_{\partial\Omega}))$ and $\delta(\phi)$. This relation can be proven noting that (Osher; Fedkiw, 2003)

$$\delta(d) = \nabla H(\phi(d)) \cdot \hat{\mathbf{n}}\,, \tag{4.28}$$

where $\nabla H(\phi(d)) = \delta(\phi)\nabla\phi$, resulting in

$$\delta(d) = \delta(\phi)\nabla\phi \cdot \frac{\nabla\phi}{|\nabla\phi|} = \delta(\phi)|\nabla\phi|\,. \tag{4.29}$$

4.3 Discretization and boundary conditions

As long as the proposed problem aims to achieve a second-order scheme, using a colocated grid is not an option due to the difficulty with pressure-velocity coupling when a central difference is used. One way of correcting this problem for simple geometries is to calculate velocity and pressure at different points using a staggered mesh (Ferziger; Perić, 1999; Anderson, 1995; McKee et al., 2008).

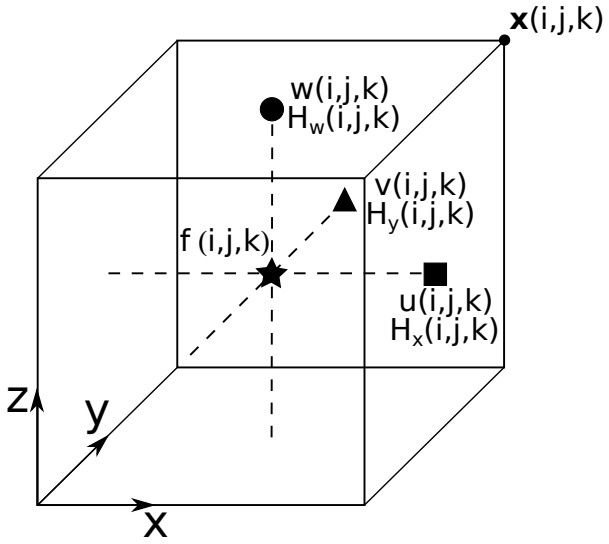

Figure 4.2 – Three-dimensional unit cell of a staggered grid with the distribution of vectors and scalar functions.

Figure 4.2 shows a standard unit of the mesh with the respective positions of the parameters. The vectors $\mathbf{u}$ and $\mathbf{H}$ are distributed according to their components, and scalar quantities are, symbolically represented by $f(i,j,k)$, located in the center of the cell. With the variable centered at cell faces normal to their directions, both pressure gradient or divergence of velocity can now be calculated avoiding the checkerboard problem.

Based on this scheme, equations described in Sec. 4.2 are now discretized using centered second-order finite differences, except for the advective term, $\mathbf{u}\cdot\nabla\mathbf{u}$, which uses a second-order essentially non-oscillatory (ENO) scheme with upwinding (Osher; Fedkiw, 2003). The discretization process of Eqs. 4.21, 4.24 and 3.10 leads, for example, to following systems for the velocity, pressure and the magnetic potential in the x-direction, respectively

$$a_{i,j,k}u^*_{i-1,j,k}+b_{i,j,k}u^*_{i,j-1,k}+c_{i,j,k}u^*_{i,j,k-1}+d_{i,j,k}u^*_{i,j,k}+e_{i,j,k}u^*_{i+1,j,k}+f_{i,j,k}u^*_{i,j+1,k}+g_{i,j,k}u^*_{i,j,k+1} = h_{i,j,k}\,, \tag{4.30}$$

for

$$\begin{aligned}
a_{i,j,k} &= -\frac{Ca\Delta t}{Re\Delta x^2}\,,\\
b_{i,j,k} &= -\frac{Ca\Delta t}{Re\Delta y^2}\,,\\
c_{i,j,k} &= -\frac{Ca\Delta t}{Re\Delta z^2}\,,\\
d_{i,j,k} &= \frac{3}{2} + \frac{2Ca\Delta t}{Re\Delta x^2} + \frac{2Ca\Delta t}{Re\Delta y^2} + \frac{2Ca\Delta t}{Re\Delta z^2}\,,\\
e_{i,j,k} &= -\frac{Ca\Delta t}{Re\Delta x^2}\,,\\
f_{i,j,k} &= -\frac{Ca\Delta t}{Re\Delta y^2}\,,\\
g_{i,j,k} &= -\frac{Ca\Delta t}{Re\Delta z^2}\,,\\
h_{i,j,k} &= 2u^n_{i,j,k} - \frac{u^{n-1}_{i,j,k}}{2} + \Delta t[\mathbf{F}_v(\hat{u},\hat{\phi}) + \mathbf{F}_c(\hat{\phi}) + \mathbf{F}_{mag}(\hat{\phi}, H_x)]\,,
\end{aligned} \tag{4.31}$$

$$a_{i,j,k}q_{i-1,j,k}+b_{i,j,k}q_{i,j-1,k}+c_{i,j,k}q_{i,j,k-1}+d_{i,j,k}q_{i,j,k}+e_{i,j,k}q_{i+1,j,k}+f_{i,j,k}q_{i,j+1,k}+g_{i,j,k}q_{i,j,k+1} = h_{i,j,k}\,, \tag{4.32}$$

$$\begin{aligned}
a_{i,j,k} &= \frac{1}{\Delta x^2}\,,\\
b_{i,j,k} &= \frac{1}{\Delta y^2}\,,\\
c_{i,j,k} &= \frac{1}{\Delta z^2}\,,\\
d_{i,j,k} &= -\frac{2}{\Delta x^2} - \frac{2}{\Delta y^2} - \frac{2}{\Delta z^2}\,,\\
e_{i,j,k} &= \frac{1}{\Delta x^2}\,,\\
f_{i,j,k} &= \frac{1}{\Delta y^2}\,,\\
g_{i,j,k} &= \frac{1}{\Delta z^2}\,,\\
h_{i,j,k} &= \frac{3Re}{2Ca\Delta t}\left(\frac{u^*_{i,j,k} - u^*_{i-1,j,k}}{\Delta x} + \frac{v^*_{i,j,k} - v^*_{i,j-1,k}}{\Delta y} + \frac{w^*_{i,j,k} - w^*_{i,j,k-1}}{\Delta z}\right)\,,
\end{aligned} \tag{4.33}$$

$$a_{i,j,k}\psi_{i-1,j,k}+b_{i,j,k}\psi_{i,j-1,k}+c_{i,j,k}\psi_{i,j,k-1}+d_{i,j,k}\psi_{i,j,k}+e_{i,j,k}\psi_{i+1,j,k}+f_{i,j,k}\psi_{i,j+1,k}+g_{i,j,k}\psi_{i,j,k+1} = h_{i,j,k}\,, \tag{4.34}$$

where

$$
\begin{aligned}
a_{i,j,k} &= \frac{\zeta_{i-1/2,j,k}}{\Delta x^2}\,, \\
b_{i,j,k} &= \frac{\zeta_{i,j-1/2,k}}{\Delta y^2}\,, \\
c_{i,j,k} &= \frac{\zeta_{i,j,k-1/2}}{\Delta z^2}\,, \\
d_{i,j,k} &= -\left(\frac{\zeta_{i-1/2,j,k}+\zeta_{i+1/2,j,k}}{\Delta x^2}+\frac{\zeta_{i,j-1/2,k}+\zeta_{i,j+1/2,k}}{\Delta y^2}+\frac{\zeta_{i,j,k-1/2}+\zeta_{i,j,k+1/2}}{\Delta z^2}\right), \\
e_{i,j,k} &= \frac{\zeta_{i+1/2,j,k}}{\Delta x^2}\,, \\
f_{i,j,k} &= \frac{\zeta_{i,j+1/2,k}}{\Delta y^2}\,, \\
g_{i,j,k} &= \frac{\zeta_{i,j,k+1/2}}{\Delta z^2}\,. \\
h_{i,j,k} &= 0
\end{aligned}
\tag{4.35}
$$

Finally, the velocity and pressure are updated according to Eqs. 4.22 and 4.24

$$
u^{n+1}_{i,j,k} += u^{*}_{i,j,k} - \frac{2Ca\Delta t}{3Re}\frac{q^{n+1}_{i+1,j,k}-q^{n+1}_{i,j,k}}{\Delta x}\,, \tag{4.36}
$$

$$
p^{n+1} = q^{n+1}_{i,j,k} - \left(\frac{u^{*}_{i,j,k}-u^{*}_{i-1,j,k}}{dx}+\frac{v^{*}_{i,j,k}-v^{*}_{i,j-1,k}}{dy}+\frac{w^{*}_{i,j,k}-w^{*}_{i,j,k-1}}{dz}\right), \tag{4.37}
$$

and the unit normal vector and curvature are given by

$$
n_x(\hat{\phi}_{i,j,k}) = \frac{\frac{\hat{\phi}_{i+1,j,k}-\hat{\phi}_{i-1,j,k}}{2\Delta x}}{\sqrt{\left(\frac{\hat{\phi}_{i+1,j,k}-\hat{\phi}_{i-1,j,k}}{2\Delta x}\right)^2+\left(\frac{\hat{\phi}_{i,j+1,k}-\hat{\phi}_{i,j+1,k}}{2\Delta y}\right)^2+\left(\frac{\hat{\phi}_{i,j,k+1}-\hat{\phi}_{i,j,k+1}}{2\Delta z}\right)^2}} \tag{4.38}
$$

$$
\kappa(\hat{\phi}) = \frac{n_x(\hat{\phi}_{i+1,j,k})-n_x(\hat{\phi}_{i-1,j,k})}{2\Delta x}+\frac{n_y(\hat{\phi}_{i,j+1,k})-n_y(\hat{\phi}_{i,j-1,k})}{2\Delta y}+\frac{n_z(\hat{\phi}_{i,j,k+1})-n_z(\hat{\phi}_{i,j,k-1})}{2\Delta z}\,, \tag{4.39}
$$

4.4 Boundary conditions

Concerning the boundary conditions, Fig. 4.3 shows, schematically, a macro view of all these imposed constraints. The planes normal to y are composed of a Dirichlet

boundary condition for velocity, which is given by Eq. 3.19 and Neumann boundary condition for pressure and magnetic field, given by $\nabla p = 0$ and $\nabla \psi = \mathbf{H}_0$. Furthermore, impenetrability and no-slip constraints are present, as well. Eq. 4.40 summarizes all these imposed conditions for both $\mathbf{u}$ and $\mathbf{u}^*$.

$$\begin{cases} \mathbf{u}^* \cdot \mathbf{n}|_{\partial\Omega} = \mathbf{u}^{n+1} \cdot \mathbf{n}|_{\partial\Omega} \,, \\ \mathbf{t} \cdot \mathbf{u}^*|_{\partial\Omega} = \mathbf{t} \cdot \left(\mathbf{u}^{n+1} + \frac{2Ca\Delta t}{3Re} \nabla (2q^n - q^{n-1}) \right) \,, \\ \mathbf{u}^{n+1} \cdot \mathbf{n}|_{\partial\Omega} = 0 \,. \end{cases} \tag{4.40}$$

where $\mathbf{t}$ represents the tangential vector to the plane.

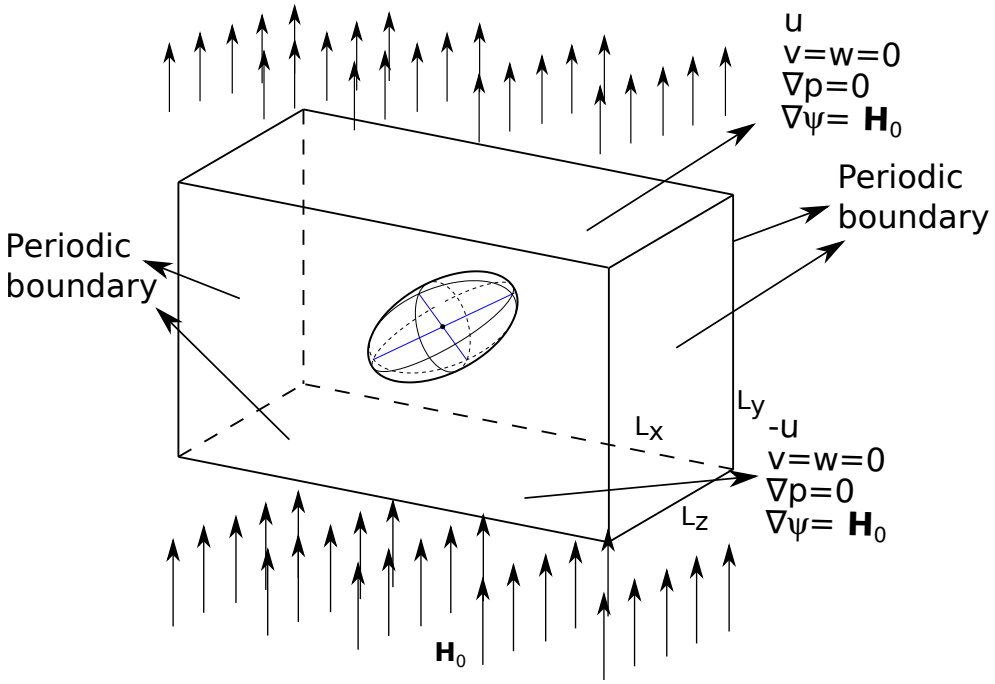

Figure 4.3 – Boundary conditions.

For planes normal to x and z there are periodic boundary conditions, which means that the respective edges are connected. In this case, for example, for elements whose derivatives are made using a second-order ENO, it is necessary to expand the mesh beyond the domain contours, as shown

$$\begin{aligned} u_{0,j,k} &= u_{nx,j,k} \,, \\ u_{i-1,j,k} &= u_{nx-1,j,k} \,, \\ u_{i-2,j,k} &= u_{nx-2,j,k} \,, \\ u_{nx+1,j,k} &= u_{1,j,k} \,, \\ u_{nx+2,j,k} &= u_{2,j,k} \,, \end{aligned} \tag{4.41}$$

where nx is the number of nodes (including zero). For a variable that makes use of fifth-order WENO, for example

$$
\begin{aligned}
\phi_{0,j,k} &= \phi_{nx,j,k}\,, \\
\phi_{i-1,j,k} &= \phi_{nx-1,j,k}\,, \\
\phi_{i-2,j,k} &= \phi_{nx-2,j,k}\,, \\
\phi_{i-3,j,k} &= \phi_{nx-3,j,k}\,, \\
\phi_{nx+1,j,k} &= \phi_{1,j,k}\,, \\
\phi_{nx+2,j,k} &= \phi_{2,j,k}\,, \\
\phi_{nx+3,j,k} &= \phi_{3,j,k}\,,
\end{aligned}
\tag{4.42}
$$

For all other cases, such as q

$$
\begin{aligned}
q_{0,j,k} &= q_{nx,j,k}\,, \\
q_{nx+1,j,k} &= q_{1,j,k}\,,
\end{aligned}
\tag{4.43}
$$

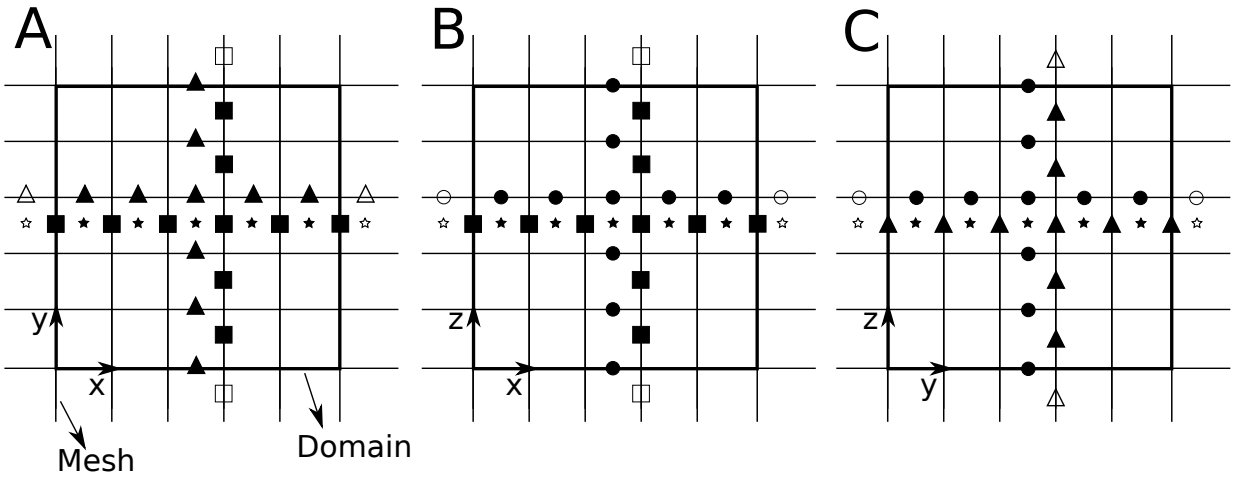

Figure 4.4 – Example of the distribution of variables and ghosts in the xy (A), xz (B) and yz (C) planes of the staggered mesh.

Figure 4.4 shows an exemplified distribution of the vectors and scalar fields in each plane, where Fig. 4.4A shows the xy plane, Fig. 4.4B the xz plane and Fig. 4.4C the yz plane.

Focusing on the xy plane, as shown in Fig. 4.4A, it is possible to see empty symbols outside the boundary denoting a ghost node, which is essential to compute the centered derivatives and solve the linear systems. All other planes in Fig. 4.4 present the same layout with their respective variables. In this case, to impose the boundary conditions on the wall we use a simple arithmetic mean between the point inside and the ghost, for example

$$
\frac{u_{ghost} + u_{inside}}{2} = u_{wall} \rightarrow u_{ghost} = 2u_{wall} - u_{inside}\,. \tag{4.44}
$$

Applying for u^* on the upper wall, Eq. 4.30 becomes

$$\begin{aligned} a_{i,j,k}u^*_{i-1,j,k} + b_{i,j,k}u^*_{i,j-1,k} + c_{i,j,k}u^*_{i,j,k-1} + (d_{i,j,k} - f_{i,j,k})u^*_{i,j,k} + \\ e_{i,j,k}u^*_{i+1,j,k} + f_{i,j,k}(2u^*_{wall}) + g_{i,j,k}u^*_{i,j,k+1} = h_{i,j,k}\,. \end{aligned} \tag{4.45}$$

Since we know u^*_{wall} (Eq. 4.40), it is possible to impose the boundary conditions that will enable the solution of the linear system. A similar situation happens for pressure and magnetic field.

4.5 Numerical solvers

In this work, there are two types of linear systems to be solved: the first follows the pattern of the Poisson equation, as in Eq. 4.23, which results in the linear system arranged in Eq. 4.32. Similarly, the linear system of Eq. 4.30 shares the same properties. One of the biggest problems is that this operation takes most of the time in the projection method. In order to alleviate this problem, a method called Fast Poisson Solver (FPS) was developed. This technique combines fast Fourier transforms (FFT) and Gauss elimination, resulting in a tridiagonal system of equations, which can be readily solver using a TDMA algorithm (Thomas algorithm) (Dodd; Ferrante, 2014).

The second type of linear system to be solved is the one in Eq. 4.34, for the magnetic potential. In this specific case, ζ is not constant over the domain, making the use of the FPS algorithm unfeasible. However, it is possible to use another efficient solver that uses the conjugate gradient algorithm with multigrid preconditioning (McAdams; Sifakis; Teran, 2010).

Once we set $\Delta x = \Delta y = \Delta z$ the coefficients of the linear system are constant. Thus, both Eqs. 4.30 and 4.32 can be simplified to

$$a(q_{i-1,j,k} + q_{i+1,j,k}) + b(q_{i,j-1,k} + q_{i,j+1,k}) + c(q_{i,j,k-1} + q_{i,j,k+1}) + dq_{i,j,k} = h_{i,j,k}\,. \tag{4.46}$$

The suitable Fourier transform for periodic boundaries in x and z is given by (Press et al., 1992)

$$q_{i,j,k} = \frac{1}{PL}\sum_{m=0}^{P-1}\sum_{n=0}^{L-1}\hat{\hat{q}}_{m,j,n}e^{-2\pi iim/p}e^{-2\pi ikn/L}\,, \tag{4.47}$$

$$h_{i,j,k} = \frac{1}{PL}\sum_{m=0}^{P-1}\sum_{n=0}^{L-1}\hat{\hat{h}}_{m,j,n}e^{-2\pi iim/p}e^{-2\pi ikn/L}\,, \tag{4.48}$$

where P and L are the last periodic nodes in the x and y direction, respectively.

Substituting Eqs. 4.47 and 4.48 in Eq. 4.46 and simplifying, it is possible to achieve the following tridiagonal systems of equations

$$b\hat{\hat{q}}_{m,j-1,n} + \left[2a\cos\left(\frac{2\pi m}{P}\right) + 2c\cos\left(\frac{2\pi n}{L}\right) + d\right]\hat{\hat{q}}_{m,j,n} + b\hat{\hat{q}}_{m,j+1,n} = \hat{\hat{h}}_{m,j,n}\,, \tag{4.49}$$

which can be solved using the TDMA algorithm. To recover the solution in the time domain, it is necessary to apply the inverse FFT.

The second method employs a multigrid cycle, denominated as V-Cycle, as a preconditioner for the conjugate gradient method. One of the biggest advantages of this method is that using a V-Cycle algorithm enables a purely geometric scheme, ensuring robustness and speed.

The V-Cycle algorithm is based on the fact that if the residual is smooth in a coarse grid, it is possible to extend the solution to a finer grid, in order to achieve the final solution. In this sense, while the solution is not reached, several interpolation and smoothing operations are performed on the different meshes, from the finest to the coarsest. The solution is then calculated on the coarsest grid and the process is reversed to the finest mesh carrying the solution. Finally, this solution is used as a preconditioner for the conjugate gradient method. The entire method and the detailed algorithms are well described by McAdams, Sifakis and Teran (2010) and Abicalil (2021).

5 Results and discussions

5.1 Dilute magnetic emulsion under simple shear flow

The present results shown in this section are part of the preliminary step discussed in Ch. 2. The intention here is to show that the proposed methodology is valid and congruent with the literature in simple shear. The mathematical and numerical model was generated using the shear characteristic time, $1/\dot{\gamma}$ (see Appendix A), and a similar methodology as in the SAOS presented in this thesis. The related results and parameters were published in co-authorship in Physics of Fluids 2021 (Abicalil et al., 2021).

In all following cases discussed here, we employ a domain size of $10 \times 10 \times 7.5$ and a corresponding mesh discretization of $128 \times 128 \times 96$ cells. The parameters $\lambda = 1$, $Re = 0.01$ and $\zeta = 2$ are likewise fixed. This domain size is associated with a volume fraction β around 0.56%, which describes a diluted emulsion with negligible magnetic and hydrodynamic interaction between the droplets. To confirm the absence of confinement and mesh refinement effects, tests were conducted in a scenario of large droplet deformation ($Ca = 0.15$, $Ca_{mag} = 12$). We discovered that differences in droplet deformation, droplet inclination angle, and reduced viscosity were all smaller than 3% when comparing the findings obtained with our conventional mesh to those obtained with a more refined mesh of $192 \times 192 \times 144$ cells. In addition, given the aforementioned parameters, comparisons with a domain size of $15 \times 15 \times 11.25$, with the same mesh density, produced differences lower than 1%. As long as Δt is small enough to ensure stability, this parameter has little influence on steady-state results. It is important to note that the analyzed case here coincides with one of the highest droplet deformations. As a result, we are sure that mesh refinement and confinement effects have no impact on the data provided here.

The droplet deformation and inclination angle are shown in Fig. 5.1 as a function of the magnetic capillary number, for different magnetic field directions and capillary numbers. In close accordance with our findings, data from Ishida and Matsunaga (2020) are shown alongside our results. The agreement indicates that both strategies are properly capturing the magnetic and hydrodynamic components of the problem given that the two studies employ distinct numerical approaches.

The magnetic forces at the interface stretch the droplet in the respective direction

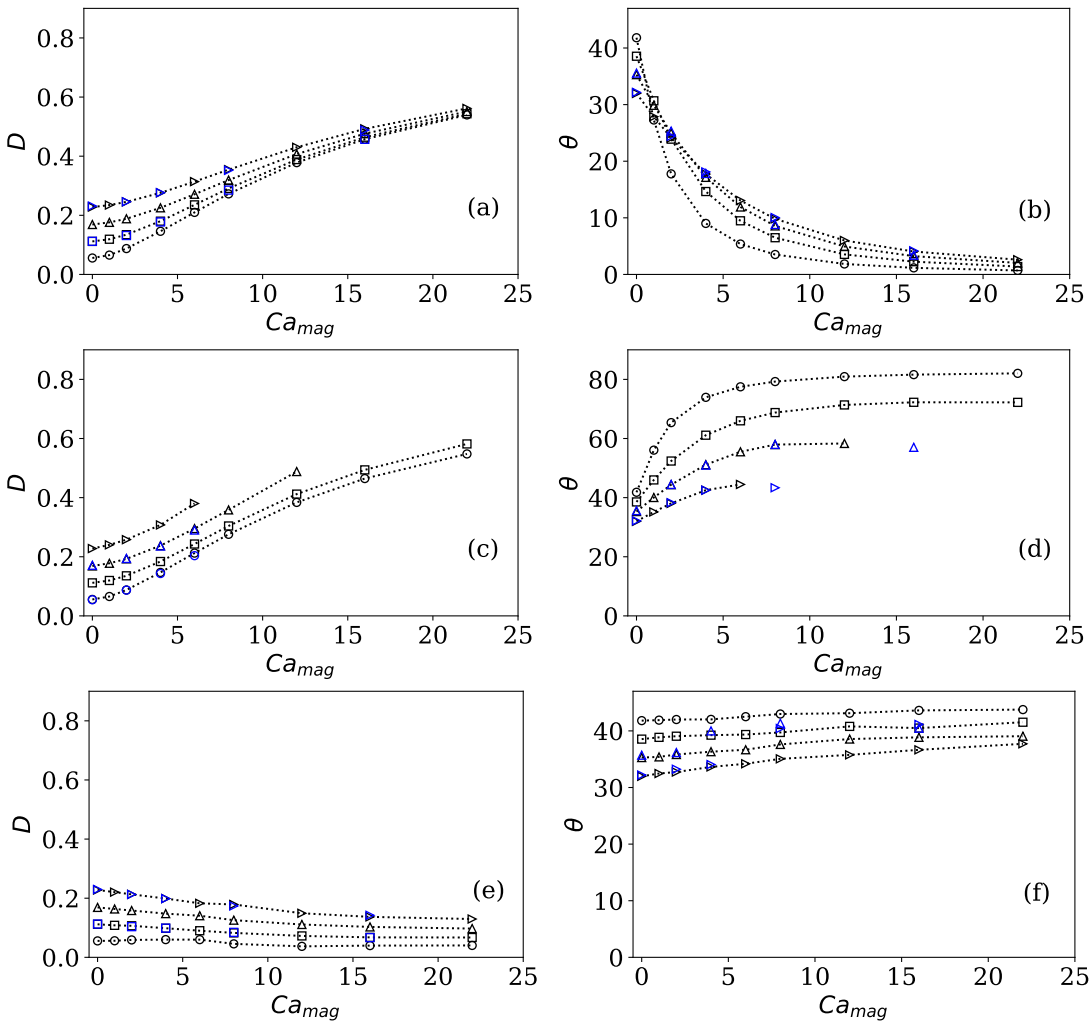

Figure 5.1 – Droplet deformation, D, and inclination angle, θ, as a function of Ca_{mag}, for different values of Ca. Figures (a) and (b): external magnetic field in the x direction; (c) and (d): y direction; (e) and (f): z direction. Black markers represent the results from the present study and the blue markers represent the results of Ishida and Matsunaga(Ishida; Matsunaga, 2020). Circles correspond to $Ca = 0.05$, squares to $Ca = 0.10$, triangles to $Ca = 0.15$, and right-pointing triangle to $Ca = 0.20$.

of the external magnetic field, allowing active control of the droplet inclination and deformation. The droplet deformation and inclination under an external magnetic field in the x-direction are shown in Figs. 5.1a and 5.1b, respectively. One can see that the droplet deformation changes dramatically over the range of magnetic capillary numbers up to modest magnetic field strengths ($Ca_{mag} \approx 10$). The curves for various values of Ca begin to converge when the values of Ca_{mag} rise above this point, demonstrating that the magnetic stresses have a major influence on the droplet form. One can notice that with the droplet inclination, increasing values of Ca_{mag} cause the droplet to align with the applied magnetic field. The inclination angle also exhibits non-monotonic behavior. Higher values of Ca result in lesser inclination angles in the absence of magnetic fields ($Ca_{mag} = 0$), but $Ca_{mag} \geq 4$ exhibits the reverse tendency. There is a transition area, represented by intermediate values of Ca_{mag}, where such patterns are less distinct. Smaller values of Ca

allow for greater dominance of the magnetic field, which accounts for the steeper slope of θ. Also, as suggested by Cunha et al. (2020b), at high values of Ca_{mag}, the stronger shear effects, characteristic of larger values of Ca, are more likely to align the droplet at angles closer to those with no external fields.

Shear-induced effects, however, are still important throughout the whole range of the external magnetic field (Ca_{mag}) when applied in the y-direction. Figures 5.1c and 5.1d illustrate this phenomenon showing how the droplet deformation and inclination change considerably with Ca. The primary cause of this behavior is that the droplet is subjected to larger effective shears as it deforms in the direction of the magnetic field, preventing the dominance of the magnetic effects. Shear-induced and magnetic-induced elongations are additive in droplet deformation. As a result, it increases with both Ca and Ca_{mag}, up until the point of breakup (Cunha et al., 2020b). The inclination angle, θ, decreases with Ca and increases with Ca_{mag}. This behavior results from a balance between the magnetic forces that try to align the droplet with the external magnetic field and the shear stresses that attempt to rotate the droplet with the vorticity. It is interesting to observe that subsequent increases in Ca_{mag} only have a little impact on the inclination angle for $Ca_{mag} > 6$. In fact, with $Ca \geq 0.15$, raising Ca_{mag} over 6 may even cause a slight decrease in inclination angle. This phenomenon results from the droplet being stretched along the velocity gradient direction, which causes it to experience a greater effective shear. This increase in effective shear also leads to an earlier onset of droplet breakup, resulting in breakups for the (Ca, Ca_{mag}) pairs $(0.15, 16)$ and $(0.2, 8)$.

As previously stated by Ishida and Matsunaga (2020), the strength of the external magnetic field has only a small impact on the droplet deformation and inclination angle for external magnetic fields in the z-direction, as seen in Figs. 5.1e and 5.1f. The mass conservation results in a decrease in the droplet cross-section in the shear plane as the magnetic effects stretch the droplet in the z-direction. As a result, the droplet is subject to a lower effective shear and greater interfacial forces due to the increased curvature of the interface. Due to the reduced droplet deformations and inclination angles that are closer to 45°, higher values of Ca_{mag} have comparable effects to lowering values of Ca. The findings for θ, when $Ca_{mag} > 5$ for $Ca = 0.20$, and when $Ca_{mag} > 2$ for $Ca = 0.15$, are quite different from those of Ishida and Matsunaga (2020). The findings from Ishida and Matsunaga (2020) have an apparent discontinuity, which is not present in our results. Indeed, these discontinuities can be seen at the point where Ca_{mag} is strong enough to align the ellipsoid major semi-axis in the z-direction, no longer in the shear plane.

In contrast to magnetic fields in the other two directions, magnetic fields in the z-direction can cause a droplet deformation normal to the shear plane, which can result in unique droplet morphologies. The droplet exhibits a prolate geometry comparable to a non-magnetic droplet if the shear-induced deformations are more apparent than the magnetic-induced ones, as for $Ca = 0.3$ and $Ca_{mag} = 1$, for instance. As previously noted by Ishida and Matsunaga (2020), the droplet once again exhibits a prolate shape if the

magnetic-induced deformations are more significant than the shear-induced ones, such as for $Ca = 0.1$ and $Ca_{mag} = 12$, for example. Nevertheless, when both deforming processes are equally strong, as they are when $Ca = 0.6$ and $Ca_{mag} = 16$, the droplet is stretched in two orthogonal directions and distorted into an odd disc-like shape, as illustrated in Fig. 5.2. For the creation of micromaterials with flexible oblate forms, such phenomena may be of great importance (Zhang et al., 2019b).

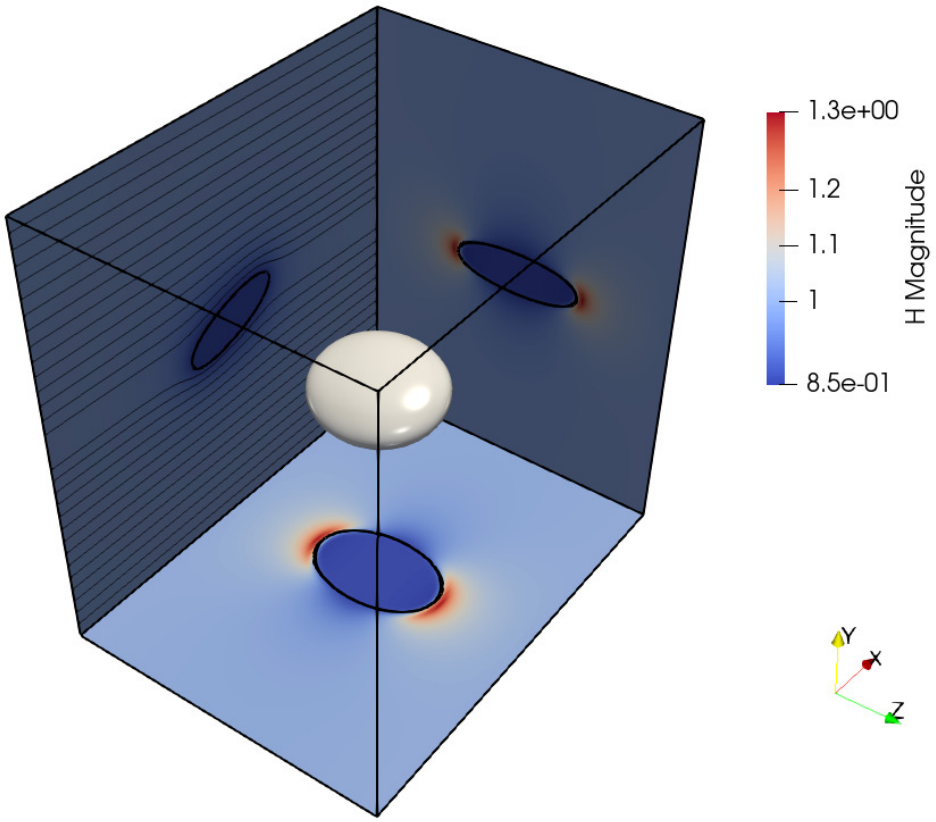

Figure 5.2 – Three-dimensional view of a ferrofluid droplet subjected to an external magnetic field parallel to the main vorticity direction, with slices crossing the droplet center projected to the domain boundaries. $Ca = 0.6$, $Ca_{mag} = 16$.

We also study the influence of the dispersed phase on the emulsion viscosity, defined as a reduced viscosity and given by

$$[\eta] = \frac{\Sigma^D_{yx}}{\beta}\,, \tag{5.1}$$

where Σ^D_{yx} is the shear-stress component of the particle stress, given by Eq. 3.25 and scaled by $\eta\dot{\gamma}$ (See Appendix A), resulting in

$$\mathbf{\Sigma}^D = \frac{1}{L_x L_y L_z}\int_\Omega \left[\left(\frac{\kappa}{Ca} - \frac{Ca_{mag}}{2Ca}(\zeta - 1)H^2\right)\mathbf{x}\hat{\mathbf{n}}\right] d\Omega\,, \tag{5.2}$$

The reduced viscosity is shown in Fig. 5.3 as a function of Ca_{mag} for each of the three external magnetic field directions for $Ca = 0.2$. We confirm a strong agreement between our findings and those of Ishida and Matsunaga (2020), which further supports

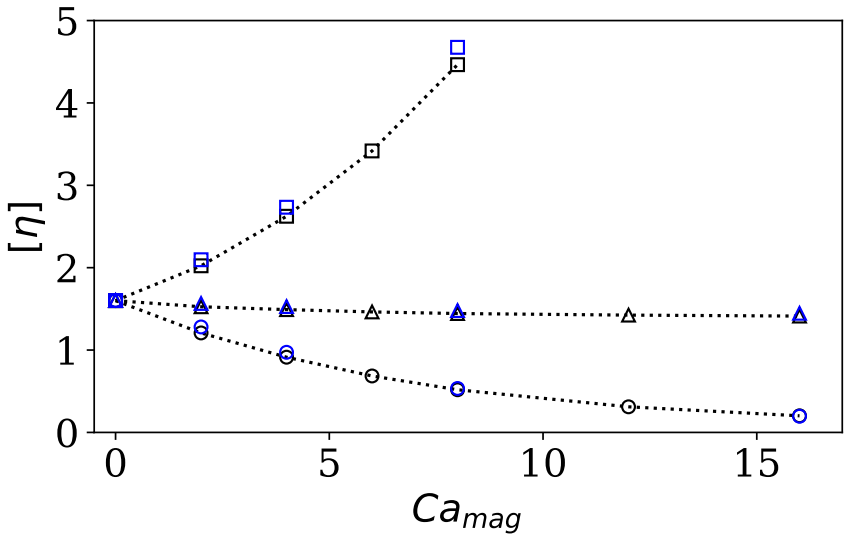

Figure 5.3 – Reduced viscosity $[\eta]$ as a function of Ca_{mag}, for $Ca = 0.2$ and external magnetic fields applied in the x (circles), y (squares), and z (triangles) directions. Black markers represent the results from the present study and blue markers represent the results of Ishida and Matsunaga (2020).

the validity of both approaches for both the droplet geometry and emulsion rheology. There are distinct reduced viscosity behaviors for each direction of the external magnetic field. Stronger magnetic fields cause the reduced viscosity to dramatically increase when the field is oriented in the y-direction. By interacting with areas of higher velocity flow and exhibiting a larger cross-sectional area relative to the flow direction, the droplet assumes a shape that imposes additional resistance to the flow as it is deformed along the magnetic field direction. The behavior of external magnetic fields in the x-direction is the opposite. The droplet assumes a structure that provides less resistance to the flow in this situation as it is deformed along the magnetic field direction. When external magnetic fields are applied in the z-direction, the decreased viscosity of the emulsion is only slightly influenced by variations in magnetic field intensities, with larger values of Ca_{mag} causing a modest reduction in reduced viscosity. As with the shear-thinning behavior of non-magnetic emulsions, this phenomenon is most likely caused by a reduction in the cross-sectional area of the droplet in the shear plane, though some of this effect is likely offset by the stronger capillary forces and their restorative effects on the shape of the droplet.

5.2 Droplet breakup

Droplet breakup is a rich field of research. Many researchers have focused on describing in detail their mechanism, such as the works of Zhao (2007), Vananroye, Puyvelde and Moldenaers (2006), Stone (1992), Barai and Mandal (2016). In this section we focus on presenting a quantitative and qualitative validation, but, more than that, we present the ability of the present algorithm to capture different physical phenomena, in

this case, for variable viscosities (see Appendix B).

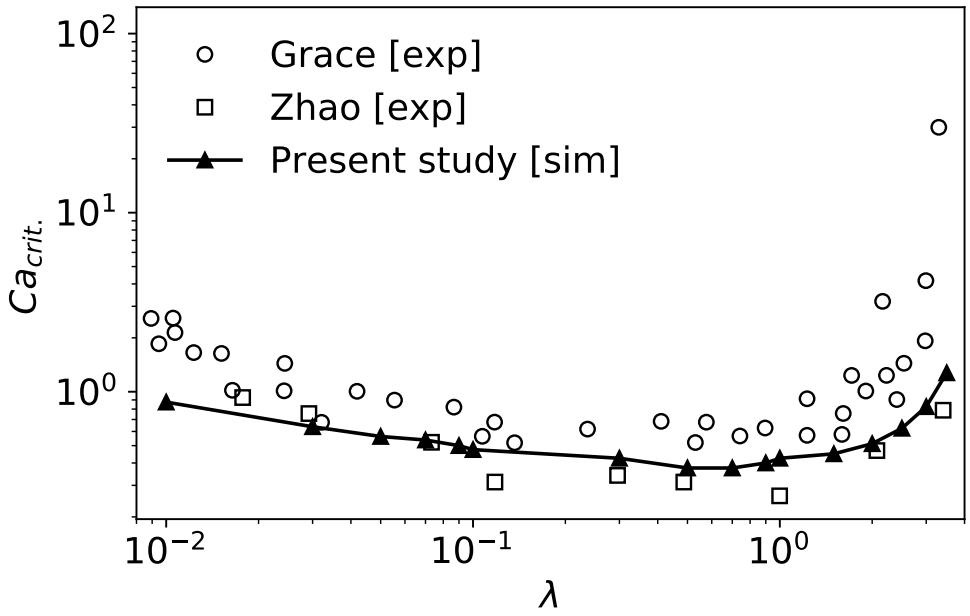

Figure 5.4 – Critical capillary number, Ca_{crit} for $0.01 \leq \lambda \leq 3.5$. Circles denote the work of GRACE (1982), squares the work of Zhao (2007) and the black triangles the present study.

From this perspective, Fig. 5.4 presents a validation of the critical capillarity, which denotes the maximum value of Ca at which the droplet does not break. In Fig. 5.4 it is possible to see the influence of λ on the breakup dynamics and three points of the graph deserve to be highlighted: both the lateral extremes and the minimum point near $\lambda \approx 1$. From the minimum point ($\lambda \approx 1$), as we approach the extreme right of the graph, as λ grows, *i.e.*, the viscosity of the dispersed phase rises several times, the viscous drag imposed by the continuous phase is not enough to elongate the droplet until its breakup (Taylor, 1934). For $\lambda \gtrapprox 3.6$ (Kennedy; Pozrikidis; Skalak, 1994), no matter how high the viscous stresses are, the droplet simply begins to rotate like a rigid body. At the other end, the dispersed phase, now with a viscosity several times lower than the continuous phase, is unable to exert any significant shear stress on the continuous phase, getting a very long, deformed and narrow body (Taylor, 1934; Hinch; Acrivos, 1980). Between these points, there is a transition of both behaviors.

Figure 5.5 shows the evolution of the droplet breakup viewed from the velocity gradient direction. At the first moment, the droplet changes its spherical shape to elongate until narrow necks are formed near the center of the droplet. The instability of the neck leads to the pinching off of the bulbs and the formation of daughter drops separated by smaller satellite drops. This effect is due to the surface tension behavior, which separates the droplet when it reaches high curvature values. Comparing the experiment on the left side of Fig. 5.5 with the simulation on the right side, it is possible to notice that

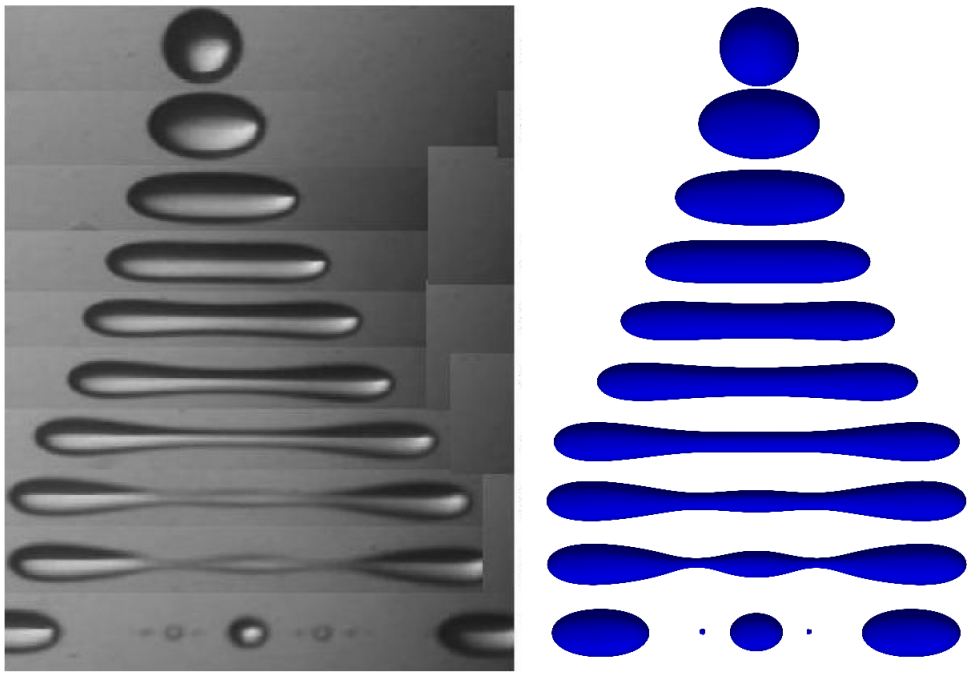

Figure 5.5 – Comparison of droplet breakup seen in the xy plane between the work of Chang-Zhi and Lie-Jin (2007) and the present study for $\lambda = 1$ and $Ca = 0.42$.

the numerical method can capture satisfactorily all the evolution phases of the droplet, including the satellite drops.

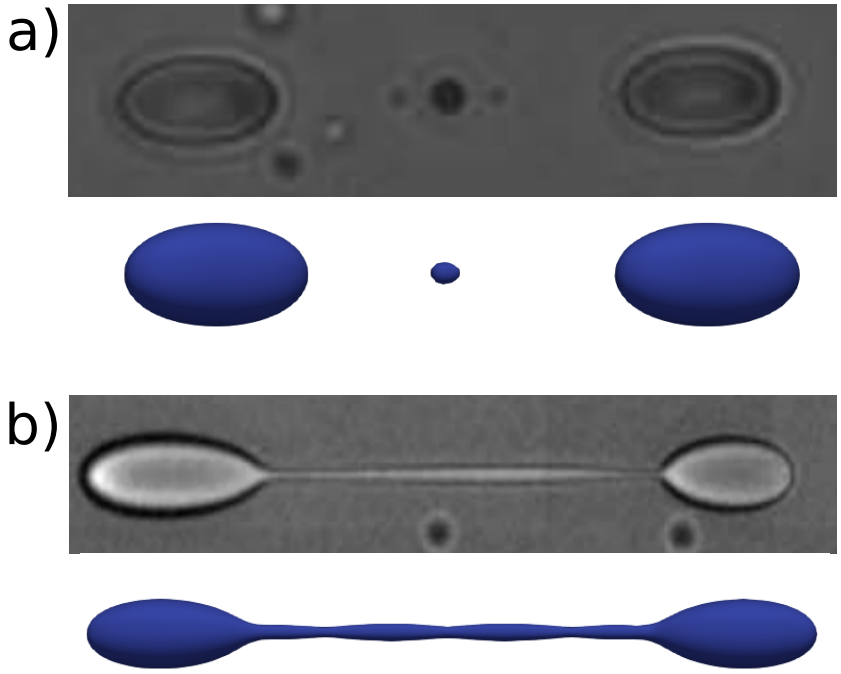

Figure 5.6 – Qualitative comparison between Zhao (2007) experimental results and the present study of the breakup of the droplet seen from the xy plane. (a) represents the results for $\lambda = 0.5$ and (b) for $\lambda = 3.5$

As a final result, we present a qualitative comparison between two distinct deformation phases for $\lambda = 0.5$, Fig. 5.6(a) and 3.5, Fig. 5.6(b). It is possible to observe an

excellent agreement between the experimental results and those produced by simulations in the present study. In Fig. 5.6(a), the simulation was able to reproduce the satellite droplet surrounded by the two other droplets. In the case of Fig. 5.6(b), it is possible to see the link formed between the two lateral drops just before the rupture.

5.3 Dilute magnetic emulsion under SAOS

This section investigates how the ferrofluid droplet responds to a small amplitude oscillatory shear (SAOS) in the presence of a constant external magnetic field. We first examine how the external magnetic field affects the droplet deformation, defined as $D = (L - B)/(L + B)$, where the major and minor axes are L and B, respectively, as shown in Fig. 3.1. Additionally, this analysis includes the inclination angle, θ (see Fig. 3.1), defined as the angle between the major deformation direction in the shear plane and the x-axis. All geometrical measurements taken throughout this work are related to the droplet shape projected in the shear plane, *i.e.*, the xy plane crossing the droplet center. The effects of the external magnetic field on the storage and loss moduli, G' and G'', and the first and second normal stress differences, N_1 and N_2, are then our main concerns. We also present research on how the magnetization of the emulsion reacts to oscillatory strain under various external magnetic field conditions. We calculate the magnetic susceptibility, χ, the angle between the magnetization and the external field, θ_{mag}, and the magnetic torque, $\boldsymbol{\tau}_{mag}$. These values were monitored by their in-phase and out-of-phase components in relation to the strain since they are periodic under oscillatory shear conditions.

All of the investigations in this study were performed on a cubic domain with sides of 8.125, a discretized mesh of $104 \times 104 \times 104$, and a time step of 4×10^{-3}. This domain size is associated with a volume fraction of approximately 0.78 %, which indicates that the emulsion is dilute, *i.e.*, both magnetic and hydrodynamic interactions between the droplets are negligible. As long as $Re = 10^{-3}$ and $\gamma_0 = Ca/\omega = 0.1$, the dimensionless strain amplitude is minimal, inertial effects are negligible, and the flow regime is compatible with the linear viscoelasticity limit. Throughout this work, the magnetic permeability ratio is fixed at $\zeta = 2$.

In order to assure convergence, we assessed how the time step, mesh refinement, and domain size affected the results for $\omega = 10$, $Ca = 1.0$, and $Ca_{mag} = 16$ for the magnetic field oriented in the y-direction. The pair of rheological parameters (G', G''), which are closely related to the geometric characteristics of the droplet, are used as parameters for the following analysis. Using $\Delta t = 1.0 \times 10^{-3}$ as the reference case, we found variations of $(0.413\%, 2.270\%)$ when raising the time step to 4.0×10^{-3} and $(0.978\%, 3.115\%)$ for $\Delta t = 8.0 \times 10^{-3}$. Regarding mesh refinement, we observed relative variations of $(0.710\%, 0.738\%)$ for a mesh of $104 \times 104 \times 104$ cells and $(0.896\%, 2.661\%)$ for a mesh of $64 \times 64 \times 64$ cells, using a mesh of $208 \times 208 \times 208$ cells as the reference case.

Lastly, we concentrated on (G'/β, G''/β) for the investigation of confinement effects. It was identified minor fluctuations of (0.39%, 0.46%) when doubling the domain size from 8.125 to 16.25, retaining the same mesh refinement employed throughout this work. Other variables, such as droplet deformation and inclination angle, showed insignificant variances, as well. Taking into account that these cases were performed for the most critical values of ω and Ca_{mag}, as well as the small variations found for the tested time steps and mesh discretizations, it can be concluded that both time step and mesh discretization used did not significantly affect the results in the subsequent analyses. We can also conclude that confinement effects are minimal based on the domain size investigation.

5.3.1 Verification

The numerical approach utilized in the present study is comparable to that of Abicalil et al. (2021), and it has been shown to be valid for the case of ferrofluid droplets in steady shear flows in the aforementioned work by comparisons with other findings in the literature (Ishida; Matsunaga, 2020). In this study, we compare the proposed approach for oscillatory shear flows to Palierne's analytical solution for dilute emulsions, which successfully explains the viscoelastic characteristics of a wide range of non-Newtonian fluids (Bousmina, 1999; Liao et al., 2020; Boudoukhani; Moulai-Mostefa; Hammani, 2020), and the experimental study of Guido, Grosso and Maffettone (2004).

The contribution of the dispersed phase to the non-dimensional complex shear modulus of the emulsion is given by the right-hand side of Eq. 3.21, *i.e.*, $28\beta G_c^*/(35G_c^*+16)$. By using a Fast Fourier Transform on the periodic signal of Σ_{yx}^D over time, which is given by Eq. 3.27, it is possible to extract both parameters since G' and G'' decompose the time-dependent particle stress into an in-phase and an out-of-phase component with respect to the shear.

The comparison between our numerical findings and Palierne's model for an emulsion composed of Newtonian fluids with the same viscosity and density can be seen in Fig. 5.7. As can be observed, both models exhibit great overall agreement, supporting the validity of our methodology, which also makes use of Batchelor's particle stress approach (Batchelor, 1970). Additionally, we discovered that the intersection of curves for G' and G'' happens at a frequency of $\omega_{cp} = 0.45$, which corresponds to a relaxation time of $t_d = 2.19$. This finding is in excellent accordance with the model described by Graebling, Muller and Palierne (1993), where $t_d = 2.20$.

The emulsion mostly exhibits the characteristic of a viscous fluid for $\omega < \omega_{cp}$. Since the droplet relaxation time in this regime is short relative to the oscillation frequency, it has enough time to adjust to the variations in the shear-rate imposed by the oscillatory flow. At the limit of $\omega \to 0$, the droplet becomes closer to the steady-state situation for a simple shear flow with an equal instant shear-rate. As a result, the droplet response depends mostly on the instantaneous shear-rate at low oscillation frequencies, as evidenced

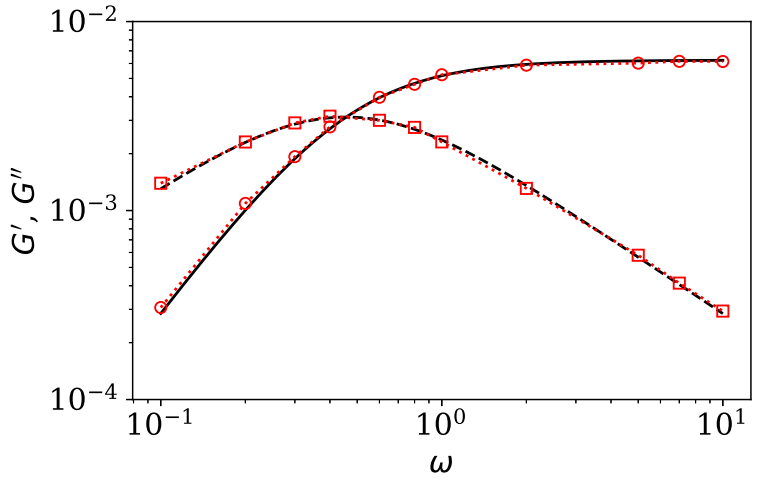

Figure 5.7 – Elastic, G', and Loss, G'', moduli as a function of the non-dimensional angular frequency, ω. Red circles and squares represent, respectively, our results for G' and G''. The solid and dashed black lines refer to the model of Palierne (1990).

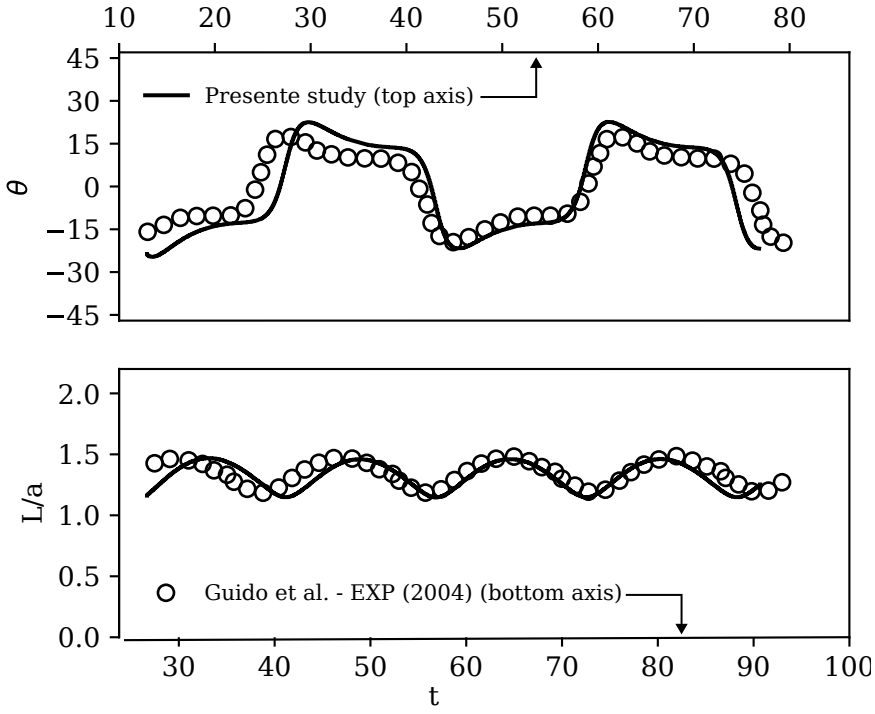

Figure 5.8 – Comparison of the droplet inclination angle and the ratio between the semi-major axis and the initial radius of the drop (L/a) with the experimental study of Guido, Grosso and Maffettone (2004) for $Ca = 0.61$ and $\lambda = 6$. The figure is extracted from the stationary regime of both results, the present study referring to the upper axis and traced in a continuous black line, and the work of Guido, Grosso and Maffettone (2004) referring to the lower axis traced with circular marks.

by $G' \ll G''$. On the other hand, as the relaxation time is greater than the oscillation periods for $\omega > \omega_{cp}$, the droplet response is more sensitive to the instantaneous shear-strain, resulting in $G' \gg G''$. When applied to high-frequency values ($\omega > 2$), G' reaches a plateau region, with values approaching 0.006158.

As a complementary validation of the oscillatory case, Fig. 5.8, presents a comparison between the experimental results of Guido, Grosso and Maffettone (2004) and the simulations of the present study. The first point that is worth mentioning is that both studies reach the stationary regime at different times. The simulation (top axis) reaches a steady state about 15 time units before the experiment (bottom axis). However, after that, there is a complete agreement between both results. It is also worth noting that the scope of this validation comprises a viscosity ratio other than unity, such theory is complemented in Appendix B.

5.3.2 Droplet geometrical properties

In this subsection, we explore how the external magnetic field influences the droplet deformation (D) and inclination angle (θ) when applied in the x, y and z-directions. These geometrical characteristics were measured across a series of cycles for $\omega = 0.10$, 1.00 and 10.00, which stand for low, middle, and high oscillation frequencies, respectively.

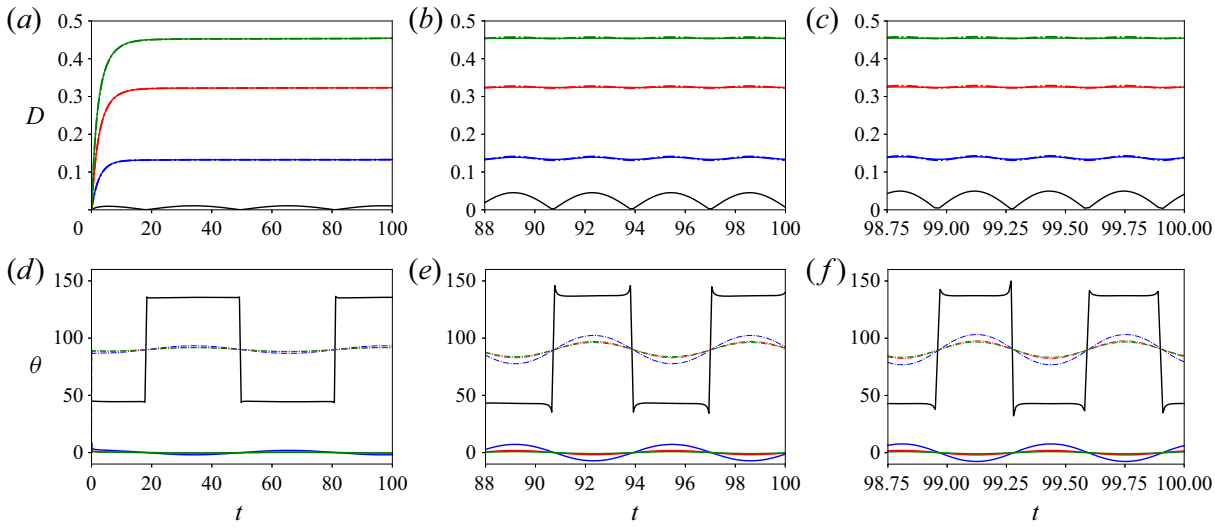

Figure 5.9 – Droplet deformation, D, and inclination angle, θ, over time for the external magnetic field in the x (solid lines) and y-directions (dash-dotted lines) as a function of oscillatory shear frequency and Ca_{mag}. First column for $\omega = 0.10$, the second for $\omega = 1.00$ and the last one for $\omega = 10.00$. Black lines represent the flow in the absence of magnetic field blue lines refer to $Ca_{mag} = 4.00$, red to $Ca_{mag} = 10.00$ and green to $Ca_{mag} = 16.00$.

The deformation and inclination of the droplet over time for various cases with variable magnetic field direction, oscillatory shear frequency, and magnetic capillary number are shown in Figs 5.9 and 5.12. The droplet dynamics in the absence of external magnetic fields is our first point of interest. In figure 5.9(a), the droplet displays a deformation pattern that is based on cyclic oscillations with a single mode, with frequency ω and amplitude ≈ 0.01. Lower oscillation frequencies lead to lower shear-rates since the findings presented

in this study assume a constant oscillation amplitude. The droplet in this instance barely diverges from its spherical form. Recalling that the droplets incline up to 45° relative to the flow direction under low capillary number regimes helps to understand the behavior of the inclination angle in the oscillatory shear. This leads us to the conclusion that θ must be close to either 45° or 135°, depending only on the instant shear-rate direction. This is because the instant ratio between shear stress and surface tension perceived by the droplet is compatible with a small capillary number for low frequencies and small strain amplitudes. Considering this, the droplet inclination oscillates like a binary wave, sharply varying between 45° and 135°, as shown in Fig. 5.9(d).

Figure 5.9(b) shows that the droplet deformation amplitude increases noticeably from $\omega = 0.10$ to $\omega = 1.00$, with the greater oscillation frequency leading to a higher characteristic Ca. In contrast to the previous case, shear stresses for $\omega = 1$ are equivalent to surface tension, allowing deformation peaks of $D \approx 0.05$. Despite the slightly wider fluctuations with $43° \lessapprox \theta \lessapprox 137°$, the binary behavior of θ remained consistent with the earlier case. It is clear that in this situation, regardless of the increased shear-rates imposed by ω, the droplet cannot achieve even higher deformation values due to the short strain available to it. In this respect, compared with the transition from $\omega = 0.10$ to 1.00, we find relatively moderate alterations for D and θ when increasing the frequency from $\omega = 1.00$ to 10.00 (Fig. 5.9(c)). The peaks in D become ≈ 0.5 in this scenario, but the θ fluctuations essentially stay unaltered from the case of $\omega = 1.00$. The surface tension effects caused by the capillary forces eventually become insignificant for high oscillation frequencies in comparison to the high shear-rates, making the droplet deformation solely dependent on the applied strain, with peak deformations being constrained by the strain amplitude.

The effect of an external magnetic field on a ferrofluid droplet subjected to oscillatory shear affects the droplet motion pattern. As can be observed in Figs. 5.9(a), (b) and (c), the deformation behavior for external magnetic fields applied in the x and y-directions is mostly indifferent to the field orientation and the shear frequency. As a result, the magnetic effects predominate in the deformation of the droplet even for the lowest relative magnetic field strength studied, which corresponds to $Ca_{mag} = 4.00$. In this approach, even at large shear-rate frequencies, the droplet deformation exhibits only weak oscillations after the stationary regime is achieved. It's interesting to note that the amplitude of these oscillations is far lower than it would be in the absence of an external field. One can still see that these variations are slightly more pronounced for the field in the $y-$direction. In this situation, the droplet experiences a larger effective shear as the magnetic field extends it to areas of faster flow, with the reverse effect happening for fields applied in the $x-$direction (Cunha et al., 2018; Abicalil et al., 2021). The deformation oscillates around $D = 0.1369 \pm 0.0059$ for $Ca_{mag} = 4.00$, $D = 0.3254 \pm 0.0034$ for $Ca_{mag} = 10.00$ and $D = 0.4553 \pm 0.0027$ for $Ca_{mag} = 16.00$ for $\omega = 10.00$ and a magnetic field in the $y-$direction, indicating a progressive action of the magnetic field in the sense of decreasing the amplitude of D.

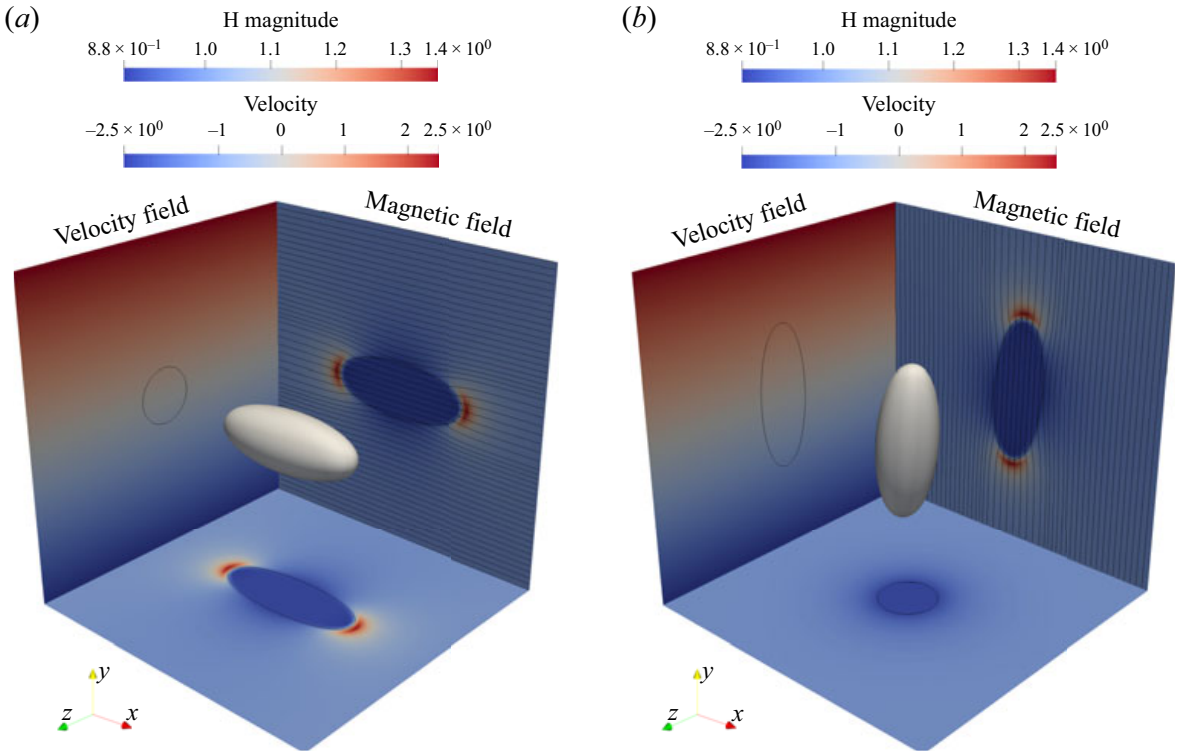

Figure 5.10 – Oscillation amplitude for a droplet under an external magnetic field in the x-direction (a) and y-direction (b) for $Ca_{mag} = 16.00$ and $\omega = 10.00$. The droplet is projected into all orthogonal planes alongside the magnitude of the magnetic field in the xz and xy-planes, with the latter also containing the magnetic field lines. The yz-plane shows the velocity field.

Focusing on the droplet inclination angle, Figs. 5.9(d), (e) and (f) show that the capillary forces are negligible in comparison to the shear and magnetic effects, being bounded by the small strain amplitudes, defined by γ_0 and constant across all cases. The droplet tends to accommodate in the direction of the magnetic field when $\omega = 0.10$, resulting in small oscillations in all cases of Ca_{mag}. The shear stresses are too weak to significantly alter the droplet inclination, similar to the deformation. As a result of the droplet being subjected to higher effective shear-rates in the $y-$direction, the amplitude of the inclination angle oscillations is bigger, though still small, and it gets smaller as Ca_{mag} increases. This amplitude for $Ca_{mag} = 4.00$ is 3.33° for the field in the y-direction and 1.96° for the field in the x-direction. The droplet inclination angle dynamics are quite similar for both $\omega = 1.00$ and 10.00. The droplet mostly maintains the alignment with the field direction and exhibits only minor oscillations for the magnetic field in the x-direction for $Ca_{mag} = 10.00$ and 16.00. In this case, the magnetic effects overcome the shear forces, as illustrated in Fig. 5.10(a). Such oscillations are more noticeable for $Ca_{mag} = 4.00$, with amplitudes of roughly 7.20° for both $\omega = 1.00$ and $\omega = 10.00$.

When the field is in the y-direction, the oscillations are more evident. The curves for $Ca_{mag} = 10.00$ and 16.00 mainly overlay each other, with amplitudes of approximately 6.16° for both $\omega = 1.00$ and $\omega = 10.00$, as illustrated in Fig. 5.10(b). These results indicate

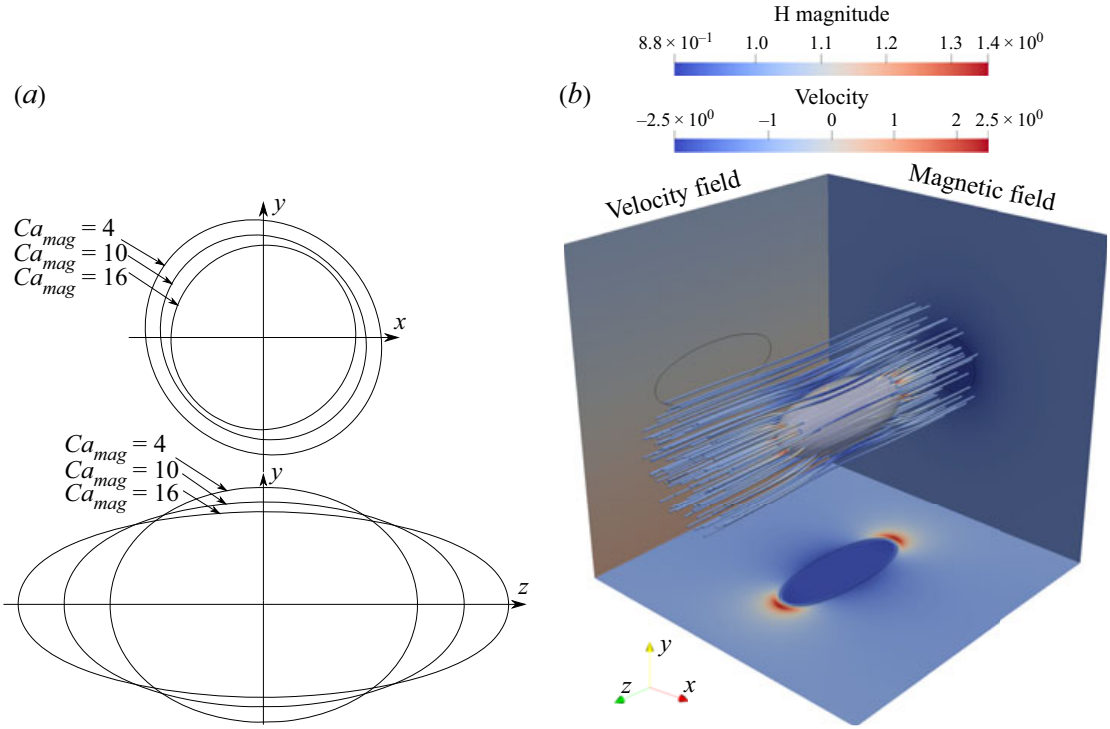

Figure 5.11 – Figure (a) shows the droplet shape for the external magnetic field in z-direction for $t = 91.64$, $\omega = 1.00$ and $Ca_{mag} = 4$, 10 and 16, as indicated by the legend. Figure (b) represents a 3D view of the velocity (yz-plane) and magnetic field projections (xz and xy-planes) together with the magnetic streamlines around the droplet for $Ca_{mag} = 16$ and $\omega = 10$.

that the droplet dynamics were saturated with respect to the shear frequency. We verify an oscillation amplitude of 12.35° for both $\omega = 1.00$ and $\omega = 10.00$ for $Ca_{mag} = 4.00$. When analyzing the rheology of the current system in the next subsections, such comprehension will be crucial.

Since the elongation of the droplet happens perpendicular to the shear plane, applying magnetic fields in the z-direction has various effects. Figure 5.11(a) displays the droplet shape from two angles for various values of Ca_{mag}. The principal effect is that the droplet cross-section stays almost circular in the xy-plane. Additionally, due to the droplet elongation in the direction of the magnetic field, when Ca_{mag} increases, this cross-sectional area reduces with the conservation of the droplet mass.

The droplet inclination angle in Figs. 5.12(d), (e) and (f) is the first crucial aspect to be examined. Regardless of Ca_{mag} and ω, the droplet oscillates in a binary form since its near-circular cross-section in the shear plane is comparable to what it would be in the absence of a magnetic field. Small spikes that result from the change in angle may be seen; these spikes are also present in the no-field scenario. These are outliers because of the difficulty of calculating the inclination angles as the cross-sections get smaller and more circular (when the flow direction is reversing). For $Ca_{mag} = 16$, such spikes are therefore more pronounced.

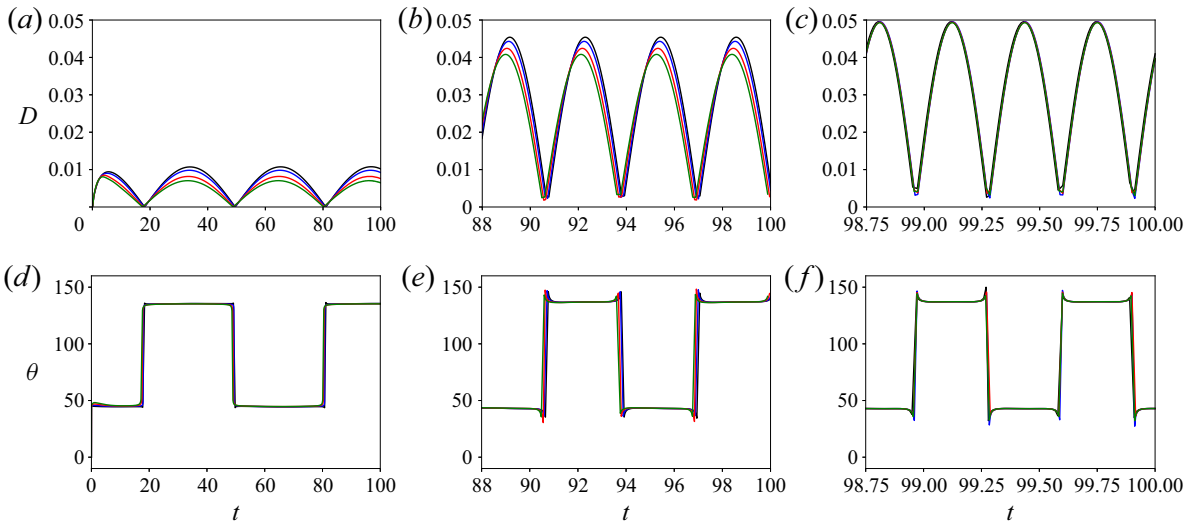

Figure 5.12 – Droplet deformation, D, and inclination angle, θ, over time for the external magnetic field in the z-direction as a function of oscillatory shear frequency and Ca_{mag}. First column for $\omega = 0.10$, second for $\omega = 1.00$, and the last one for $\omega = 10.00$. Black lines represent the flow in the absence of a magnetic field, blue lines refer to $Ca_{mag} = 4.00$, red to $Ca_{mag} = 10.00$, and green to $Ca_{mag} = 16.00$.

Smaller values of Ca_{mag} result in larger deformation amplitudes for $\omega = 0.10$, as shown in Fig. 5.12(a), with peaks of $D \approx 0.011$ for $Ca_{mag} = 0$ (no magnetic field) and $D \approx 0.0081$ for $Ca_{mag} = 16$. Figure 5.12(b) shows a comparable dynamic for $\omega = 1.00$, but having noticeably larger deformation amplitudes, such as $D \approx 0.048$ for $Ca_{mag} = 0$ and $D \approx 0.043$ for $Ca_{mag} = 16$. Figure 5.12(c) shows how the curves collapse at $\omega = 10$, becoming identical despite the various values of Ca_{mag}, with a deformation amplitude of $D \approx 0.051$. Figure 5.11(b) shows this phenomena for $Ca_{mag} = 16$ and $\omega = 10$. In order to look for a potential trend reversal, we also extended this investigation to $\omega = 12$, however, we discovered that doing so merely strengthens the convergence of the curves. This finding implies that magnetic influence has little effect on droplet deformation at high oscillation frequencies. It should be noted that only the deformation of the droplet in the shear plane is covered in this analysis. The overall droplet shape is still influenced by the magnetic field intensity. Larger values of Ca_{mag} result in larger droplet elongations in the field direction. It is interesting to observe in Fig. 5.12(b) that both curves move to the left when Ca_{mag} increases. This dynamic may be caused by the droplet tendency to shrink in the shear plane as Ca_{mag} increases, which also results in a reduction in effective Ca and relaxation times.

5.3.3 Viscoelastic properties

In this section, we investigate the influence of both the external magnetic fields, defined by the magnetic capillary number Ca_{mag} and the field direction, and the angular frequency ω on the emulsion linear viscoelastic properties. As a consequence of the

geometric dynamics reported in Sec. 5.3.2, the droplet experiences changes in its storage and loss moduli. In this section, such analyses are based on both symmetric, $Sym(\mathbf{\Sigma}^D)$, and antisymmetric, $Asym(\mathbf{\Sigma}^D)$, parts of the particle stress tensor.

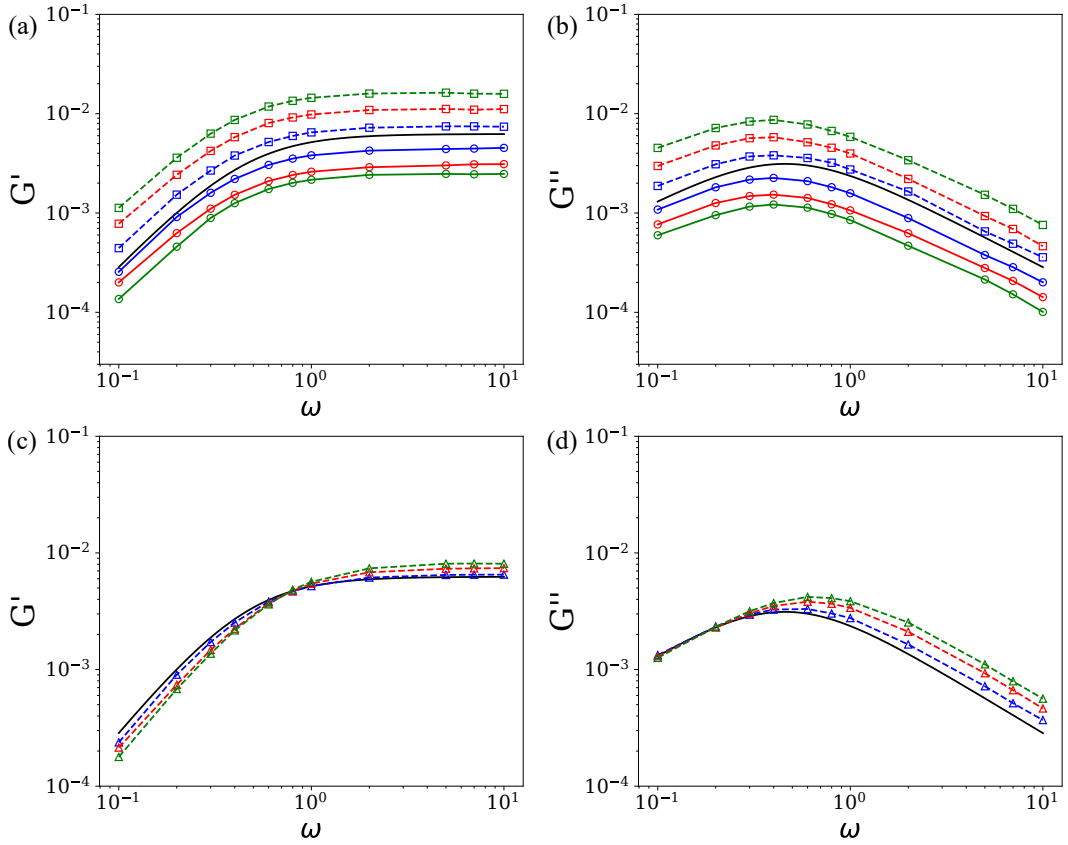

Figure 5.13 – Linear viscoelastic properties, G', and G'', based on the yx component of $Sym(\mathbf{\Sigma}^D)$, for an external magnetic field in x, y, and z directions. The first column is for G' and the second one is for G''. The first row represents the results for x-direction (circle marks) and y-direction (squared marks). The second row shows the results for z-direction (triangle marks). Black solid lines are for $Ca_{mag} = 0$ (Palierne, 1990), blue lines are for $Ca_{mag} = 4$, red ones for $Ca_{mag} = 10$ and green ones for $Ca_{mag} = 16$

The magnetic field in the x-direction reduces the oscillatory dynamics of the droplet as well as the actual shear effects. The main effect is when Ca_{mag} grows, where the amplitude of the particle shear stress, Σ^D_{yx}, gradually decreases. Figures 5.13(a) and (b) show this behavior through the in-phase (G') and out-of-phase (G'') components extracted from $Sym(\mathbf{\Sigma}^D)$. As can be seen, the overall behavior as a function of angular frequency stays mostly constant and is comparable to the situation in the absence of magnetic fields despite the vertical displacements of the curves. In the case of $\omega \to 0.1$, the long oscillation periods provide capillary effects enough time to strongly influence the droplet shape. As a consequence, the droplet deformation is mostly governed by the instant shear-rate, resulting in $G' \ll G''$ and a predominantly viscous behavior. Regardless of the magnetic capillary number, the moment at which G' becomes higher than G'' occurs at $\omega_{cp} \approx 0.41$. As the oscillation frequency rises, there is a progressive change from this viscous to elastic behavior. The capillary effects on the droplet shape become unimportant at high

oscillation frequencies. The instantaneous shear-strain controls the droplet deformation since the time needed for capillary effects to impact the droplet shape is significantly longer than the oscillation periods. As a result of the $G' \gg G''$, the emulsion exhibits a mainly elastic characteristic.

An opposite effect is seen in relation to Ca_{mag} for external magnetic fields oriented in the y-direction. The droplet becomes more elongated in the direction of the velocity gradient as the magnetic capillary number increases, which exposes it to more effective shear and leads to higher variations in θ. Figures 5.13(a) and (b) show that when Ca_{mag} grows, both the in-phase and out-of-phase components increase, in contrast to the situation of magnetic fields in the x-direction. The droplet response is mostly determined by the instantaneous shear-rate at low oscillation frequencies and by the shear-strain at high frequencies, much like in the case of magnetic fields in the x-direction. Similar to what was discovered for magnetic fields in the x-direction, the transition point at which G' becomes greater than G'' stays constant across the Ca_{mag} range despite the rise in viscoelastic components. We think that the magnetic field does not affect the droplet effective relaxation time in either direction given that the percentage difference between the droplet relaxation time for the cases with and without the magnetic field is less than 9%.

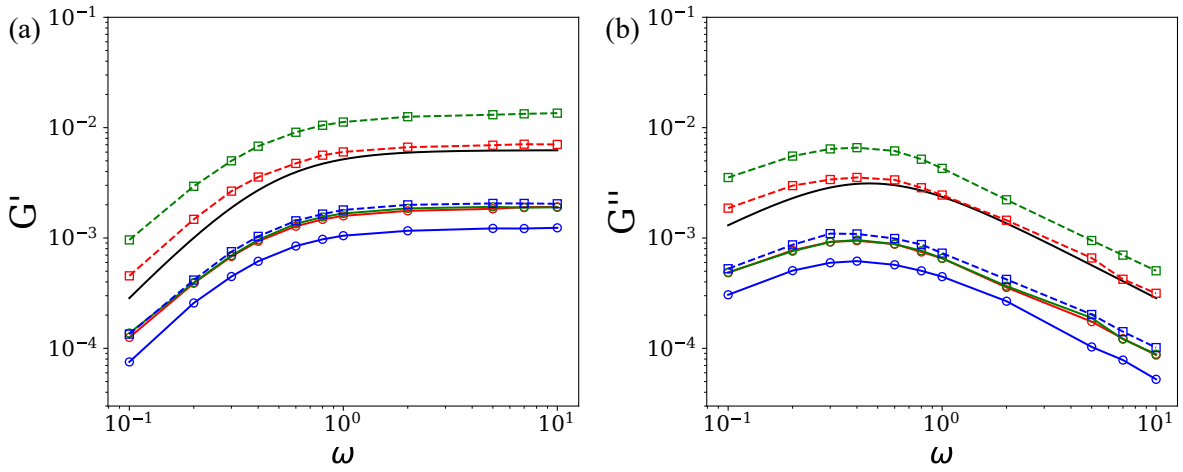

Figure 5.14 – Linear viscoelastic properties, G', and G'', based on the yx component of $Asym(\mathbf{\Sigma}^D)$, for an external magnetic field in x and y-directions. Circle marks represents the results for x-direction and the squared marks ones for y-direction. Black solid lines are for $Ca_{mag} = 0$ (Palierne, 1990), blue lines are for $Ca_{mag} = 4$, red ones for $Ca_{mag} = 10$ and green ones for $Ca_{mag} = 16$

For all cases presented in this section, the external magnetic field creates significant changes in the behavior of the components of the particle stress tensor. The magnetic field in the x-direction causes $|\Sigma^D_{yx}| < |\Sigma^D_{xy}|$, while in the y-direction, $|\Sigma^D_{yx}| > |\Sigma^D_{xy}|$. In the case of the symmetrical part of the particle stress, there is no phase shift since the yx component of the $Sym(\mathbf{\Sigma}^D)$ is given by $(\Sigma^D_{yx} + \Sigma^D_{xy})/2$. For $Asym(\mathbf{\Sigma}^D)$, the same component in the x-direction produces a π rad phase shift in relation to the y-direction once the yx component is given by $(\Sigma^D_{yx} - \Sigma^D_{xy})/2$, similar to that presented for the magnetic torque in Sec. 5.3.5.3. Figure 5.14 shows a behavior similar to the presented in Fig. 5.13

The relaxation times remain unchanged with the same behavior as a function of ω and Ca_{mag}.

When the magnetic field is oriented in the z-direction, a distinct phenomenon takes place, the first point is that $Sym(\mathbf{\Sigma}^D)$ is already symmetric, *i.e.*, $Sym(\mathbf{\Sigma}^D) = \mathbf{\Sigma}^D$. Figures 5.13(c) and (d) show that the behavior is mixed, with different responses to changes in Ca_{mag} depending on the oscillation frequency. Changes in G'' are almost unnoticeable at low angular frequencies, with ω around 0.1, and both G' and G'' decrease with rising Ca_{mag}, but in a considerably less pronounced manner than what was found for the other two directions. This behavior is similar to that in simple shear flows that have already been described in the literature (Ishida; Matsunaga, 2020; Abicalil et al., 2021). In contrast, when Ca_{mag} increases, both G' and G'' rise at high oscillation frequencies ($\omega \to 10$).

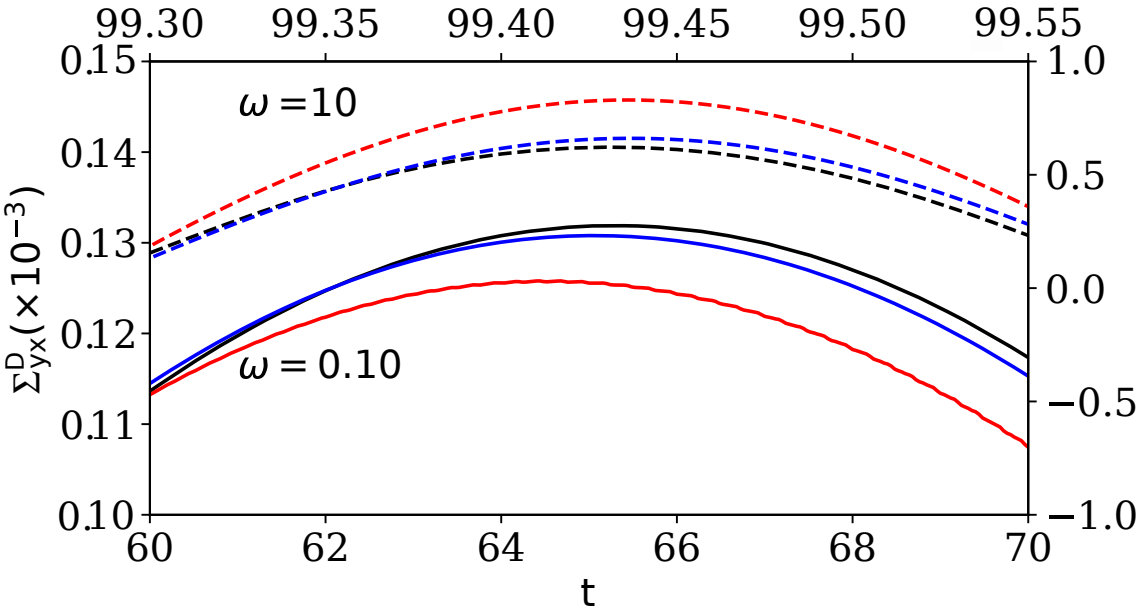

Figure 5.15 – yx component of the particle stress given by Eq. 3.27 for $\omega = 10.00$ (dashed lines), relative to the top and right axes, and $\omega = 0.10$ (solid lines), relative to the bottom and left axes. Black, blue, and red colors correspond to $Ca_{mag} = 0,\ 4$ and 16, respectively.

Figure 5.15 shows the same phenomenon by using the particle shear stress component Σ^D_{yx} for $\omega = 0.1$ (solid lines) and $\omega = 10$ (dashed lines). When $\omega = 0.1$, an increase in Ca_{mag} is followed by lower amplitudes in the signal of Σ^D_{yx}, however, when $\omega = 10$, the opposite is observed. This leads to the conclusion that the reduction in the viscoelastic properties is related to the reduction in the amplitude of Σ^D_{yx} caused by the larger magnetic capillary numbers at low oscillation frequencies, as shown in Figs. 5.13(c) and (d). In contrast, the rise in the amplitude of Σ^D_{yx} with higher Ca_{mag} at high oscillation frequencies causes a stronger interference of the droplet in the flow, leading to the higher viscoelastic moduli.

It is remarkable to notice that the existence of magnetic fields in the z-direction does affect the droplet effective relaxation time, in contrast to what was shown for magnetic

fields in the x and y-directions. The droplet effective relaxation time was calculated to be $t \approx 2.20,\ 1.90,\ 1.62$ and 1.45, for $Ca_{mag} = 0,\ 4\ ,10$ and 16, respectively, based on the crossover points at which G' becomes bigger than G''. This is a result of the droplet cross-sectional area decreasing, as was discussed in Sec. 5.3.2 and the previous paragraphs.

The variations in the viscoelastic moduli are caused by adjustments in the balancing act between various effects. The droplet cross-sectional area decreases as it is stretched in the z-direction, putting it under less effective shear and having less of an impact on the flow at the central shear plane. However, the droplet frontal area in relation to the flow direction increases due to the rise in length in the z-direction, which leads the droplet to contact with a higher proportion of shear planes. According to the discussion in Sec. 5.3.2, at low oscillation frequencies, there is also a corresponding decrease in the deformation of the droplet as Ca_{mag} increases. Similar to what is seen for simple shear flow (Abicalil et al., 2021), in this situation the balance of these three effects causes the viscoelastic moduli to decrease as Ca_{mag} increases. For high oscillation frequencies, however, the droplet deformation becomes indifferent to changes in the magnetic capillary number, a fact that tips the balancing act between the three aforementioned effects in the opposite direction, resulting in the observed increases in both viscoelastic moduli with an increasing magnetic capillary number.

5.3.4 Normal stress difference

The magnetic field generates larger stresses at the droplet tips than in the flattened areas, as implicitly seen in Sections 5.3.2 and 5.3.3. In accordance with this, we now go on to the analysis of the droplet anisotropy using the first and second normal stress differences, denoted, respectively, as $N_1 = \Sigma^D_{xx} - \Sigma^D_{yy}$ and $N_2 = \Sigma^D_{yy} - \Sigma^D_{zz}$.

It is possible to see the impact of the magnetic field on the normal stress differences by analyzing Eq. 3.27. Surface tension works in order to restore the spherical droplet shape as the magnetic field stretches the droplet in its respective direction. In addition, the term H^2 is maximized when the surface's normal vector coincides with the direction of the magnetic field, which dominates the effects of the surface tension under these circumstances, and N_1 (or N_2) may shift signs.

N_1 and N_2 are shown in Fig. 5.16 as a function of time for $\omega = 1.00$. Results for $\omega = 0.10$ and 10.00 are not included since they are similar to those of the presented case. Figure 5.16(a) shows that the magnetic field in the x-direction induces $\Sigma^D_{xx} < \Sigma^D_{yy}$, an effect that becomes stronger as Ca_{mag} increases, demonstrating the magnetic field's capacity to establish a preferred orientation and promote anisotropy. Since the droplet barely deviates from the magnetic field direction, as illustrated in Sec. 5.3.2, the oscillations in N_1 decrease as Ca_{mag} increases. N_2 is independent of magnetic field strength since there is no impact on Σ^D_{yy} and Σ^D_{zz} components.

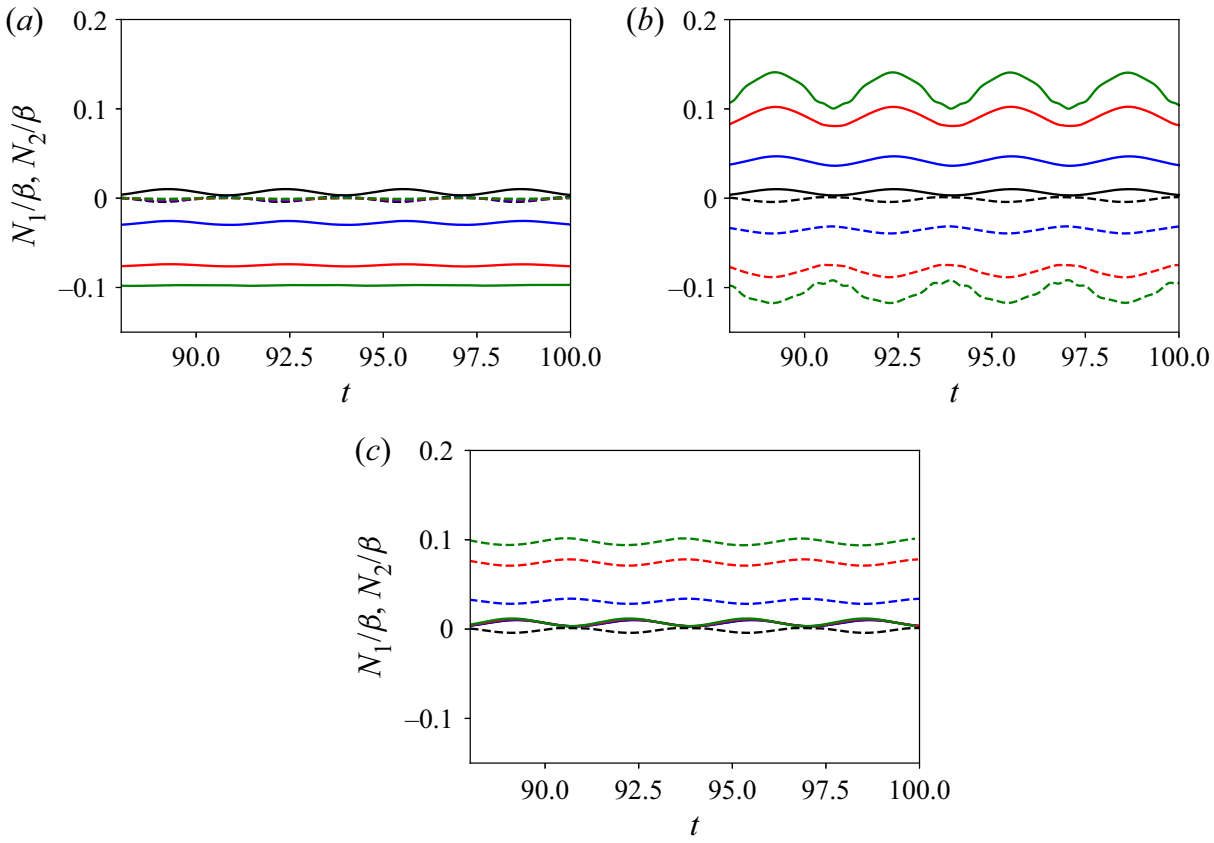

Figure 5.16 – First (solid lines) and second (dashed lines) normal stress differences, scaled by the volume fraction, for an external magnetic field in the x (a), y (b) and z (c) directions and $\omega = 1.00$. Black, blue, red and green colors are, respectively, for $Ca_{mag} = 0,\ 4,\ 10$ and 16.

The symmetrical behavior between N_1 and N_2 in Fig. 5.16(b) shows that both Σ^D_{xx} and Σ^D_{zz} were not significantly impacted by the magnetic field in the y-direction, *i.e.*, the magnetic field only generated anisotropy in its respective direction. The existence of the droplet in an area of increased effective shear, as a function of Ca_{mag}, counterbalances the magnetic field effect, as shown in Secs. 5.3.2 and 5.3.3. As a result, when the droplet is primarily aligned with the magnetic field, N_1 peaks coincide with the lowest points of D, and the valleys correspond with the places of greatest deformation, where the droplet is least aligned with the magnetic field.

Figure 5.16(c) shows the third scenario with external magnetic fields pointing in the z-direction. Since the anisotropies caused by the magnetic field have a little direct impact on Σ^D_{xx} and Σ^D_{yy}, N_1 is unaffected in this scenario. Although values of N_1 for magnetic fields in the x-direction are mostly opposite and equal in magnitude to N_2 for the present case, the magnetic field in the z-direction does not restrict the droplet orientation in the shear plane. Thus, when the shear flow oscillates, the droplet inclination angle varies as well, causing variations in Σ^D_{yy} and, in turn, the oscillations seen in N_2.

These findings suggest that external magnetic fields, as in the simple shear flow in

two (Cunha et al., 2018; Cunha et al., 2020b) and three dimensions (Ishida; Matsunaga, 2020; Abicalil et al., 2021), are capable of creating large anisotropies in emulsions subjected to SAOS flows. In conclusion, magnetic fields in the x-direction led to large negative values of N_1 with no appreciable changes in N_2. Magnetic fields in the y-direction led to large positive values of N_1 and large negative values of N_2. Lastly, magnetic fields in the z-direction led to large positive values of N_2 with no significant changes in N_1.

5.3.5 Magnetization of dilute emulsions

In this section, we examine the emulsion magnetization under the combined influence of an external magnetic field and a small amplitude oscillatory shear flow. Despite the superparamagnetic behavior of the droplet, as stated by Abicalil et al. (2021) for the case of simple shear flows, there is a misalignment angle, θ_{mag}, between the bulk magnetization, $\langle \mathbf{M} \rangle$, and the external field, $\mathbf{H}_0$, which causes a magnetic torque, $\boldsymbol{\tau}_{mag}$.

5.3.5.1 Magnetization

In order to calculate the non-dimensional bulk magnetization, in accordance with Abicalil et al. (2021) and Cunha et al. (2020b), we have

$$\langle \mathbf{M} \rangle = \frac{1}{V} \int_V (\zeta_\epsilon(\phi) - 1)\mathbf{H} dV \,, \tag{5.3}$$

where the magnetization effects are restricted to the droplet, since $\zeta_\epsilon(\phi) = 1$ in the continuous phase.

As can be shown in Sec. 5.3.2 the droplet stays elongated with D nearly constant when the magnetic field is in the x-direction. The vector $\langle \mathbf{M} \rangle$ has three components, but only M_y exhibits a periodic oscillation over time. Similar to this, only the x-component of the $\langle \mathbf{M} \rangle$ oscillates for magnetic fields directed in the y-direction. The magnetization does not fluctuate in the presence of external magnetic fields in the z-direction.

The y and x components of the bulk magnetization for magnetic fields in the x and y-direction, respectively, are shown in Fig. 5.17 for $\omega = 1.00$. According to Sec. 5.3.2, for external magnetic fields in the x-direction, the droplet is constrained in an area of lower effective shear and maintains a roughly aligned position with the magnetic field. Even if the average values of $\langle \mathbf{M} \rangle$ grow, the amplitude of M_y decreases due to the amplitude of θ, reducing as Ca_{mag} increases. Specifically, the average values of $\langle \mathbf{M} \rangle / \beta = 0.8,\ 0.86$ and 0.89, but the peak values of M_y/β are $0.006,\ 0.004$, and 0.003 for $Ca_{mag} = 4,\ 10$, and 16, respectively. As a result, M_y has no impact on the signal of $\langle \mathbf{M} \rangle$, which essentially stays in a straight line. In the case of external magnetic fields in the y-direction, the average values of $|\langle \mathbf{M} \rangle| / \beta$ increase in a similar way and approximately with the same values as for the case of magnetic fields in the x-direction. The magnetization amplitude,

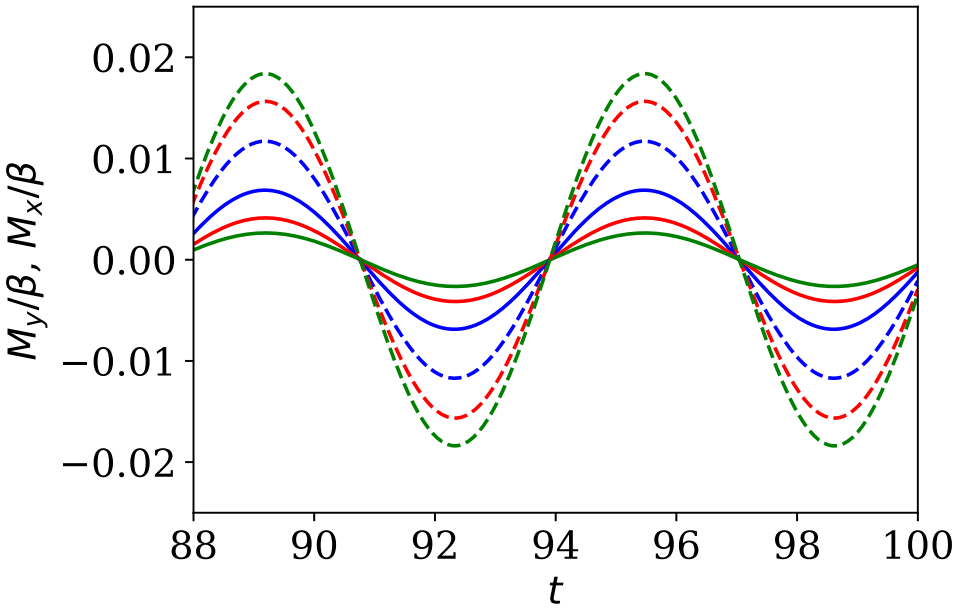

Figure 5.17 – Bulk magnetization scaled by the volume fraction for $\omega = 1.00$ and $Ca_{mag} = 4$ (blue lines), $Ca_{mag} = 10$ (red lines) and $Ca_{mag} = 16$ (green lines). Solid lines correspond to M_y for external magnetic fields in the x-direction, and dashed lines correspond to M_x for magnetic fields in the y-direction.

however, rises with increasing Ca_{mag}, with a maxima of $M_x/\beta = 0.012,\ 0.016$ and 0.018 for $Ca_{mag} = 4,\ 10$ and 16 respectively. As a result, the increase in the droplet deformation associated with higher values of Ca_{mag} leads to increases in the amplitude of M_x. In this case, even though the amplitude of the droplet inclination angle also decreases with increasing Ca_{mag}, this reduction is far less significant than for the case of external magnetic fields in the x-direction. In a similar manner, the signal of $\langle \mathbf{M} \rangle$, which is roughly constant, is not much affected by M_x.

The magnetization signal can be analyzed following a similar methodology to that employed in Sec. 5.3.3 for the particle shear stress. In this way, we have that

$$M_k = \chi'_k \sin \omega t + \chi''_k \cos \omega t, \tag{5.4}$$

where k designates the magnetization component. χ'_k is the component in-phase with the shear-strain and χ''_k the component 90° out-of-phase, *i.e.*, in-phase with the shear-rate.

Based on the Eq. 5.4, Figs. 5.18 and 5.19 show both the in-phase and out-of-phase components. The connection with the viscoelastic qualities in Sec. 5.3.3 is the first topic to be explored. In this sense, there were no appreciable variations in M_k for $\omega \gtrapprox 1$, indicating a plateau in saturation as a function of Ca_{mag}. Additionally, we discovered a non-zero χ'', demonstrating the existence of an out-of-phase component in the periodic response of the $\langle \mathbf{M} \rangle$ with respect to the applied periodic shear. Consequently, as a result of the emulsions mechanical response to the periodic shear, the magnetization shows a finite relaxation time. The frequency in which χ' and χ'' are equal is $\omega = 0.41$, which is precisely the same frequency in which $G' = G''$. That is a piece of strong evidence that the periodic variations in the droplet shape and orientation at the micro-scale are the origin of the magnetization

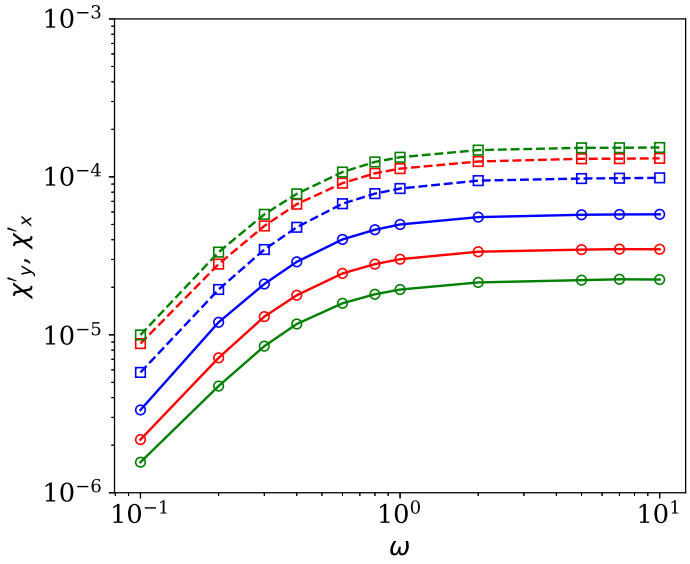

Figure 5.18 – In-phase component of the bulk magnetization, χ', as a function of angular frequency for $Ca_{mag} = 4$ (blue lines), $Ca_{mag} = 10$ (red lines) and $Ca_{mag} = 16$ (green lines). Solid lines represent χ'_y for the magnetic field in the x-direction and dashed lines χ'_x for the magnetic field in the y-direction.

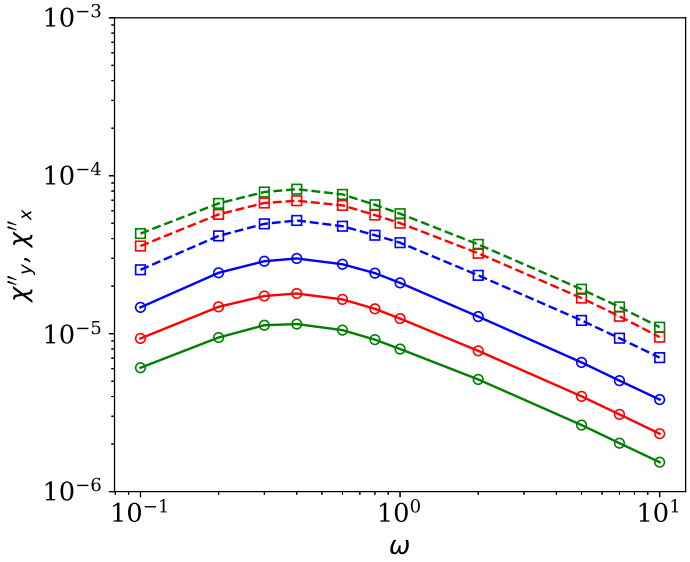

Figure 5.19 – Out-of-phase component of the bulk magnetization, χ'', as a function of angular frequency for $Ca_{mag} = 4$ (blue lines), $Ca_{mag} = 10$ (red lines) and $Ca_{mag} = 16$ (green lines). Solid lines represent χ''_y for the magnetic field in the x-direction and dashed lines χ''_x for the magnetic field in the y-direction.

relaxation process in diluted magnetic emulsions (the same mechanism originating the mechanical viscoelastic response). In this sense, the effective magnetic susceptibility, based on the periodic components and given by given by $\chi = \sqrt{\chi'^2 + \chi''^2}$, is larger for high oscillation frequencies (with the emulsion exhibiting a solid-like behavior) than for lower oscillation (with the emulsion displaying a liquid-like behavior) frequencies.

It is important to note that regular ferrofluids are expected to approach nonlinear regimes of magnetization for some of the high values of Ca_{mag} ($\gtrapprox 10$) investigated in this

study. In experiments with currently workable ferrofluids, one would need to drastically reduce the interfacial tension to something in the order of 10^{-3} N/m by the use of surfactants and arrange emulsion samples with millimeter-sized droplets in order to achieve such high Ca_{mag} values and still maintain the linear regime.

5.3.5.2 Angle between $\langle \mathbf{M} \rangle$ and $\mathbf{H}_0$

Even for a superparamagnetic droplet, $\mathbf{M}$ and $\mathbf{H}_0$ are not aligned due to the combined effects of the shear flow and the external magnetic field. The deformation of the droplet, the strength and the direction of the external magnetic all influence the angle, or θ_{mag}, between $\mathbf{M}$ and $\mathbf{H}_0$.

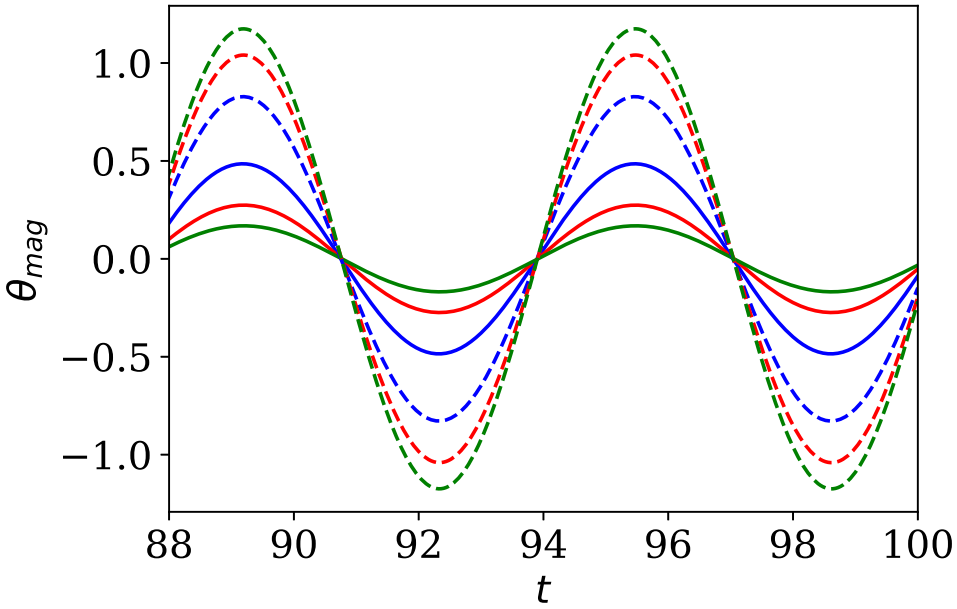

Figure 5.20 – Angle between $\langle M \rangle$ and H_0, θ_{mag}, in degrees, for an external magnetic field in the x (solid lines) and y-directions (dashed lines), for $Ca_{mag} = 4$ (blue lines), $Ca_{mag} = 10$ (red lines) and $Ca_{mag} = 16$ (green lines).

Fig. 5.20 shows θ_{mag} for $\omega = 1.00$. In this case, the previously examined magnetization components and θ_{mag} are directly related. It is possible to represent this parameter using both M_x and M_y, *i.e.*, $\theta_{mag} = \sin^{-1}\left(M_y/|\langle \mathbf{M} \rangle|\right)$ and $\theta_{mag} = \sin^{-1}\left(M_x/|\langle \mathbf{M} \rangle|\right)$ for magnetic fields in the x and y-directions. Thus, as the droplet, and consequently the magnetization vector, are constrained by the magnetic field in the x-direction, θ_{mag} oscillations become smaller with increasing Ca_{mag}, with amplitudes of θ_{mag} approximately 0.48, 0.28 and 0.17 for $Ca_{mag} = 4$, 10, and 16, respectively. In contrast, the amplitudes tend to grow with Ca_{mag} when the magnetic field is directed in the y-direction. This is because the droplet encounters larger effective shear-rates and comparatively smaller decreases in inclination angle oscillations.

The angle θ_{mag} can also be analyzed similarly to the stress and susceptibility, using

the equation

$$\theta_{mag} = \theta'_{mag} \sin \omega t + \theta''_{mag} \cos \omega t \,, \tag{5.5}$$

to decompose θ_{mag} into components in-phase (θ'_{mag}) and out-of-phase (θ''_{mag}) with the shear-rate.

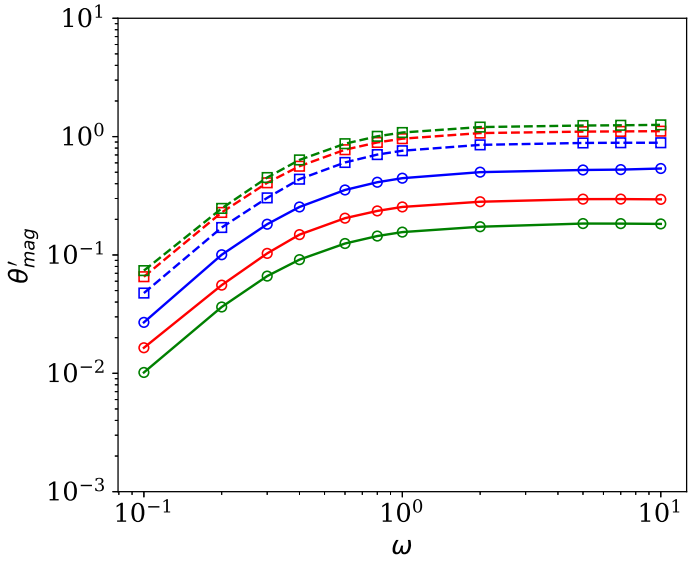

Figure 5.21 – In-phase component of θ_{mag}, θ', as a function of angular frequency for $Ca_{mag} = 4$ (blue lines), $Ca_{mag} = 10$ (red lines) and $Ca_{mag} = 16$ (green lines). Solid lines correspond to magnetic fields in the x-direction, and dashed lines correspond to magnetic fields in the y-direction.

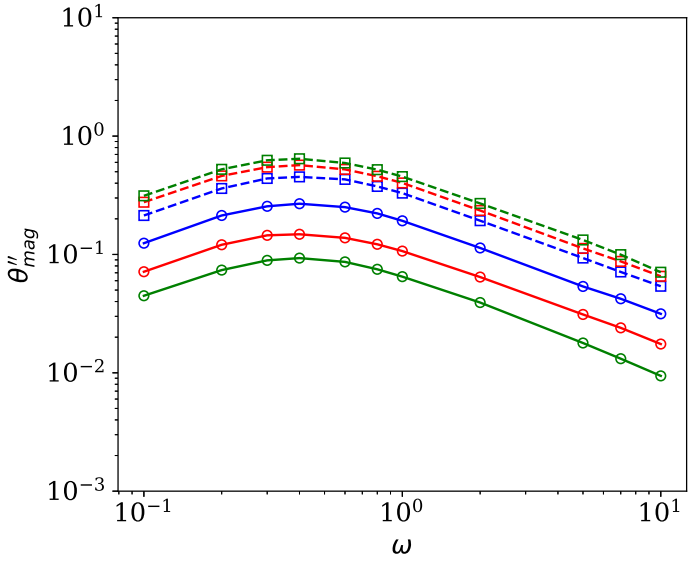

Figure 5.22 – Out-of-phase component of θ_{mag}, θ'', as a function of angular frequency for $Ca_{mag} = 4$ (blue lines), $Ca_{mag} = 10$ (red lines) and $Ca_{mag} = 16$ (green lines). Solid lines correspond to magnetic fields in the x-direction, and dashed lines correspond to magnetic fields in the y-direction.

The findings are the same as those of the magnetization, including the crossover point, as can be seen in Figs. 5.21 and 5.22, since θ_{mag} is computed as a function of the magnetization components. Although the equation of θ_{mag} represents a non-linear

relationship to $\langle \mathbf{M} \rangle$, we can rewrite it as $\theta_{mag} = M_y/|\langle \mathbf{M} \rangle|$ and $\theta_{mag} = M_x/|\langle \mathbf{M} \rangle|$ for small arguments.

5.3.5.3 Magnetic torque

Due to the misalignment of $\mathbf{M}$ and $\mathbf{H}_0$, a magnetic torque arises in the fluid. The conservation of angular momentum is ensured by an opposing hydrodynamic torque that balances out this magnetic force (Cunha et al., 2020b; Abicalil et al., 2021). Equation 3.27 describes how this produced hydrodynamic torque appears as asymmetries in the particle stress tensor. In our study, we compute the non-dimensional magnetic torque, $\boldsymbol{\tau}_{mag}$, normalized by σ/a, using the following expression (Rosensweig, 2013; Cunha et al., 2020b; Abicalil et al., 2021)

$$\boldsymbol{\tau}_{mag} = Ca_{mag} \langle \mathbf{M} \rangle \times \mathbf{H}_0 \,, \tag{5.6}$$

highlighting that $\boldsymbol{\tau}_{mag}$ is proportional to both $|\langle \mathbf{M} \rangle|$ and $\sin \theta_{mag}$ (Abicalil et al., 2021).

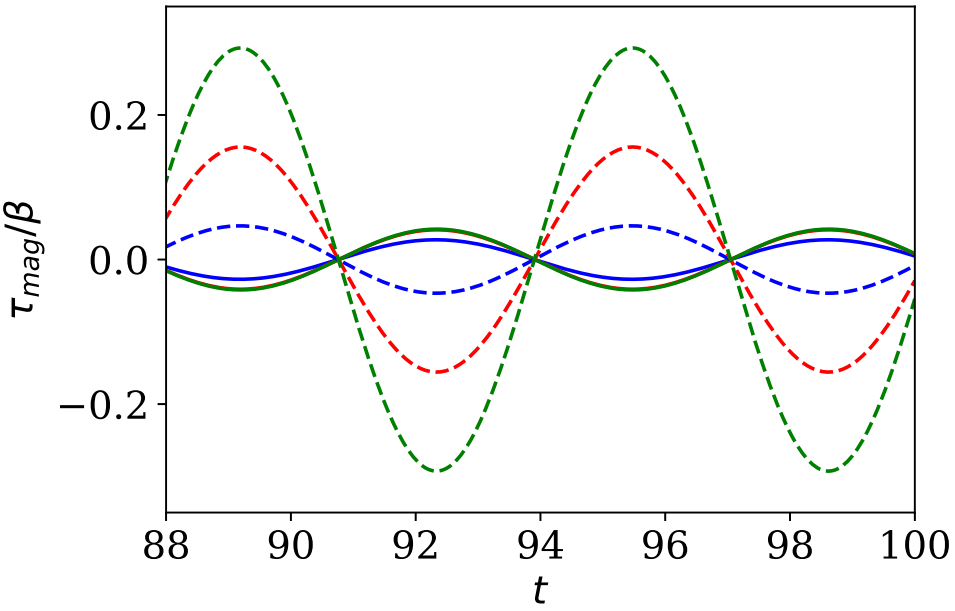

Figure 5.23 – Torque scaled by σ/a for external magnetic fields in x (solid lines) and y-directions (dashed lines), with $Ca_{mag} = 4$ (blue lines), $Ca_{mag} = 10$ (red lines) and $Ca_{mag} = 16$ (green lines).

Figure 5.23 presents the magnetic torque scaled by β over time for the magnetic field in x (solid lines) and y-directions (dashed lines). It can be seen that the peaks of magnetic torque for magnetic fields in the x-direction correspond to the valleys for fields in the y-direction, *i.e.*, they act in opposite directions. As shown in figures 5.9 and 5.10, during the first half of its oscillation cycle, the droplet always assumes inclination angles in the range $0° < \theta < 90°$, regardless of magnetic field direction. Since the magnetic torque acts in the direction of aligning the droplet to the magnetic field, this results in a clockwise

torque for magnetic fields in the x-direction, and counter-clockwise torques for magnetic fields in the y-direction.

The magnetic torque magnitude, τ_{mag}, scaled by β, over time for the magnetic field in the x (solid lines) and y-directions (dashed lines) is shown in Fig. 5.23. As can be observed, the magnetic torque peaks for fields acting in the x-direction correspond to the valleys for fields in the y-direction, *i.e.*, they act in opposite directions. The droplet always takes inclination angles in the range $0° < \theta < 90°$ throughout the first half of its oscillation cycle, independent of the direction of the magnetic field, as seen in figures 5.9 and 5.10. A clockwise torque is produced for magnetic fields in the x-direction and a counterclockwise torque is produced for magnetic fields in the y-direction since the magnetic torque operates in the direction of aligning the droplet to the magnetic field. For the second half of the oscillation cycle, both torques act in opposite directions.

For magnetic fields in the x-direction, raising Ca_{mag} from 4 to 10 leads to an increase in torque amplitude, with the magnetization magnitude outweighing the decrease in the angle between $\langle \mathbf{M} \rangle$ and $\mathbf{H}_0$. This is readily seen in Fig. 5.23. However, due to the reduction in θ_{mag} and increase in magnetization, an additional increase in Ca_{mag} to 16 does not appreciably alter the torque amplitude. In the y-direction, increases in Ca_{mag} cause increases in magnetization and θ_{mag}, which in turn increases torque amplitude for external magnetic fields.

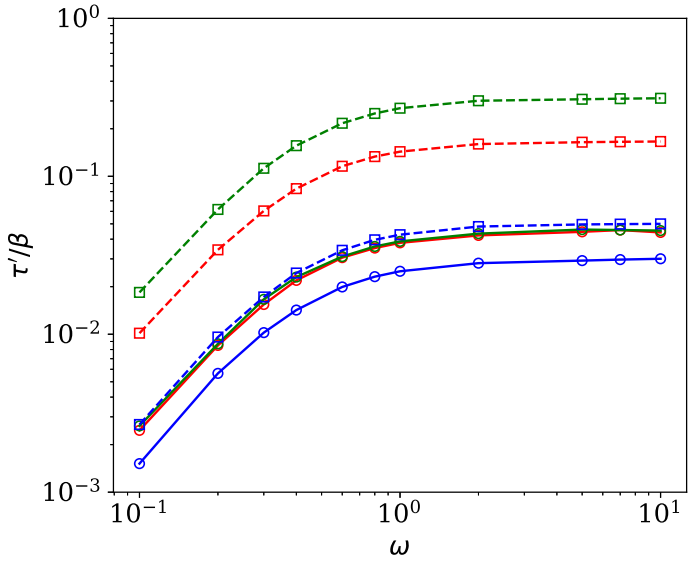

Figure 5.24 – In-phase, τ', component of the torque scale by $\sigma\beta/a$ as a function of angular frequency for $Ca_{mag} = 4$ (blue lines), $Ca_{mag} = 10$ (red lines) and $Ca_{mag} = 16$ (green lines). Solid lines are for the magnetic field in the x-direction and dashed lines are for the magnetic field in the y-direction.

Focusing on the signal of the non-dimensional magnetic torque, it can be decomposed using the definition

$$\frac{\tau_{mag}}{\beta} = \alpha \left[\frac{\tau'}{\beta} \sin \omega t + \frac{\tau''}{\beta} \cos \omega t \right] , \tag{5.7}$$

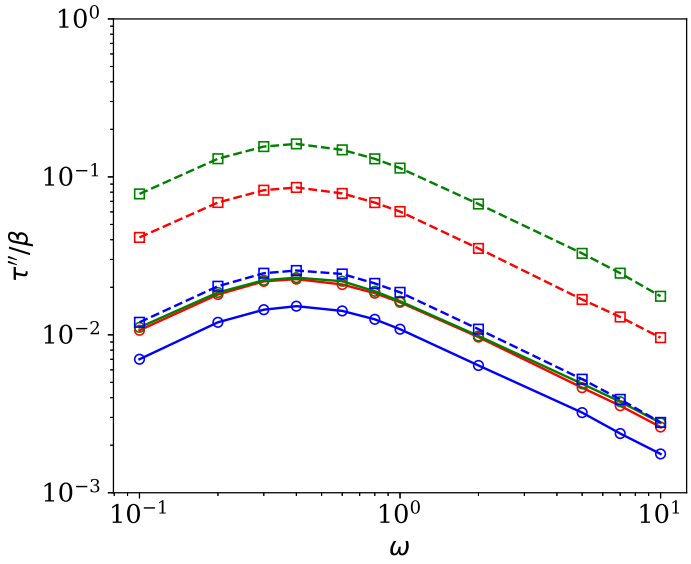

Figure 5.25 – Out-of-phase, τ'', component of the torque scale by $\sigma\beta/a$ as a function of angular frequency for $Ca_{mag} = 4$ (blue lines), $Ca_{mag} = 10$ (red lines) and $Ca_{mag} = 16$ (green lines). Solid lines are for the magnetic field in the x-direction and dashed lines are for the magnetic field in the y-direction.

where τ' and τ'' are the in-phase and out-of-phase components with the strain, also normalized by σ/a. As seen in figure 5.23, the magnetic field in the x-direction produces a π rad phase shift in relation to the y-direction, which implies negative amplitudes in the decomposition. Therefore, in order to compare the in-phase and out-of-phase components for both magnetic field orientations, we adopt $\alpha = -1$ when the magnetic field is in x-direction and $\alpha = 1$ for magnetic fields in the y-direction.

Figures 5.24 and 5.25 show both of the aforementioned torque components. As can be seen, the general behavior is comparable to that seen for the magnetization components and θ_{mag} in terms of angular frequency, including the crossover point at the same oscillation frequency. Notably, the in-phase component exhibits a gradual rise in the plateau area, with torques for the magnetic field in the x-direction of around 0.03, 0.044 and 0.046 for $Ca_{mag} = 4$, 10 and 16, correspondingly. Given this situation, it is clear that the rise in Ca_{mag} from 10 to 16 is not substantial due to θ_{mag} cancels out the increase in magnetization magnitude. The plateau region for the magnetic field in the y-direction corresponds to torques of around 0.05, 0.17, and 0.31 for $Ca_{mag} = 4$, 10, and 16, respectively. The curves for $Ca_{mag} = 16$ and magnetic fields in the x-direction are interestingly almost identical to those for $Ca_{mag} = 4$ and magnetic fields in the y-direction.

6 Conclusions

The current work presented a three-dimensional computational analysis of a dilute ferrofluid emulsion exposed to a small amplitude oscillatory shear flow and an external magnetic field. The domain was discretized using the finite-difference method, with the interface captured using the level-set method and a semi-implicit projection method to solve the Navier-Stokes equations.

We assessed the droplet behavior in relation to the angular frequency, magnetic field direction and strength. We set the strain amplitude to $\gamma_0 = 0.1$, producing a small amplitude oscillatory shear flow, in order to guarantee a linear regime and avoid the formation of any higher harmonics. These assumptions allowed the evaluation of the morphological, rheological, and magnetization behaviors of the emulsion, including droplet geometry, viscoelastic characteristics, normal stress differences, and magnetization characteristics such as bulk magnetization, the angle between $\langle \mathbf{M} \rangle$ and $\mathbf{H}_0$, and the magnetic torque.

In terms of the morphology of the emulsion, we discovered that droplet deformation is mainly indifferent to the magnetic field direction, whether it is in the x or y-directions, with rising Ca_{mag} leading to even more droplet deformation. However, depending on the magnetic field direction, the droplet behavior in terms of its inclination angle did change dramatically. The droplet is constrained to areas of smaller effective shear for magnetic fields in the x-direction, attenuating the effects of the flow on the droplet and lowering the inclination angle amplitude. The droplet is stretched alongside the main velocity gradient for magnetic fields in the y-direction, putting it under more effective shear and causing larger inclination angle amplitudes. In both situations, the inclination angle decreases as the magnetic capillary number grows.

When the magnetic field was oriented in the z-direction, a novel phenomenon has been seen. The droplet in this case is elongated perpendicular to the shear plane while staying almost circular in the shear plane, barely affecting the oscillations of θ. Although increased magnetic capillary numbers result in smaller deformations for low oscillation frequencies, this impact reduces the effective relaxation time of the droplet, which causes the deformation curves to converge into one for high oscillation frequencies.

The viscoelastic properties are therefore a direct result of these behaviors based on these geometric dynamics. The emulsion displayed a mainly viscous behavior at low frequencies, with $G" \ll G'$, for magnetic fields in the x and y-directions. High oscillation

frequencies led G' to a plateau region, where $G' \gg G$", corresponding to an elastic behavior, *i.e.*, a Hookean solid. Additionally, it shows that the crossover point between G' and G" is not significantly different, indicating that the droplet effective relaxation time is unaffected by both the x and y magnetic fields. Despite these similarities, the magnetic field in the x-direction reduces both viscoelastic components as Ca_{mag} rises, which is a direct result of the magnetic field constriction of the droplet. Both viscoelastic components increase with Ca_{mag} in the y-direction since the magnetic field projects the droplet into an area with a larger effective shear-rate. For magnetic fields in the z-direction, there is a balance between the influence of the droplet area in the shear plane and its projected area in the flow. Smaller deformations at low oscillation frequencies lead to a reduction in both viscoelastic components with increasing Ca_{mag}. In contrast, at high oscillation frequencies, the convergence of the droplet deformations as Ca_{mag} increases leads to increases in both viscoelastic moduli.

Regarding the normal stress differences, we found that the anisotropies produced by the magnetic field depend only on its strength and direction.

The droplet dynamics have a direct impact on the magnetization characteristics. While the bulk magnetization grows as Ca_{mag} increases, confinement effects caused by the magnetic field in the x-direction reduce the impact on the periodic component of the bulk magnetization vector and, as a result, on θ_{mag}. Given that the reduction in θ_{mag} is overcome by the rise in bulk magnetization, there is a magnetic torque that grows with Ca_{mag} and aligns the droplet with the magnetic field. As the magnetic field intensity rises in the y-direction, the droplet elongates to an area with a greater effective shear rate, increasing the bulk magnetization magnitude, the periodic component of the magnetization vector, and, therefore, the angle between $\langle \mathbf{M} \rangle$ and $\mathbf{H}_0$. As Ca_{mag} grows, there is an increasing magnetic torque occurring. It is important to note that all of these properties had the same crossover point, demonstrating a strong dependency on $\langle \mathbf{M} \rangle$, θ_{mag}, and $\boldsymbol{\tau}_{mag}$ on the droplet interfacial properties. The droplet also exhibits a finite magnetization relaxation time while being superparamagnetic due to its interfacial dynamics.

7 Future work

Within the possible ways to expand the present study, there are two main aspects to be explored and consolidated about magnetic emulsions. The first point is the improvement of the algorithm implemented in this study. Although the results are in complete agreement with the experimental and theoretical models, it is still necessary to increase the versatility of computational models in order to expand their applicability. Thus, a suggestion is to migrate the present algorithm, for example, for a coupled level set/volume-of-fluid (CLSVOF) (Sussman; Puckett, 2000) and combine the advantages of each method. Still, on this topic, it is strongly recommended to optimize the code for both serial and parallel processing.

The second main point is related to the physics of the problem. Future studies on the current topic presented in this thesis are therefore suggested in order to elucidate other behaviors. Within this perspective the first one would be to evaluate the influence of capillary number within the linear regime of viscoelasticity, *i.e.*, to verify how G' and G'' change for the same frequency when varying the strain amplitude and the magnetic capillarity number. It would also be possible to verify the influence of the magnetic field on the limit of linear viscoelasticity or even if it is possible that the magnetic field changes the dilute emulsion behavior based on the magnetic interaction among the ferrofluid droplets.

The prospect of the present thesis serves as a continuous impulse for spur to future research. It is possible to migrate the present work to the LAOS regime (Large amplitude oscillatory shear) and investigate the influence of the magnetic field and oscillatory field in the pattern of formation of larger harmonics. Or, with a small change in dynamics, implement LAOE (Large amplitude oscillatory extensional) to quantify the dynamics, rheology and magnetization properties in the emulsion.

Finally, as another suggestion for further work, it is possible to investigate the emulsion response in a simultaneous combination of magnetic field and oscillatory flow, with simple or compound droplets. Another area to be explored concerns magneto hyperthermia, where the main objective would be to explore the thermodynamic properties of the droplet in the presence of an oscillating magnetic field. Finally, exploring the possible effects of an electric field in all these previous combinations and conditions is extremely relevant and constitutes an important objective in the scope of future works.

Appendix

A Shear characteristic time

In order to present the mathematical and numerical model used in Sec. 5.1, this appendix is intended to give a more detailed explanation about the approach based on the shear characteristic time for $\lambda = 1$.

The non-dimensional parameters are as follow: $\mathbf{u}^* = \mathbf{u}/\dot{\gamma}a$, $t^* = t\dot{\gamma}$, $\mathbf{x}^* = \mathbf{x}/a$, $p^* = p/\rho_c a^2\dot{\gamma}^2$, $\lambda^*(\mathbf{x}) = \eta(\mathbf{x})/\eta_c$, $\rho^*(\mathbf{x}) = \rho(\mathbf{x})\rho_c$, $\mathbf{H}^* = \mathbf{H}/|\mathbf{H}_0|$, $\kappa^* = a\kappa$, $\delta(\mathbf{x})^* = a\delta(\mathbf{x})$, $\mathbf{D}^* = \mathbf{D}/\dot{\gamma}$ and $\nabla^* = a\nabla$. Substituting each value in Eq. 3.14 and suppressing, for convenience, the superscript *, we have

$$\begin{aligned}\frac{\partial \mathbf{u}}{\partial t} + \mathbf{u}.\nabla\mathbf{u} = -\nabla p + \frac{1}{Re}\nabla.(2\mathbf{D}) + \frac{Ca_{mag}}{CaRe}(\zeta(\mathbf{x}) - 1)\mathbf{H}.\nabla\mathbf{H} \\ -\frac{1}{CaRe}\kappa\delta(|\mathbf{x} - \mathbf{x}_{\partial\Omega}|)\hat{\mathbf{n}}\,.\end{aligned} \tag{A.1}$$

Here, in this cases, the non-dimensional parameters are the same as in Sec. 3.5: Re, Ca and Ca_{mag}. The only difference is that instead of using the shear-rate amplitude, $\dot{\gamma}_0$, it is used the shear-rate, $\dot{\gamma}$, *i.e.*, $Re = \rho_c\dot{\gamma}a^2/\eta_c$, $Ca = \eta_c a\dot{\gamma}/\sigma$ and $Ca_{mag} = \mu_0 a H_0^2/\sigma$

The upper and botom wall velocities in Fig. 3.1 are given by

$$\mathbf{u} = \pm\frac{L_y}{2}\,. \tag{A.2}$$

Also substituting the non-dimensional parameters in Eqs. 3.22 and 3.25, we found the non-dimensional bulk stress tensor scaled by $\eta_c\dot{\gamma}$

$$\boldsymbol{\Sigma}_b = -\frac{1}{V}\int_{\Omega_c} pdV\mathbf{I} + \frac{1}{V}\int_{\Omega_c}(\nabla\mathbf{u} + \nabla\mathbf{u}^T)dV + \boldsymbol{\Sigma}^D\,, \tag{A.3}$$

$$\boldsymbol{\Sigma}^D = \frac{Re}{V}\int_{\partial\Omega}\left[\mathbf{x}\left(\frac{\kappa}{Ca} - \frac{Ca_{mag}}{2Ca}(\zeta - 1)\mathbf{H}^2\right)\hat{\mathbf{n}}\right]d\Omega\,. \tag{A.4}$$

The reduced viscosity, in Eq. 5.1, is defined as (Schramm, 2014)

$$[\eta] = \frac{\frac{\eta_b}{\eta_d} - 1}{\beta} = \frac{\eta_b - \eta_c}{\eta_c\beta}, \tag{A.5}$$

where η_b is the viscosity of the emulsion. Once $\eta_b = \Sigma_{b:yx}/\dot{\gamma}$ and $\eta_c = \Sigma_{c:yx}/\dot{\gamma}$, the equation reduces to

$$[\eta] = \frac{\Sigma_{b:yx} - \eta_c\dot{\gamma}}{\eta_c\dot{\gamma}\beta}\,. \tag{A.6}$$

Noting that, in simple shear,

$$\Sigma_{b:yx} = \int_{\Omega_c} \eta_c \frac{\partial \mathbf{u}}{\partial y} d\Omega_c + \Sigma^D_{yx} = \eta_c\dot{\gamma} + \Sigma^D_{yx}\,, \tag{A.7}$$

Eq. A.6 reduces to

$$[\eta] = \frac{\Sigma^D_{yx}}{\eta_c\dot{\gamma}\beta}\,, \tag{A.8}$$

which is given, taking advantage of the non-dimensional form of Σ^D_{yx}, as

$$[\eta] = \frac{\Sigma^D_{yx}}{\beta}\,, \tag{A.9}$$

The projection method follows the same methodology as described in Sec. 4.2. In a similar way, the boundary conditions in Sec. 4.4, but without the term Ca/Re in Eq. 4.40. The equations are given by

$$\frac{1}{2\Delta t}\left(3\mathbf{u}^* - 4\mathbf{u}^n + \mathbf{u}^{n-1}\right) - \frac{1}{Re}\nabla^2\mathbf{u}^* = \mathbf{G}(\hat{\mathbf{u}}) + \mathbf{F}_C(\hat{\phi}) + \mathbf{F}_M(\hat{\phi}, \hat{H})\,, \tag{A.10}$$

$$\mathbf{u}^{n+1} = \mathbf{u}^* - \frac{2\Delta t}{3}\nabla(q^{n+1})\,, \tag{A.11}$$

$$\nabla^2 q^{n+1} = \frac{3}{2\Delta t}\nabla\cdot\mathbf{u}^*, \tag{A.12}$$

$$p^{n+1} = q^{n+1} - \nabla\cdot\mathbf{u}^*, \tag{A.13}$$

where $\mathbf{G}$, $\mathbf{F}_c$ and $\mathbf{F}_{mag}$ are

$$\mathbf{G}(\hat{\mathbf{u}}) = -\hat{\mathbf{u}}\cdot\nabla\hat{\mathbf{u}} - \frac{1}{Re}\nabla^2\hat{\mathbf{u}} + \frac{1}{Re}\nabla\cdot[(\nabla\hat{\mathbf{u}} + \nabla\hat{\mathbf{u}}^T)]\,, \tag{A.14}$$

$$\mathbf{F}_c(\hat{\phi}) = -\frac{1}{CaRe}\kappa(\hat{\phi})\delta_\epsilon(\hat{\phi})|\nabla\hat{\phi}|\hat{\mathbf{n}}, \tag{A.15}$$

$$\mathbf{F}_{mag}(\hat{\phi}, \hat{\mathbf{H}}) = \frac{Ca_{mag}}{CaRe}[(\zeta(\hat{\phi}) - 1)\hat{\mathbf{H}}.\nabla\hat{\mathbf{H}}]. \tag{A.16}$$

The discretization follows the same methodology as described in Sec. 4.3, needing only few adaptations in the linear systems. Finally, as an additional information, there is a relation between both characteristic times. Comparing both the relaxation times and angular frequencies in its respective scales, it is possible to write

$$\frac{t_{droplet}}{t_{shear}} = \frac{\omega_{droplet}}{\omega_{shear}} = \frac{\eta_c a\dot{\gamma}}{\sigma} = Ca\,. \tag{A.17}$$

By applying Eq. A.17 in Eq. 3.20, it follows immediately that the amplitude in the shear time scale is $1/\omega_{shear}$. Since the strain amplitude is the same regardless the time scale, *i.e.*, $\dot{\gamma}_{0,droplet} = \dot{\gamma}_{0,shear}$, both simulations can be interchanged between time scales by changing the angular frequency. For example, $\dot{\gamma}_0 = 0.1$, $\omega_{droplet} = 5$ and $Ca = 0.3$ in the droplet time scale is equivalent to $\dot{\gamma}_0 = 0.1$, $\omega = 10$ and $Ca = 0.3$ in the shear time scale.

Comparing the bulk stress in Eqs. 3.26 and A.3, it is also possible to write

$$\mathbf{\Sigma}_{droplet} = Ca\mathbf{\Sigma}_{shear}. \tag{A.18}$$

B Variable viscosity

The variable viscosity can be implemented by taking into account the term $\lambda(\mathbf{x})$ into Eqs. 4.21 and A.10. The full form is given by

$$\nabla \cdot (2\lambda(\mathbf{x})\mathbf{D}) = \nabla \cdot (\lambda(\mathbf{x})(\nabla \mathbf{u} + \nabla \mathbf{u}^T)) \,. \tag{B.1}$$

Developing the term in index notation, we have

$$\nabla \cdot (\lambda(\mathbf{x})(\nabla \mathbf{u} + \nabla \mathbf{u}^T)) = \frac{\partial}{\partial x_k}\left(\lambda(\mathbf{x})\frac{\partial u_i}{\partial x_k} + \lambda(\mathbf{x})\frac{\partial u_k}{\partial x_i}\right) , \tag{B.2}$$

which results in the x, y and z-directions, respectively, for the velocity field $\mathbf{u} = (u, v, w)$ and i, j, k being the grid index.

$$2\frac{\partial}{\partial x}\left(\lambda(\mathbf{x})\frac{\partial u}{\partial x}\right) + \frac{\partial}{\partial y}\left(\lambda(\mathbf{x})\frac{\partial u}{\partial y} + \lambda(\mathbf{x})\frac{\partial v}{\partial x}\right) + \frac{\partial}{\partial z}\left(\lambda(\mathbf{x})\frac{\partial u}{\partial z} + \lambda(\mathbf{x})\frac{\partial w}{\partial x}\right) , \tag{B.3}$$

$$\frac{\partial}{\partial x}\left(\lambda(\mathbf{x})\frac{\partial v}{\partial x} + \lambda(\mathbf{x})\frac{\partial u}{\partial y}\right) + 2\frac{\partial}{\partial y}\left(\lambda(\mathbf{x})\frac{\partial v}{\partial y}\right) + \frac{\partial}{\partial z}\left(\lambda(\mathbf{x})\frac{\partial v}{\partial z} + \lambda(\mathbf{x})\frac{\partial w}{\partial y}\right) , \tag{B.4}$$

$$\frac{\partial}{\partial x}\left(\lambda(\mathbf{x})\frac{\partial w}{\partial x} + \lambda(\mathbf{x})\frac{\partial u}{\partial z}\right) + \frac{\partial}{\partial y}\left(\lambda(\mathbf{x})\frac{\partial w}{\partial y} + \lambda(\mathbf{x})\frac{\partial v}{\partial z}\right) + 2\frac{\partial}{\partial z}\left(\lambda(\mathbf{x})\frac{\partial w}{\partial z}\right) . \tag{B.5}$$

Based on the previous equations, the discretization of each term is:

$$\frac{\partial}{\partial x}\left(\lambda(\mathbf{x})\frac{\partial u}{\partial x}\right) = \frac{\left(\lambda\frac{\partial u}{\partial x}\right)_{i+1/2} - \left(\lambda\frac{\partial u}{\partial x}\right)_{i-1/2}}{\Delta x} = \frac{\lambda_{i+1,j,k}(u_{i+1,j,k} - u_{i,j,k}) - \lambda_{i,j,k}(u_{i,j,k} - u_{i-1,j,k})}{(\Delta x)^2} \tag{B.6}$$

$$\frac{\partial}{\partial y}\left(\lambda(\mathbf{x})\frac{\partial u}{\partial y}\right) = \frac{\left(\lambda\frac{\partial u}{\partial y}\right)_{j+1/2} - \left(\lambda\frac{\partial u}{\partial y}\right)_{j-1/2}}{\Delta y} = \frac{\lambda_{i+1/2,j+1/2,k}(u_{i,j+1,k} - u_{i,j,k}) - \lambda_{i+1/2,j-1/2,k}(u_{i,j,k} - u_{i,j-1,k})}{(\Delta y)^2} \tag{B.7}$$

$$\frac{\partial}{\partial y}\left(\lambda(\mathbf{x})\frac{\partial v}{\partial x}\right) = \frac{\left(\lambda\frac{\partial v}{\partial x}\right)_{j+1/2} - \left(\lambda\frac{\partial v}{\partial x}\right)_{j-1/2}}{\Delta y} = \frac{\lambda_{i+1/2,j+1/2,k}(v_{i+1,j,k} - v_{i,j,k}) - \lambda_{i+1/2,j-1/2,k}(v_{i+1,j-1,k} - v_{i,j-1,k})}{\Delta y \Delta x} \tag{B.8}$$

$$\frac{\partial}{\partial z}\left(\lambda(\mathbf{x})\frac{\partial u}{\partial z}\right) = \frac{\left(\lambda\frac{\partial u}{\partial z}\right)_{k+1/2} - \left(\lambda\frac{\partial u}{\partial z}\right)_{k-1/2}}{\Delta z} = \frac{\lambda_{i+1/2,j,k+1/2}(u_{i,j,k+1} - u_{i,j,k}) - \lambda_{i+1/2,j,k-1/2}(u_{i,j,k} - u_{i,j,k-1})}{(\Delta z)^2} \tag{B.9}$$

$$\frac{\partial}{\partial z}\left(\lambda(\mathbf{x})\frac{\partial w}{\partial x}\right) = \frac{\left(\lambda\frac{\partial w}{\partial x}\right)_{k+1/2} - \left(\lambda\frac{\partial w}{\partial x}\right)_{k-1/2}}{\Delta x} = \frac{\lambda_{i+1/2,j,k+1/2}(w_{i+1,j,k} - w_{i,j,k}) - \lambda_{i+1/2,j,k-1/2}(w_{i+1,j,k-1} - w_{i,j,k-1})}{\Delta z \Delta x} \tag{B.10}$$

$$\frac{\partial}{\partial y}\left(\lambda(\mathbf{x})\frac{\partial v}{\partial y}\right) = \frac{\left(\lambda\frac{\partial v}{\partial y}\right)_{j+1/2} - \left(\lambda\frac{\partial v}{\partial y}\right)_{j-1/2}}{\Delta x} = \frac{\lambda_{i+1,j,k}(u_{i+1,j,k} - u_{i,j,k}) - \lambda_{i,j,k}(u_{i,j,k} - u_{i-1,j,k})}{(\Delta x)^2} \tag{B.11}$$

$$\frac{\partial}{\partial x}\left(\lambda(\mathbf{x})\frac{\partial v}{\partial x}\right) = \frac{\left(\lambda\frac{\partial v}{\partial x}\right)_{i+1/2} - \left(\lambda\frac{\partial v}{\partial x}\right)_{i-1/2}}{\Delta x} = \frac{\lambda_{i+1/2,j+1/2,k}(v_{i+1,j,k} - v_{i,j,k}) - \lambda_{i-1/2,j+1/2,k}(v_{i,j,k} - v_{i-1,j,k})}{(\Delta y)^2} \tag{B.12}$$

$$\frac{\partial}{\partial x}\left(\lambda(\mathbf{x})\frac{\partial u}{\partial y}\right) = \frac{\left(\lambda\frac{\partial u}{\partial y}\right)_{i+1/2} - \left(\lambda\frac{\partial u}{\partial y}\right)_{i-1/2}}{\Delta y} = \frac{\lambda_{i+1/2,j+1/2,k}(u_{i,j+1,k} - u_{i,j,k}) - \lambda_{i-1/2,j+1/2,k}(u_{i-1,j+1,k} - u_{i-1,j,k})}{\Delta y \Delta x} \tag{B.13}$$

$$\frac{\partial}{\partial z}\left(\lambda(\mathbf{x})\frac{\partial v}{\partial z}\right) = \frac{\left(\lambda\frac{\partial v}{\partial z}\right)_{k+1/2} - \left(\lambda\frac{\partial v}{\partial z}\right)_{k-1/2}}{\Delta z} = \frac{\lambda_{i+1/2,j,k+1/2}(v_{i,j,k+1} - v_{i,j,k}) - \lambda_{i+1/2,j,k-1/2}(v_{i,j,k} - v_{i,j,k-1})}{(\Delta z)^2} \tag{B.14}$$

$$\frac{\partial}{\partial z}\left(\lambda(\mathbf{x})\frac{\partial w}{\partial y}\right) = \frac{\left(\lambda\frac{\partial w}{\partial y}\right)_{k+1/2} - \left(\lambda\frac{\partial w}{\partial y}\right)_{k-1/2}}{\Delta x} = \frac{\lambda_{i,j+1/2,k+1/2}(w_{i,j+1,k} - w_{i,j,k}) - \lambda_{i+1/2,j,k-1/2}(w_{i,j+1,k-1} - w_{i,j,k-1})}{\Delta z \Delta x} \tag{B.15}$$

$$\frac{\partial}{\partial z}\left(\lambda(\mathbf{x})\frac{\partial w}{\partial z}\right) = \frac{\left(\lambda\frac{\partial w}{\partial z}\right)_{k+1/2} - \left(\lambda\frac{\partial w}{\partial z}\right)_{k-1/2}}{\Delta z} = \frac{\lambda_{i+1,j,k}(u_{i+1,j,k} - u_{i,j,k}) - \lambda_{i,j,k}(u_{i,j,k} - u_{i-1,j,k})}{(\Delta x)^2} \tag{B.16}$$

$$\frac{\partial}{\partial x}\left(\lambda(\mathbf{x})\frac{\partial w}{\partial x}\right) = \frac{\left(\lambda\frac{\partial w}{\partial x}\right)_{i+1/2} - \left(\lambda\frac{\partial w}{\partial x}\right)_{i-1/2}}{\Delta x} = \frac{\lambda_{i+1/2,j,k+1/2}(w_{i+1,j,k} - w_{i,j,k}) - \lambda_{i-1/2,j,k+1/2}(w_{i-1,j,k} - w_{i-1,j,k})}{(\Delta x)^2} \tag{B.17}$$

$$\frac{\partial}{\partial x}\left(\lambda(\mathbf{x})\frac{\partial u}{\partial z}\right) = \frac{\left(\lambda\frac{\partial u}{\partial z}\right)_{i+1/2} - \left(\lambda\frac{\partial u}{\partial z}\right)_{i-1/2}}{\Delta y} = \frac{\lambda_{i+1/2,j,k+1/2}(u_{i,j,k+1} - u_{i,j,k}) - \lambda_{i-1/2,j,k+1/2}(u_{i-1,j,k+1} - u_{i-1,j,k})}{\Delta z \Delta x} \tag{B.18}$$

$$\frac{\partial}{\partial y}\left(\lambda(\mathbf{x})\frac{\partial w}{\partial y}\right) = \frac{\left(\lambda\frac{\partial w}{\partial y}\right)_{j+1/2} - \left(\lambda\frac{\partial w}{\partial y}\right)_{j-1/2}}{\Delta y} = \frac{\lambda_{i,j+1/2,k+1/2}(w_{i,j+1,k} - w_{i,j,k}) - \lambda_{i,j-1/2,k+1/2}(w_{i,j,k} - w_{i,j-1,k})}{(\Delta y)^2} \tag{B.19}$$

$$\frac{\partial}{\partial y}\left(\lambda(\mathbf{x})\frac{\partial v}{\partial z}\right) = \frac{\left(\lambda\frac{\partial v}{\partial z}\right)_{j+1/2} - \left(\lambda\frac{\partial v}{\partial z}\right)_{j-1/2}}{\Delta z} = \frac{\lambda_{i,j+1/2,k+1/2}(v_{i,j,k+1} - v_{i,j,k}) - \lambda_{i,j-1/2,k+1/2}(w_{i,j-1,k+1} - w_{i,j-1,k})}{\Delta y \Delta z} \tag{B.20}$$

Bibliography

Abdo, R. F.; Abicalil, V. G.; Cunha, L. H.; Oliveira, T. F. On the rheology and magnetization of dilute magnetic emulsions under small amplitude oscillatory shear. *Journal of Fluid Mechanics*, Cambridge University Press, v. 955, p. A3, 2023.

Abicalil, V. G. Rheology and magnetization of dilute ferrofluid emulsions. University of Brasília (Master's dissertation), 2021.

Abicalil, V. G. e.; Abdo, R. F.; Cunha, L. H. P. da; Oliveira, T. F. de. On the magnetization of dilute ferrofluid emulsions in shear flows. *Physics of Fluids*, v. 33, n. 5, p. 053313, 2021. Available on: <https://doi.org/10.1063/5.0050643>.

Andablo-Reyes, E.; Hidalgo-Álvarez, R.; Vicente, J. de. Controlling friction using magnetic nanofluids. *Soft Matter*, Royal Society of Chemistry, v. 7, n. 3, p. 880–883, 2011. Available on: <http://dx.doi.org/10.1039/C0SM00251H>.

Anderson, J. *Computational Fluid Dynamics*. McGraw-Hill Education, 1995. (Computational Fluid Dynamics: The Basics with Applications). ISBN 9780070016859. Available on: <https://books.google.com.br/books?id=dJceAQAAIAAJ>.

Ashaolu, T. J. Nanoemulsions for health, food, and cosmetics: a review. *Environmental Chemistry Letters*, v. 19, n. 4, p. 3381–3395, Aug 2021. ISSN 1610-3661. Available on: <https://doi.org/10.1007/s10311-021-01216-9>.

Ashrafizadeh, S.; Kamran, M. Emulsification of heavy crude oil in water for pipeline transportation. *Journal of Petroleum Science and Engineering*, v. 71, n. 3, p. 205–211, 2010. ISSN 0920-4105. Fourth International Symposium on Hydrocarbons and Chemistry. Available on: <https://www.sciencedirect.com/science/article/pii/S0920410510000434>.

Badalassi, V.; Ceniceros, H.; Banerjee, S. Computation of multiphase systems with phase field models. *Journal of Computational Physics*, v. 190, n. 2, p. 371–397, 2003. ISSN 0021-9991. Available on: <https://www.sciencedirect.com/science/article/pii/S0021999103002808>.

Bai, L.; Huan, S.; Rojas, O. J.; McClements, D. J. Recent innovations in emulsion science and technology for food applications. *Journal of Agricultural and Food Chemistry*, -, n. -, p. –, 2021. PMID: 33982568. Available on: <https://doi.org/10.1021/acs.jafc.1c01877>.

Barai, N.; Mandal, N. Breakup modes of fluid drops in confined shear flows. *Physics of Fluids*, v. 28, n. 7, p. 073302, 2016. Available on: <https://aip.scitation.org/doi/abs/10.1063/1.4954995>.

Barnes, H.; Hutton, J.; Walters, K. *An Introduction to Rheology*. Elsevier Science, 1989. (Rheology Series). ISBN 9780444871404. Available on: <https://books.google.com.br/books?id=B1e0uxFg4oYC>.

Batchelor, G. K. The stress system in a suspension of force-free particles. *Journal of Fluid Mechanics*, Cambridge University Press, v. 41, n. 3, p. 545–570, 1970.

Batchelor, G. K. *An Introduction to Fluid Dynamics*. : Cambridge University Press, 2000. (Cambridge Mathematical Library).

Bielas, R.; Jameel, B.; Skumiel, A.; Timko, M.; Kopčanský, P.; Józefczak, A. Magnetic pickering emulsions heated in a rotating magneticfield. *Journal of Magnetism and Magnetic Materials*, v. 563, p. 169946, 2022. ISSN 0304-8853. Available on: <https://www.sciencedirect.com/science/article/pii/S0304885322008319>.

Bijarchi, M. A.; Dizani, M.; Honarmand, M.; Shafii, M. B. Splitting dynamics of ferrofluid droplets inside a microfluidic t-junction using a pulse-width modulated magnetic field in micro-magnetofluidics. *Soft Matter*, Royal Society of Chemistry, v. 17, n. 5, p. 1317–1329, 2021. Available on: <http://dx.doi.org/10.1039/D0SM01764G>.

Bijarchi, M. A.; Favakeh, A.; Sedighi, E.; Shafii, M. B. Ferrofluid droplet manipulation using an adjustable alternating magnetic field. *Sensors and Actuators A: Physical*, v. 301, p. 111753, 2020. ISSN 0924-4247. Available on: <https://www.sciencedirect.com/science/article/pii/S0924424719312804>.

Bird, R.; Armstrong, R.; Hassager, O. *Dynamics of polymeric liquids, Volume 1: Fluid mechanics*. 2. ed. : Wiley, 1987.

Boudoukhani, M.; Moulai-Mostefa, N.; Hammani, S. Prediction of rheological properties and interfacial tension of mixtures of immiscible polypropylene-polystyrene (pp3/ps) blends. *Walailak Journal of Science and Technology (WJST)*, v. 17, n. 7, p. 665–677, Jul. 2020. Available on: <https://wjst.wu.ac.th/index.php/wjst/article/view/3294>.

Bousmina, M. Rheology of polymer blends: linear model for viscoelastic emulsions. *Rheologica Acta*, v. 38, p. 73–83, 1999. Available on: <https://link.springer.com/article/10.1007/s003970050157>.

Brown, P.; Butts, C. P.; Cheng, J.; Eastoe, J.; Russell, C. A.; Smith, G. N. Magnetic emulsions with responsive surfactants. *Soft Matter*, The Royal Society of Chemistry, v. 8, p. 7545–7546, 2012. Available on: <http://dx.doi.org/10.1039/C2SM26077H>.

Capobianchi, P.; Lappa, M.; Oliveira, M. S. N.; Pinho, F. T. Shear rheology of a dilute emulsion of ferrofluid droplets dispersed in a nonmagnetizable carrier fluid under the influence of a uniform magnetic field. *Journal of Rheology*, v. 65, n. 5, p. 925–941, 2021. Available on: <https://doi.org/10.1122/8.0000226>.

Carvalho-Guimarães, F. B. de; Correa, K. L.; Souza, T. P. de; Amado, J. R. R.; Ribeiro-Costa, R. M.; Silva-Júnior, J. O. C. A review of pickering emulsions: Perspectives and applications. *Pharmaceuticals*, v. 15, n. 11, 2022. ISSN 1424-8247. Available on: <https://www.mdpi.com/1424-8247/15/11/1413>.

Cavallo, R.; Guido, S.; Simeone, M. Drop deformation under small-amplitude oscillatory shear flow. *Rheologica Acta*, v. 42, n. 1, p. 1–9, 2003. Available on: <https://link.springer.com/article/10.1007/s00397-002-0245-z>.

Chang-Zhi, L.; Lie-Jin, G. Numerical simulation of drop deformation and breakup in shear flow. *Heat Transfer—Asian Research*, v. 36, n. 5, p. 286–294, 2007. Available on: <https://onlinelibrary.wiley.com/doi/abs/10.1002/htj.20160>.

Chen, D.; Yang, Z.; Ji, Y.; Dai, Y.; Feng, L.; Arai, F. Deformable ferrofluid-based millirobot with high motion accuracy and high output force. *Applied Physics Letters*, AIP Publishing LLC, v. 118, n. 13, p. 134101, 2021. Available on: <https://doi.org/10.1063/5.0042893>.

Chen, J.; Vogel, R.; Werner, S.; Heinrich, G.; Clausse, D.; Dutschk, V. Influence of the particle type on the rheological behavior of pickering emulsions. *Colloids and Surfaces A: Physicochemical and Engineering Aspects*, v. 382, n. 1, p. 238–245, 2011. ISSN 0927-7757. A collection of papers from the 8th EUFOAM Conference and the Meetings of COST Actions D43 and P21. Available on: <https://www.sciencedirect.com/science/article/pii/S0927775711000999>.

Chorin, A. J. Numerical solution of the navier-stokes equations. *Mathematics of Computation*, American Mathematical Society, v. 22, n. 104, p. 745–762, 1968. ISSN 00255718, 10886842. Available on: <http://www.jstor.org/stable/2004575>.

Cunha, F. R.; Rosa, A. P. Effect of particle dipolar interactions on the viscoelastic response of dilute ferrofluids undergoing oscillatory shear. *Physics of Fluids*, v. 33, n. 9, p. 092004, 2021. Available on: <https://doi.org/10.1063/5.0064960>.

Cunha, L.; Siqueira, I.; Albuquerque, E.; Oliveira, T. Flow of emulsion drops through a constricted microcapillary channel. *International Journal of Multiphase Flow*, v. 103, p. 141–150, 2018. ISSN 0301-9322. Available on: <https://www.sciencedirect.com/science/article/pii/S0301932217304895>.

Cunha, L. H.; Siqueira, I. R.; Campos, A. A.; Rosa, A. P.; Oliveira, T. F. A numerical study on heat transfer of a ferrofluid flow in a square cavity under simultaneous gravitational and magnetic convection. *Theoretical and Computational Fluid Dynamics*, Springer, v. 34, n. 1, p. 119–132, 2020. Available on: <https://doi.org/10.1007/s00162-020-00515-1>.

Cunha, L. H. P.; Siqueira, I. R.; Cunha, F. R.; Oliveira, T. F. Effects of external magnetic fields on the rheology and magnetization of dilute emulsions of ferrofluid droplets in shear flows. *Physics of Fluids*, v. 32, n. 7, p. 073306, 2020. Available on: <https://doi.org/10.1063/5.0009983>.

Cunha, L. H. P.; Siqueira, I. R.; Oliveira, T. F.; Ceniceros, H. D. Field-induced control of ferrofluid emulsion rheology and droplet break-up in shear flows. *Physics of Fluids*, v. 30, n. 12, p. 122110, 2018. Available on: <https://doi.org/10.1063/1.5055943>.

Darbon, J.; Osher, S. Algorithms for overcoming the curse of dimensionality for certain hamilton–jacobi equations arising in control theory and elsewhere. *Research in the Mathematical Sciences*, v. 3, n. 1, p. 19, Sep 2016. ISSN 2197-9847. Available on: <https://doi.org/10.1186/s40687-016-0068-7>.

Das, P.; Colombo, M.; Prosperi, D. Recent advances in magnetic fluid hyperthermia for cancer therapy. *Colloids and Surfaces B: Biointerfaces*, v. 174, p. 42–55, 2019. ISSN 0927-7765. Available on: <https://www.sciencedirect.com/science/article/pii/S0927776518307495>.

Debnath, B. K.; Saha, U. K.; Sahoo, N. A comprehensive review on the application of emulsions as an alternative fuel for diesel engines. *Renewable and Sustainable Energy Reviews*, v. 42, p. 196–211, 2015. ISSN 1364-0321. Available on: <https://www.sciencedirect.com/science/article/pii/S1364032114008405>.

Dijk, N. P. van; Maute, K.; Langelaar, M.; Keulen, F. van. Level-set methods for structural topology optimization: a review. *Structural and Multidisciplinary Optimization*, v. 48, n. 3, p. 437–472, Sep 2013. ISSN 1615-1488. Available on: <https://doi.org/10.1007/s00158-013-0912-y>.

Dikansky, Y. I.; Zakinyan, A. R.; Tyatyushkin, A. N. Anisotropy of magnetic emulsions induced by magnetic and electric fields. *Phys. Rev. E*, American Physical Society, v. 84, p. 031402, Sep 2011. Available on: <https://link.aps.org/doi/10.1103/PhysRevE.84.031402>.

Dodd, M. S.; Ferrante, A. A fast pressure-correction method for incompressible two-fluid flows. *Journal of Computational Physics*, v. 273, p. 416–434, 2014. ISSN 0021-9991. Available on: <https://www.sciencedirect.com/science/article/pii/S0021999114003702>.

Einstein, A. Eine neue bestimmung der moleküldimensionen. *Annalen der Physik*, v. 324, n. 2, p. 289–306, 1906. Available on: <https://onlinelibrary.wiley.com/doi/abs/10.1002/andp.19063240204>.

Einstein, A. Berichtigung zu meiner arbeit: "eine neue bestimmung der moleküldimensionen". *Annalen der Physik*, v. 339, n. 3, p. 591–592, 1911. Available on: <https://onlinelibrary.wiley.com/doi/abs/10.1002/andp.19113390313>.

Fan, X.; Dong, X.; Karacakol, A. C.; Xie, H.; Sitti, M. Reconfigurable multifunctional ferrofluid droplet robots. *Proceedings of the National Academy of Sciences*, National Acad Sciences, v. 117, n. 45, p. 27916–27926, 2020. Available on: <https://doi.org/10.1073/pnas.2016388117>.

Fan, X.; Sun, M.; Sun, L.; Xie, H. Ferrofluid droplets as liquid microrobots with multiple deformabilities. *Advanced Functional Materials*, Wiley Online Library, v. 30, n. 24, p. 2000138, 2020. Available on: <https://doi.org/10.1002/adfm.202000138>.

Feigl, K.; Megias-Alguacil, D.; Fischer, P.; Windhab, E. J. Simulation and experiments of droplet deformation and orientation in simple shear flow with surfactants. *Chemical Engineering Science*, v. 62, n. 12, p. 3242–3258, 2007. ISSN 0009-2509. Available on: <https://www.sciencedirect.com/science/article/pii/S0009250907001637>.

Ferziger, J. H.; Perić, M. *Computational Methods for Fluid Dynamics*. 2nd. ed. Berlin: Springer, 1999.

Flament, C.; Lacis, S.; Bacri, J. C.; Cebers, A.; Neveu, S.; Perzynski, R. Measurements of ferrofluid surface tension in confined geometry. *Phys. Rev. E*, American Physical Society, v. 53, p. 4801–4806, May 1996. Available on: <https://link.aps.org/doi/10.1103/PhysRevE.53.4801>.

Fröhlich, A.; Sack, R. Theory of the rheological properties of dispersions. *Proceedings of the Royal Society of London. Series A. Mathematical and Physical Sciences*, v. 185, n. 1003, p. 415–430, 1946. Available on: <https://royalsocietypublishing.org/doi/abs/10.1098/rspa.1946.0028>.

Ghigliotti, G.; Biben, T.; Misbah, C. Rheology of a dilute two-dimensional suspension of vesicles. *Journal of Fluid Mechanics*, Cambridge University Press, v. 653, p. 489–518, 2010.

Gibou, F.; Fedkiw, R.; Osher, S. A review of level-set methods and some recent applications. *Journal of Computational Physics*, v. 353, p. 82–109, 2018. ISSN 0021-9991. Available on: <https://www.sciencedirect.com/science/article/pii/S0021999117307441>.

GRACE, H. P. Dispersion phenomena in high viscosity immiscible fluid systems and application of static mixers as dispersion devices in such systems. *Chemical Engineering Communications*, Taylor Francis, v. 14, n. 3-6, p. 225–277, 1982. Available on: <https://doi.org/10.1080/00986448208911047>.

Graebling, D.; Muller, R.; Palierne, J. F. Linear viscoelastic behavior of some incompatible polymer blends in the melt. interpretation of data with a model of emulsion of viscoelastic liquids. *Macromolecules*, v. 26, n. 2, p. 320–329, 1993. Available on: <https://doi.org/10.1021/ma00054a011>.

Guido, C. J.; Shaqfeh, E. S. The rheology of soft bodies suspended in the simple shear flow of a viscoelastic fluid. *Journal of Non-Newtonian Fluid Mechanics*, v. 273, p. 104183, 2019. ISSN 0377-0257. Available on: <https://www.sciencedirect.com/science/article/pii/S0377025719302010>.

Guido, S.; Grosso, M.; Maffettone, P. L. Newtonian drop in a newtonian matrix subjected to large amplitude oscillatory shear flows. *Rheologica Acta*, v. 43, n. 6, p. 575–583, Dec 2004. ISSN 1435-1528. Available on: <https://doi.org/10.1007/s00397-004-0388-1>.

Hamilton, J. K.; Gilbert, A. D.; Petrov, P. G.; Ogrin, F. Y. Torque driven ferromagnetic swimmers. *Physics of Fluids*, v. 30, n. 9, p. 092001, 2018. Available on: <https://doi.org/10.1063/1.5046360>.

Hartmann, D.; Meinke, M.; Schröder, W. The constrained reinitialization equation for level set methods. *Journal of Computational Physics*, v. 229, n. 5, p. 1514–1535, 2010. ISSN 0021-9991. Available on: <https://www.sciencedirect.com/science/article/pii/S0021999109006032>.

Hassan, M. R.; Wang, C. Magnetic field induced ferrofluid droplet breakup in a simple shear flow at a low reynolds number. *Physics of Fluids*, v. 31, n. 12, p. 127104, 2019. Available on: <https://doi.org/10.1063/1.5124134>.

Hassan, M. R.; Zhang, J.; Wang, C. Deformation of a ferrofluid droplet in simple shear flows under uniform magnetic fields. *Physics of Fluids*, v. 30, n. 9, p. 092002, 2018. Available on: <https://doi.org/10.1063/1.5047223>.

Hinch, E. J.; Acrivos, A. Long slender drops in a simple shear flow. *Journal of Fluid Mechanics*, Cambridge University Press, v. 98, n. 2, p. 305–328, 1980.

Ishida, S.; Matsunaga, D. Rheology of a dilute ferrofluid droplet suspension in shear flow: Viscosity and normal stress differences. *Phys. Rev. Fluids*, American Physical Society, v. 5, p. 123603, Dec 2020. Available on: <https://link.aps.org/doi/10.1103/PhysRevFluids.5.123603>.

Jacobs, U.; Fahrländer, M.; Winterhalter, J.; Friedrich, C. Analysis of palierne's emulsion model in the case of viscoelastic interfacial properties. *Journal of Rheology*, v. 43, n. 6, p. 1495–1509, 1999. Available on: <https://doi.org/10.1122/1.551056>.

Jaiswal, M.; Dudhe, R.; Sharma, P. K. Nanoemulsion: an advanced mode of drug delivery system. *3 Biotech*, v. 5, n. 2, p. 123–127, Apr 2015. ISSN 2190-5738. Available on: <https://doi.org/10.1007/s13205-014-0214-0>.

Jesus, W. C.; Roma, A. M.; Ceniceros, H. D. Deformation of a sheared magnetic droplet in a viscous fluid. *Communications in Computational Physics*, v. 24, n. 2, p. 332–355, 2018. ISSN 1991-7120. Available on: <http://global-sci.org/intro/article_detail/cicp/12243.html>.

Ji, Y.; Dai, Y.; Chen, D.; Gan, C.; Wang, L.; Feng, L. Precise control of ferrofluid droplet robot in 3-d vascular model. In: IEEE. *2021 WRC Symposium on Advanced Robotics and Automation (WRC SARA)*. 2021. p. 122–127.

Jiang, G.-S.; Peng, D. Weighted eno schemes for hamilton–jacobi equations. *SIAM Journal on Scientific Computing*, v. 21, n. 6, p. 2126–2143, 2000. Available on: <https://doi.org/10.1137/S106482759732455X>.

Jiang, G.-S.; Shu, C.-W. Efficient implementation of weighted eno schemes. *Journal of Computational Physics*, v. 126, n. 1, p. 202–228, 1996. ISSN 0021-9991. Available on: <https://www.sciencedirect.com/science/article/pii/S0021999196901308>.

Jiang, H.; Sheng, Y.; Ngai, T. Pickering emulsions: Versatility of colloidal particles and recent applications. *Current Opinion in Colloid & Interface Science*, v. 49, p. 1 – 15, 2020. ISSN 1359-0294. Emulsions and Microemulsions. Available on: <http://www.sciencedirect.com/science/article/pii/S135902942030039X>.

Kennedy, M.; Pozrikidis, C.; Skalak, R. Motion and deformation of liquid drops, and the rheology of dilute emulsions in simple shear flow. *Computers and Fluids*, v. 23, n. 2, p. 251–278, 1994. ISSN 0045-7930. Available on: <https://www.sciencedirect.com/science/article/pii/004579309490040X>.

Kerner, E. H. The elastic and thermo-elastic properties of composite media. *Proceedings of the Physical Society. Section B*, IOP Publishing, v. 69, n. 8, p. 808–813, aug 1956. Available on: <https://doi.org/10.1088/0370-1301/69/8/305>.

Kim, K.-M.; Oh, H. M.; Lee, J. H. Controlling the emulsion stability of cosmetics through shear mixing process. *Korea-Australia Rheology Journal*, v. 32, n. 4, p. 243–249, Nov 2020. ISSN 2093-7660. Available on: <https://doi.org/10.1007/s13367-020-0023-4>.

Li, D. *Encyclopedia of Microfluidics and Nanofluidics*. Springer US, 2008. (Encyclopedia of Microfluidics and Nanofluidics). ISBN 9780387324685. Available on: <https://books.google.com.br/books?id=vFI5fcNFbgYC>.

Liao, H.; Li, S.; Liu, C.; Tao, G. Rheological investigation with palierne's model on a polystyrene/nylon 6 blending melt compatibilized by a polystyrene grafted maleic anhydride. *Open Journal of Organic Polymer Materials*, v. 10, n. 2, p. 17–25, 2020.

Liu, H.; Lu, Y.; Li, S.; Yu, Y.; Sahu, K. C. Deformation and breakup of a compound droplet in three-dimensional oscillatory shear flow. *International Journal of Multiphase Flow*, v. 134, p. 103472, 2021. ISSN 0301-9322. Available on: <https://www.sciencedirect.com/science/article/pii/S0301932220305838>.

Liu, Q.; Li, H.; Lam, K. Optimization of deformable magnetic-sensitive hydrogel-based targeting system in suspension fluid for site-specific drug delivery. *Molecular pharmaceutics*, ACS Publications, v. 15, n. 10, p. 4632–4642, 2018. Available on: <https://doi.org/10.1021/acs.molpharmaceut.8b00626>.

Liu, X.-D.; Osher, S.; Chan, T. Weighted essentially non-oscillatory schemes. *Journal of Computational Physics*, v. 115, n. 1, p. 200–212, 1994. ISSN 0021-9991. Available on: <https://www.sciencedirect.com/science/article/pii/S0021999184711879>.

Ma, S.; Zong, W.; Han, X. Magnetic-responsive pickering emulsion and its catalytic application at the water–oil interface. *New J. Chem.*, The Royal Society of Chemistry, v. 45, p. 3974–3980, 2021. Available on: <http://dx.doi.org/10.1039/D0NJ05875K>.

Maffettone, P.; Minale, M. Equation of change for ellipsoidal drops in viscous flow. *Journal of Non-Newtonian Fluid Mechanics*, v. 78, n. 2, p. 227–241, 1998. ISSN 0377-0257. Available on: <https://www.sciencedirect.com/science/article/pii/S0377025798000652>.

Mandal, S.; Sinha, S.; Bandopadhyay, A.; Chakraborty, S. Drop deformation and emulsion rheology under the combined influence of uniform electric field and linear flow. *Journal of Fluid Mechanics*, Cambridge University Press, v. 841, p. 408–433, 2018.

Maphosa, Y.; Jideani, V. A. Factors affecting the stability of emulsions stabilised by biopolymers. In: Karakuş, S. (Ed.). *Science and Technology Behind Nanoemulsions*. Rijeka: IntechOpen, 2018. Chap. 5. Available on: <https://doi.org/10.5772/intechopen.75308>.

McAdams, A.; Sifakis, E.; Teran, J. A parallel multigrid poisson solver for fluids simulation on large grids. In: *Proceedings of the 2010 ACM SIGGRAPH/Eurographics Symposium on Computer Animation*. Goslar, DEU: Eurographics Association, 2010. (SCA '10), p. 65–74.

McKee, S.; Tomé, M.; Ferreira, V.; Cuminato, J.; Castelo, A.; Sousa, F.; Mangiavacchi, N. The mac method. *Computers Fluids*, v. 37, n. 8, p. 907–930, 2008. ISSN 0045-7930. Available on: <https://www.sciencedirect.com/science/article/pii/S0045793007001909>.

Mefford, O. T.; Woodward, R. C.; Goff, J. D.; Vadala, T.; St. Pierre, T. G.; Dailey, J. P.; Riffle, J. S. Field-induced motion of ferrofluids through immiscible viscous media: Testbed for restorative treatment of retinal detachment. *Journal of Magnetism and Magnetic Materials*, v. 311, n. 1, p. 347 – 353, 2007. ISSN 0304-8853. Proceedings of the Sixth International Conference on the Scientific and Clinical Applications of Magnetic Carriers. Available on: <http://www.sciencedirect.com/science/article/pii/S0304885306025728>.

Meng, F.; Matsunaga, D.; Yeomans, J.; Golestanian, R. Magnetically-actuated artificial cilium: a simple theoretical model. *Soft Matter*, Royal Society of Chemistry, n. 19, p. 3864–3871, 2019.

Morillas, J. R.; Vicente, J. de. Magnetorheology: a review. *Soft Matter*, Royal Society of Chemistry, v. 16, n. 42, p. 9614–9642, 2020. Available on: <http://dx.doi.org/10.1039/D0SM01082K>.

Oldroyd, J. G.; Taylor, G. I. The effect of interfacial stabilizing films on the elastic and viscous properties of emulsions. *Proceedings of the Royal Society of London. Series A. Mathematical and Physical Sciences*, v. 232, n. 1191, p. 567–577, 1955. Available on: <https://royalsocietypublishing.org/doi/abs/10.1098/rspa.1955.0240>.

Oldroyd, J. G.; Wilson, A. H. On the formulation of rheological equations of state. *Proceedings of the Royal Society of London. Series A. Mathematical and Physical Sciences*, v. 200, n. 1063, p. 523–541, 1950. Available on: <https://royalsocietypublishing.org/doi/abs/10.1098/rspa.1950.0035>.

Oldroyd, J. G.; Wilson, A. H. The elastic and viscous properties of emulsions and suspensions. *Proceedings of the Royal Society of London. Series A. Mathematical and Physical Sciences*, v. 218, n. 1132, p. 122–132, 1953. Available on: <https://royalsocietypublishing.org/doi/abs/10.1098/rspa.1953.0092>.

Oliveira, T. F.; Cunha, F. R. Emulsion rheology for steady and oscillatory shear flows at moderate and high viscosity ratio. *Rheologica Acta*, v. 54, n. 11, p. 951–971, Dec 2015. ISSN 1435-1528. Available on: <https://doi.org/10.1007/s00397-015-0885-4>.

Oliveira, T. F. de. Microhidrodinâmica e reologia de emulsões. Pontifícia Universidade Católica do Rio de Janeiro (PhD Thesis), 2007.

Olsson, E.; Kreiss, G.; Zahedi, S. A conservative level set method for two phase flow ii. *Journal of Computational Physics*, v. 225, n. 1, p. 785–807, 2007. ISSN 0021-9991. Available on: <https://www.sciencedirect.com/science/article/pii/S0021999107000046>.

Osher, S. A level set formulation for the solution of the dirichlet problem for hamilton–jacobi equations. *SIAM Journal on Mathematical Analysis*, v. 24, n. 5, p. 1145–1152, 1993. Available on: <https://doi.org/10.1137/0524066>.

Osher, S.; Sethian, J. A. Fronts propagating with curvature-dependent speed: Algorithms based on hamilton-jacobi formulations. *Journal of Computational Physics*, v. 79, n. 1, p. 12–49, 1988. ISSN 0021-9991. Available on: <https://www.sciencedirect.com/science/article/pii/0021999188900022>.

Osher, S. J.; Fedkiw, R. *Level set methods and dynamic implicit surfaces.* : Springer, 2003. v. 153. I-XIII, 1-273 p. (Applied mathematical sciences, v. 153). ISBN 0387954821.

Pal, R. Rheology of simple and multiple emulsions. *Current Opinion in Colloid Interface Science*, v. 16, n. 1, p. 41–60, 2011. ISSN 1359-0294. Available on: <https://www.sciencedirect.com/science/article/pii/S1359029410001135>.

Pal, R. Fundamental rheology of disperse systems based on single-particle mechanics. *Fluids*, MDPI AG, v. 1, n. 4, p. 40, Dec 2016. ISSN 2311-5521. Available on: <http://dx.doi.org/10.3390/fluids1040040>.

Pal, R. *Rheology of Particulate Dispersions and Composites.* CRC Press, 2019. ISBN 9780367453343. Available on: <https://www.routledge.com/Rheology-of-Particulate-Dispersions-and-Composites/Pal/p/book/9780367453343>.

Palierne, J. F. Linear rheology of viscoelastic emulsions with interfacial tension. *Rheologica Acta*, v. 29, n. 3, p. 204–214, may 1990. Available on: <https://link.springer.com/article/10.1007%2FBF01331356#citeas>.

Pei, H.; Shu, Z.; Zhang, G.; Ge, J.; Jiang, P.; Qin, Y.; Cao, X. Experimental study of nanoparticle and surfactant stabilized emulsion flooding to enhance heavy oil recovery. *Journal of Petroleum Science and Engineering*, v. 163, p. 476–483, 2018. ISSN 0920-4105. Available on: <https://www.sciencedirect.com/science/article/pii/S0920410518300287>.

Peng, D.; Merriman, B.; Osher, S.; Zhao, H.; Kang, M. A pde-based fast local level set method. *Journal of Computational Physics*, v. 155, n. 2, p. 410–438, 1999. ISSN 0021-9991. Available on: <https://www.sciencedirect.com/science/article/pii/S0021999199963453>.

Pimenta, P. H. N.; Oliveira, T. F. Study on the rheology of a dilute emulsion of surfactant-covered droplets using the level set and closest point methods. *Physics of Fluids*, v. 33, n. 10, p. 103306, 2021. Available on: <https://doi.org/10.1063/5.0064729>.

Poddar, A.; Mandal, S.; Bandopadhyay, A.; Chakraborty, S. Electrorheology of a dilute emulsion of surfactant-covered drops. *Journal of Fluid Mechanics*, Cambridge University Press, v. 881, p. 524–550, 2019.

Press, W. H.; Flannery, B. P.; Teukolsky, S. A.; Vetterling, W. T. *Numerical Recipes in FORTRAN 77: The Art of Scientific Computing.* 2. ed. Cambridge University Press, 1992. Hardcover. ISBN 052143064X. Available on: <http://www.worldcat.org/isbn/052143064X>.

Raja, R. V.; Subramanian, G.; Koch, D. L. Inertial effects on the rheology of a dilute emulsion. *Journal of Fluid Mechanics*, Cambridge University Press, v. 646, p. 255–296, 2010.

Ray, A.; Varma, V.; Jayaneel, P.; Sudharsan, N.; Wang, Z.; Ramanujan, R. On demand manipulation of ferrofluid droplets by magnetic fields. *Sensors and Actuators B: Chemical*, v. 242, p. 760–768, 2017. ISSN 0925-4005. Available on: <https://www.sciencedirect.com/science/article/pii/S092540051631913X>.

Roodan, V. A.; Gómez-Pastora, J.; Karampelas, I. H.; González-Fernández, C.; Bringas, E.; Ortiz, I.; Chalmers, J. J.; Furlani, E. P.; Swihart, M. T. Formation and manipulation of ferrofluid droplets with magnetic fields in a microdevice: a numerical parametric study. *Soft Matter*, Royal Society of Chemistry, v. 16, n. 41, p. 9506–9518, 2020. Available on: <http://dx.doi.org/10.1039/D0SM01426E>.

Rosa, A. P.; Cunha, F. R. The influence of dipolar particle interactions on the magnetization and the rotational viscosity of ferrofluids. *Physics of Fluids*, v. 31, n. 5, p. 052006, 2019. Available on: <https://doi.org/10.1063/1.5093267>.

Rosa, A. P.; Cunha, F. R. Shear rate dependence of viscosity and normal stress differences in ferrofluids. *Journal of Magnetism and Magnetic Materials*, v. 499, p. 166184, 2020. ISSN 0304-8853. Available on: <https://www.sciencedirect.com/science/article/pii/S0304885319327702>.

Rosensweig, R. E. *Ferrohydrodynamics*. : Courier Corporation, 2013.

Royston, M.; Pradhana, A.; Lee, B.; Chow, Y. T.; Yin, W.; Teran, J.; Osher, S. Parallel redistancing using the hopf–lax formula. *Journal of Computational Physics*, v. 365, p. 7–17, 2018. ISSN 0021-9991. Available on: <https://www.sciencedirect.com/science/article/pii/S0021999118300457>.

Schramm, L. *Emulsions, Foams, Suspensions, and Aerosols: Microscience and Applications*. Wiley, 2014. ISBN 9783527337064. Available on: <https://books.google.com.br/books?id=i2dEBAAAQBAJ>.

Sen, U.; Chatterjee, S.; Sen, S.; Tiwari, M. K.; Mukhopadhyay, A.; Ganguly, R. Dynamics of magnetic modulation of ferrofluid droplets for digital microfluidic applications. *Journal of Magnetism and Magnetic Materials*, v. 421, p. 165–176, 2017. ISSN 0304-8853. Available on: <https://www.sciencedirect.com/science/article/pii/S030488531631544X>.

Sharma, S.; Singh, M. Wettability and friccohesity of emulsions: Covid-19 killing robust science - a review. *International Journal Of Research In Pharmacy And Chemistry*, v. 11, n. 2, p. 43–54, 2021. ISSN 2231-2781. Available on: <https://dx.doi.org/10.33289/IJRPC.11.2.2021.11(13)>.

Shu, C.-W.; Osher, S. Efficient implementation of essentially non-oscillatory shock-capturing schemes. *Journal of Computational Physics*, v. 77, n. 2, p. 439–471, 1988. ISSN 0021-9991. Available on: <https://www.sciencedirect.com/science/article/pii/0021999188901775>.

Shu, C.-W.; Osher, S. Efficient implementation of essentially non-oscillatory shock-capturing schemes, ii. *Journal of Computational Physics*, v. 83, n. 1, p. 32–78, 1989. ISSN 0021-9991. Available on: <https://www.sciencedirect.com/science/article/pii/0021999189902222>.

Shu, R.; Sun, W.; Wang, T.; Wang, C.; Liu, X.; Tong, Z. Linear and nonlinear viscoelasticity of water-in-oil emulsions: Effect of droplet elasticity. *Colloids and Surfaces A: Physicochemical and Engineering Aspects*, v. 434, p. 220–228, 2013. ISSN 0927-7757. Available on: <https://www.sciencedirect.com/science/article/pii/S0927775713004408>.

Shukla, T.; Upmanyu, N.; Agrawal, M.; Saraf, S.; Saraf, S.; Alexander, A. Biomedical applications of microemulsion through dermal and transdermal route. *Biomedicine Pharmacotherapy*, v. 108, p. 1477–1494, 2018. ISSN 0753-3322. Available on: <https://www.sciencedirect.com/science/article/pii/S0753332218353393>.

Siqueira, I. R.; Rebouças, R. B.; Oliveira, T. F.; Cunha, F. R. A new mesh relaxation approach and automatic time-step control method for boundary integral simulations of a viscous drop. *International Journal for Numerical Methods in Fluids*, v. 84, n. 4, p. 221–238, 2017. Available on: <https://onlinelibrary.wiley.com/doi/abs/10.1002/fld.4346>.

Siqueira, I. R. d.; Rebouças, R. B.; Cunha, L. H. P. d.; Oliveira, T. F. d. On the volume conservation of emulsion drops in boundary integral simulations. *Journal of the Brazilian Society of Mechanical Sciences and Engineering*, v. 40, n. 1, p. 3, Dec 2017. ISSN 1806-3691. Available on: <https://doi.org/10.1007/s40430-017-0924-4>.

Solomenko, Z.; Spelt, P. D.; Ó Náraigh, L.; Alix, P. Mass conservation and reduction of parasitic interfacial waves in level-set methods for the numerical simulation of two-phase flows: A comparative study. *International Journal of Multiphase Flow*, v. 95, p. 235–256, 2017. ISSN 0301-9322. Available on: <https://www.sciencedirect.com/science/article/pii/S0301932216304669>.

Spatafora-Salazar, A.; Lobmeyer, D. M.; Cunha, L. H. P.; Joshi, K.; Biswal, S. L. Hierarchical assemblies of superparamagnetic colloids in time-varying magnetic fields. *Soft Matter*, The Royal Society of Chemistry, v. 17, p. 1120–1155, 2021. Available on: <http://dx.doi.org/10.1039/D0SM01878C>.

Stephen, P. S. *Low viscosity magnetic fluid obtained by the colloidal suspension of magnetic particles*. U.S. Patent 3 215 572 A, 1963.

Stone, H. Breakup of concentric double emulsion droplets in linear flows. *Journal of Fluid Mechanics*, Cambridge University Press, v. 211, n. 123, p. 123–156, fev. 1992. ISSN 0022-1120.

Stone, H. A.; Leal, L. G. The effects of surfactants on drop deformation and breakup. *Journal of Fluid Mechanics*, Cambridge University Press, v. 220, p. 161–186, 1990.

Sussman, M.; Fatemi, E. An efficient, interface-preserving level set redistancing algorithm and its application to interfacial incompressible fluid flow. *SIAM J. Sci. Comput.*, Society for Industrial and Applied Mathematics, USA, v. 20, n. 4, p. 1165–1191, fev. 1999. ISSN 1064-8275. Available on: <https://doi.org/10.1137/S1064827596298245>.

Sussman, M.; Puckett, E. G. A coupled level set and volume-of-fluid method for computing 3d and axisymmetric incompressible two-phase flows. *Journal of Computational Physics*, v. 162, n. 2, p. 301–337, 2000. ISSN 0021-9991. Available on: <https://www.sciencedirect.com/science/article/pii/S0021999100965379>.

Tadros, T. Fundamental principles of emulsion rheology and their applications. *Colloids and Surfaces A: Physicochemical and Engineering Aspects*, v. 91, p. 39–55, 1994. ISSN 0927-7757. A selection of papers presented at the First World Congress on Emulsions. Available on: <https://www.sciencedirect.com/science/article/pii/092777579302709N>.

Tadros, T. F. *Emulsion Formation, Stability, and Rheology*. John Wiley Sons, Ltd, 2013. ISBN 9783527647941. Available on: <https://onlinelibrary.wiley.com/doi/book/10.1002/9783527647941>.

Tayeb, H. H.; Felimban, R.; Almaghrabi, S.; Hasaballah, N. Nanoemulsions: Formulation, characterization, biological fate, and potential role against covid-19 and other viral outbreaks. *Colloid and Interface Science Communications*, v. 45, p. 100533, 2021. ISSN 2215-0382. Available on: <https://www.sciencedirect.com/science/article/pii/S2215038221001734>.

Taylor, G. I. The viscosity of a fluid containing small drops of another fluid. *Proceedings of the Royal Society of London. Series A, Containing Papers of a Mathematical and Physical Character*, v. 138, n. 834, p. 41–48, 1932. Available on: <https://royalsocietypublishing.org/doi/abs/10.1098/rspa.1932.0169>.

Taylor, G. I. The formation of emulsions in definable fields of flow. *Proceedings of the Royal Society of London. Series A, Containing Papers of a Mathematical and Physical Character*, The Royal Society, v. 146, n. 858, p. 501–523, 1934. ISSN 09501207. Available on: <http://www.jstor.org/stable/2935605>.

Témam, R. Sur l'approximation de la solution des équations de navier-stokes par la méthode des pas fractionnaires (i). *Archive for Rational Mechanics and Analysis*, v. 32, n. 2, p. 135–153, Jan 1969. ISSN 1432-0673. Available on: <https://doi.org/10.1007/BF00247678>.

Témam, R. Sur l'approximation de la solution des équations de navier-stokes par la méthode des pas fractionnaires (ii). *Archive for Rational Mechanics and Analysis*, v. 33, n. 5, p. 377–385, Jan 1969. ISSN 1432-0673. Available on: <https://doi.org/10.1007/BF00247696>.

Tiwari, S.; Mall, C.; Solanki, P. P. Surfactant and its applications: A review. *International Journal of Engineering Research and Application*, v. 8, n. 9, p. 61–66, 2018. Available on: <https://www.ijera.com/papers/vol8no9/p1/M0809016166.pdf>.

Tsitsiklis, J. N. Efficient algorithms for globally optimal trajectories. In: *Proceedings, IEEE 33rd Conference on Decision and Control*. 1994. p. 1368–1373.

Tsitsiklis, J. N. Efficient algorithms for globally optimal trajectories. *IEEE Transactions on Automatic Control*, v. 40, n. 9, p. 1528–1538, 1995.

Vananroye, A.; Puyvelde, P. V.; Moldenaers, P. Effect of confinement on droplet breakup in sheared emulsions. *Langmuir*, v. 22, n. 9, p. 3972–3974, 2006. PMID: 16618134. Available on: <https://doi.org/10.1021/la060442+>.

Varma, V.; Ray, A.; Wang, Z.; Wang, Z.; Ramanujan, R. Droplet merging on a lab-on-a-chip platform by uniform magnetic fields. *Scientific reports*, Nature Publishing Group, v. 6, n. 1, p. 1–12, 2016. Available on: <https://doi.org/10.1038/srep37671>.

Vicente, J. D.; Klingenberg, D. J.; Hidalgo-Alvarez, R. Magnetorheological fluids: a review. *Soft matter*, Royal Society of Chemistry, v. 7, n. 8, p. 3701–3710, 2011. Available on: <http://dx.doi.org/10.1039/C0SM01221A>.

Vlahovska, P. M. On the rheology of a dilute emulsion in a uniform electric field. *Journal of Fluid Mechanics*, Cambridge University Press, v. 670, p. 481–503, 2011.

Vlahovska, P. M.; Bławzdziewicz, J.; Loewenberg, M. Small-deformation theory for a surfactant-covered drop in linear flows. *Journal of Fluid Mechanics*, Cambridge University Press, v. 624, p. 293–337, 2009. Available on: <https://doi.org/10.1017/S0022112008005417>.

Voltairas, P.; Fotiadis, D.; Massalas, C. Elastic stability of silicone ferrofluid internal tamponade (sfit) in retinal detachment surgery. *Journal of Magnetism and Magnetic Materials*, v. 225, n. 1, p. 248–255, 2001. ISSN 0304-8853. Proceedings of the Third International Conference on Scientific and Clinical Applications of Magnetic Carriers. Available on: <https://www.sciencedirect.com/science/article/pii/S0304885300012658>.

Wannaborworn, S.; Mackley, M. R.; Renardy, Y. Experimental observation and matching numerical simulation for the deformation and breakup of immiscible drops in oscillatory shear. *Journal of Rheology*, v. 46, n. 5, p. 1279–1293, 2002. Available on: <https://doi.org/10.1122/1.1501960>.

Wong, T.; Leung, S. A fast sweeping method for eikonal equations on implicit surfaces. *Journal of Scientific Computing*, v. 67, n. 3, p. 837–859, Jun 2016. ISSN 1573-7691. Available on: <https://doi.org/10.1007/s10915-015-0105-5>.

Wu, H.; Song, L.; Chen, L.; Huang, Y.; Wu, Y.; Zang, F.; An, Y.; Lyu, H.; Ma, M.; Chen, J.; Gu, N.; Zhang, Y. Injectable thermosensitive magnetic nanoemulsion hydrogel for multimodal-imaging-guided accurate thermoablative cancer therapy. *Nanoscale*, The Royal Society of Chemistry, v. 9, p. 16175–16182, 2017. Available on: <http://dx.doi.org/10.1039/C7NR02858J>.

Yang, H.; Zhang, H.; Peng, J.; Zhang, Y.; Du, G.; Fang, Y. Smart magnetic ionic liquid-based pickering emulsions stabilized by amphiphilic fe3o4 nanoparticles: Highly efficient extraction systems for water purification. *Journal of Colloid and Interface Science*, v. 485, p. 213–222, 2017. ISSN 0021-9797. Available on: <https://www.sciencedirect.com/science/article/pii/S0021979716306786>.

Yang, M.; Shaqfeh, E. S. G. Mechanism of shear thickening in suspensions of rigid spheres in boger fluids. part i: Dilute suspensions. *Journal of Rheology*, v. 62, n. 6, p. 1363–1377, 2018. Available on: <https://doi.org/10.1122/1.5024696>.

Yang, M.; Shaqfeh, E. S. G. Mechanism of shear thickening in suspensions of rigid spheres in boger fluids. part ii: Suspensions at finite concentration. *Journal of Rheology*, v. 62, n. 6, p. 1379–1396, 2018. Available on: <https://doi.org/10.1122/1.5024698>.

Yang, Y.; Fang, Z.; Chen, X.; Zhang, W.; Xie, Y.; Chen, Y.; Liu, Z.; Yuan, W. An overview of pickering emulsions: Solid-particle materials, classification, morphology, and applications. *Frontiers in Pharmacology*, v. 8, 2017. ISSN 1663-9812. Available on: <https://www.frontiersin.org/articles/10.3389/fphar.2017.00287>.

Yu, W.; Bousmina, M. Ellipsoidal model for droplet deformation in emulsions. *Journal of Rheology*, v. 47, n. 4, p. 1011–1039, 2003. Available on: <https://doi.org/10.1122/1.1582853>.

Zakinyan, A.; Dikansky, Y. Drops deformation and magnetic permeability of a ferrofluid emulsion. *Colloids and Surfaces A: Physicochemical and Engineering Aspects*, v. 380, n. 1, p. 314–318, 2011. ISSN 0927-7757. Available on: <https://www.sciencedirect.com/science/article/pii/S0927775711001762>.

Zentner, C. A.; Concellón, A.; Swager, T. M. Controlled movement of complex double emulsions via interfacially confined magnetic nanoparticles. *ACS Central Science*, v. 6, n. 8, p. 1460–1466, 2020. PMID: 32875087. Available on: <https://doi.org/10.1021/acscentsci.0c00686>.

Zhang, J.; Hassan, M. R.; Rallabandi, B.; Wang, C. Migration of ferrofluid droplets in shear flow under a uniform magnetic field. *Soft Matter*, Royal Society of Chemistry, v. 15, n. 11, p. 2439–2446, 2019. Available on: <http://dx.doi.org/10.1039/C8SM02522C>.

Zhang, X.; Sun, L.; Yu, Y.; Zhao, Y. Flexible ferrofluids: Design and applications. *Advanced Materials*, Wiley Online Library, v. 31, n. 51, p. 1903497, 2019.

Zhao, X. Drop breakup in dilute newtonian emulsions in simple shear flow: New drop breakup mechanisms. *Journal of Rheology*, v. 51, n. 3, p. 367–392, 2007. Available on: <https://doi.org/10.1122/1.2714641>.

Zhou, Y.; Yin, D.; Chen, W.; Liu, B.; Zhang, X. A comprehensive review of emulsion and its field application for enhanced oil recovery. *Energy Science & Engineering*, v. 7, n. 4, p. 1046–1058, 2019. Available on: <https://onlinelibrary.wiley.com/doi/abs/10.1002/ese3.354>.